

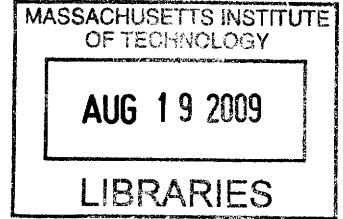
Detection of Improvised Explosive Devices at Long-Range Using Coded Aperture Imaging of Backscattered X-Rays with Dynamic Reconstruction

by

Jayna T. Bell

B.S., Environmental Science (2000)

The United States Military Academy



Submitted to the Department of Nuclear Science and Engineering in Partial Fulfillment of the Requirements for the Degree of Master of Science in Nuclear Science and Engineering at the

Massachusetts Institute of Technology

[JUNE] May 2009

© 2009 Massachusetts Institute of Technology All rights reserved

ARCHIVES

Signature of Author [Signature] Department of Nuclear Science and Engineering May 8, 2009

Certified by [Signature] Richard C. Lanza Senior Research Scientist in Nuclear Science and Engineering Thesis Supervisor

Certified by [Signature] Jacquelyn C. Yanch Professor in Nuclear Science and Engineering Thesis Reader

Certified by [Signature] Berthold K.P. Horn Professor in Electrical Engineering and Computer Science Thesis Reader

Accepted by [Signature] Jacquelyn C. Yanch Professor in Nuclear Science and Engineering Chairman, Department Committee on Graduate Students

Detection of Improvised Explosive Devices at Long-Range Using Coded Aperture Imaging of Backscattered X-Rays with Dynamic Reconstruction

by

Jayna T. Bell

Submitted to the Department of Nuclear Science and Engineering
in Partial Fulfillment of the Requirements for the Degree of
Master of Science in Nuclear Science and Engineering

ABSTRACT

Standoff detection of improvised explosive devices (IEDs) is a continuing problem for the U.S. military. Current X-ray detection systems cannot detect explosives at distances above a few meters and with a source-detector system moving in relation to the target. The aim of this study is to determine the feasibility of a large-area, Coded-Aperture Imaging (CAI) system using X-Ray backscatter as the source of radiation. A moving source-detector system required development of a new reconstruction technique, dynamic reconstruction (DR), which continually back-projects detected events on an event-by-event basis. This research imaged multiple low-Z (polyethylene and water-filled), area targets with backscattered X-rays using standard medical imaging equipment, coded aperture masks with ideal bi-level autocorrelation properties, and dynamic reconstruction (DR). Lower fill factor apertures were the primary metric investigated because contrast was shown to be inversely related to the mask's percentage of open area. This study experimentally determined the optimal mask fill factor, gamma camera imaging protocols, and experimental geometry by examining the resulting effects on image quality. Reconstructed images were analyzed for Contrast-to-noise ratio (CNR), Signal-to-noise Ratio (SNR), resolution, sharpness, the uniformity of the background (artifacts). In addition to changing the fill factor, additional methods of improving the contrast included changing the experimental geometry, reducing the X-ray tube filtration, and widening the X-ray source's cone beam (FOV). 14 studies were performed that found 25% fill factor mask reconstructions had the highest average CNR (14.7), compared to 50% and 12.5% fill factor (CNRs 8.50 and 6.9, respectively) with a system resolution of 25 mm at the target. Thus, this study's techniques confirmed that large-area, low fill factor coded apertures could successfully be used, in conjunction with dynamic reconstruction, to image complex, extended scenes at 5 meters with capabilities of up to 50 meters or more.

Thesis Supervisor: Richard C. Lanza

Title: Senior Research Scientist in Nuclear Science and Engineering
Department of Nuclear Science and Engineering

TABLE OF CONTENTS

ABSTRACT	2
TABLE OF CONTENTS	3
LIST OF FIGURES	5
LIST OF TABLES	7
LIST OF ACRONYMS	7
1. INTRODUCTION	9
1.1 Project Background and Motivation	9
1.2. Theory.....	12
1.21. Coded Aperture Imaging.	12
1.22. Metrics Affecting an Ideal Image.....	16
1.23. Dynamic Reconstruction	20
1.24. Compton Theory.....	21
1.3 Approach and Objectives of the Project	24
2. APPARATUS AND PROCEDURES	25
2.1. Apparatus.....	25
2.1.1 Gamma Camera.....	25
2.1.2 Coded Aperture Masks.....	26
2.1.3 X-ray Tube	27
2.2. Procedures.....	28
2.2.1 PHASE I Preparation for Imaging.....	28
2.2.2 PHASE II Point Source Tests.....	34
2.2.3 PHASE III Area Source Tests	35
2.2.4 PHASE IV X-ray Backscatter Tests.....	37
3. RESULTS	43
3.1 PHASE I. Preparation for Imaging	43
3.2 PHASE II. Point Source Tests	47
3.3. PHASE III Area Source Tests	49
3.3.1 50% fill factor mask	49
3.3.2 25% fill factor mask	50
3.3.3 12.5% fill factor mask	51
3.4. PHASE IV. X-ray Backscatter Tests	54
3.4.1. 50% fill factor mask.	54
3.4.2. 25% fill factor mask	60
3.4.3. 12.5% fill factor mask.	67
4. DISCUSSION	72
4.1. PHASE I.	72
4.2 PHASE II.....	74
4.3 PHASE III Area Source Tests	75
4.3.1 50% fill factor mask.	76
4.3.2 25% fill factor mask	75
4.3.3 12.5% fill factor mask.	77
4.4. PHASE IV. X-ray Backscatter Tests	79
4.4.1. 50% fill mask.....	79
4.4.2. 25% fill factor mask.....	83
4.2.3. 12.5% fill factor mask.	86
4.5 Contrast-to-noise and Resolution.....	89
CONCLUSION	94
REFERENCES	97

ACKNOWLEDGEMENTS.....100
APPENDICES101
 Appendix A. An Addendum to Coded Aperture Imaging Mathematics..... 101
 Appendix B. Coded Aperture Mask Design 105
 Appendix C. Addendum to X-Ray Experiments 110
BIBLIOGRAPHY 117

LIST OF FIGURES

Figure 1. Encoding of the signal.....	14
Figure 2. Magnification effects from mask hole diameter.....	20
Figure 3. Hexagonal uniformly redundant array mask drill patterns.....	27
Figure 4. Coded aperture camera.....	27
Figure 5. Geometry of initial gamma camera experiments.....	29
Figure 6. 4-quadrant lead phantom.....	31
Figure 7. Targets used for X-ray backscatter experiments.....	33
Figure 8. Area source during acquisitions.....	33
Figure 9. Geometry for Area Source tests.....	36
Figure 10. Experiment geometry for X-ray backscatter tests.....	39
Figure 11. Verification of Anger camera resolution.....	44
Figure 12. Signal-to-noise versus frequency.....	45
Figure 13. Gamma camera Modulation Transfer Function.....	46
Figure 14. Backscatter Energy spectrum for 225 keV X-rays centered about 114 keV.....	47
Figure 15. Reconstructed point source, 50% fill mask.....	48
Figure 16. Magnified 50% fill factor mask shadow.....	49
Figure 17. Single-frame reconstruction of area source target imaged with the 50% fill mask.....	49
Figure 18. Estimated lateral motion of the carriage (tug).....	50
Figure 19. Reconstructed area source images, 25% fill mask.....	51
Figure 20. Reconstructed area source images with artifacts, 25% fill mask.....	51
Figure 21. Area Source target, 12.5% fill factor mask.....	52
Figure 22. Gamma ray throughput as a function of mask-source distance.....	53
Figure 23. LOG of Count Rate versus LOG Distance.....	54
Figure 24. Determination of minimum total counts per image, water jug, 50% fill mask.....	55
Figure 25. Systematic error due to misalignment of mask-detector axis of symmetry.....	55
Figure 26. Water Jug Sequence reacquired with optical axis aligned., 50% fill mask.....	56
Figure 27. Rings, 50% fill mask.....	57
Figure 28. Rings on Lead Bricks, 50% fill mask.....	57
Figure 29. Reconstructed arrow after optimizing gamma camera imaging protocols, 50% fill masks.....	58
Figure 30. Water jug after changing experimental geometry, 50% fill mask.....	58
Figure 31. Arrow with Mask-Anti-mask addition, 50% fill mask.....	59
Figure 32. Single frame reconstruction of the arrow, 25% fill mask.....	61
Figure 33. Reconstructed Water jug imaged on lead bricks and polyethylene, 25% fill mask.....	61
Figure 34. Rings with less X-ray tube filtration, 25% fill mask.....	62
Figure 35. Reconstructed arrow sequence after widening of cone beam.....	63
Figure 36. Multiple Object scene, 25% fill factor mask.....	64
Figure 37. Reconstructed arrow, high matrix detector output.....	65
Figure 38. Reconstructed arrow, lower matrix detector output.....	66
Figure 39. System resolution calculation for 25% fill factor mask.....	67
Figure 40. Full Width at Half Maximum, point-source calibration, 12.5% fill factor mask.....	68
Figure 41. Reconstructed arrow, 12.5% mask.....	68
Figure 42. Reconstructed multiple object scene, 12.5% fill mask.....	69
Figure 43. Smoothed multiple object scene, 12.5% fill mask.....	70
Figure 44. Point Source Series showing presence of self-collimation effects.....	71
Figure 45. Self-collimation effects increased background noise at closer distances.....	72
Figure B-1. Hexagonal Uniformly Redundant Array, 50% fill factor.....	108
Figure C-1. Water jug sequence, optical axis aligned, 50% fill mask.....	110

Figure C-2. Polyethylene rings sequence on poly sheets.	111
Figure C-3. Arrow before and after a change in geometry, 50% fill mask.....	111
Figure C-4. Reconstructed arrow sequence with 50% fill mask.	112
Figure C-5. Reconstructed arrow sequence with 50% fill antimask	112
Figure C-6. Calculation of mean intensity for Contrast-to-noise calculations.....	114
Figure C-1. Calculation of mean background and standard deviation.....	114
Figure C-2. Reconstructed rings with 25% fill mask.....	115
Figure C-3. Arrow sequence, 25% fill mask.....	115
Figure C-4. Reconstructed arrow sequence after widening of cone beam.....	116

LIST OF TABLES

Table 1. Gamma Camera Specifications.....	26
Table 2. Mask Metrics for 50%, 25%, and 12.5% fill factor masks	26
Table 3. Acquisitions for the 12.5% fill factor mask.....	37
Table 4. Summary of Experiments for X-ray Backscatter Experiments.....	38
Table 5. Determination of wavelength from four-quadrant bar phantom	43
Table 6. Contrast-to-noise ratio results for 25% fill factor reconstructions.....	60
Table 7. Contrast-to-noise ratio results for 25% fill factor reconstructions.....	66
Table B-1. Generation of 1-D array using quadratic residues.....	107

LIST OF ACRONYMS

CA: Coded Aperture
CAI: Coded aperture imaging
CNR: Contrast-to-noise ratio
DR: Dynamic Reconstruction
FOV: Field of View
FWHM: Full Width at Half Maximum
HURA: Hexagonal Uniformly Redundant Arrays
IED: Improvised Explosive Device
MTF: Modulation Transfer Function
MURA: Modified Uniformly Redundant Arrays
PMT: Photomultiplier Tube
PSF: Point Spread Function
SNR: Signal-to-noise Ratio
URA: Uniformly Redundant Arrays

1. INTRODUCTION

1.1 Project Background and Motivation

1.11 Purpose of investigation. Detection of improvised explosive devices (IEDs) at a distance has been and remains a pressing problem. One approach to this problem which has been proposed is to use backscattered X-rays to detect the low-Z materials of explosives. Backscatter has been previously used to detect contraband and explosives in vehicles and carried on individuals. The conventional approach, generally based on a variant of pencil-beam scanning, cannot be effectively used for two primary reasons. First, pencil-beam scanning rapidly degrades with distances of more than 1 or 2 m, so this approach is essentially useless for distances greater than 50 m which could provide the military with crucial standoff. Second, almost all of the work to date has assumed a fixed geometric relationship between the interrogating source and the detector rather than the practical case where the source and the detector are moving relative to the target object lying at a distance in front of the system, as is typical of current anti-IED, route reconnaissance missions.

Our approach addresses the aforementioned limitations of conventional X-ray imaging by illuminating the entire field of view with X-rays and imaging the backscatter using a coded aperture. Because the source-detector is in constant motion relative to the target, a new approach to coded aperture imaging with *dynamic reconstruction* was developed. Coded aperture imaging ameliorates the issue of having to image extended scenes. Large-area coded apertures are able to collect as much information as possible about the source while DR makes near real-time imaging possible by reconstructing on an event by event basis while the imaging system is in motion.

This research attempts to image IEDs with backscattered X-rays using standard medical imaging equipment, coded aperture imaging (CAI), and dynamic reconstruction (DR). Though the process of CAI is not new in practice, reconstruction methods have principally been used in static situations, where the geometry is well defined and constant in time. In this application, we will determine how well low-Z materials can be imaged using coded aperture and DR when the photon source is lower energy,

backscattered radiation in the presence of background noise. Target distances for a proposed final system will be up to 50 m.

1.12 Background. At the current time (2009) IEDs cause the most casualties to military personnel in both Operation Iraqi Freedom and Operation Enduring Freedom. A majority of IEDs are hastily emplaced on the shoulder of frequented roads and are composed of low-atomic number explosives, such as C4, PE4, or TNT. Sizes range from military-grade munitions such as 155 mm artillery shells (605 mm in height and 155 mm in diameter) or blocks of civilian-grade explosives packed in a container with shrapnel or ball bearings. More information on IEDs can be found in [12], [17], and [18]. Though the material can be easily camouflaged to the naked eye, this material is visible when imaged with X-Rays. The blast radius of typical IEDs is about 35 to 50 m when the munition is a 155 mm shell. Accordingly, standoff detection systems are preferred. Assuming a military vehicle is moving at 30 mph, the driver has roughly 3.5 s to decide to stop if an IED is detected 100m away¹. So, an imaging system must be in near-real time, have low failure rate, and provide image quality against inescapable background noise.

The main standoff IED detection system currently employed in the Joint Operating Environment is the Counter Remote Control Improvised Explosive Device (RCIED) Electronic Warfare (CREW) system which detonates remote-controlled IEDs prematurely by sending out initiation frequencies matching a wide variety of detonators. This system only works with RCIEDS and command-detonated IEDs do comprise a sizeable portion of the IED threat. The CREW system cannot detect the actual explosives, so implementation of this system is hampered by enemy use of RCIEDs. The common denominator of all IEDs, however, is the use of explosives which can be detected by CAI of X-rays.

Current CAI systems, however, are limited by short interrogation ranges and the requirement to scan a target from the side with a fixed separation distance. The backscatter image is formed using a pencil beam to obtain spatial resolution. This is a highly inefficient use of source X-rays and generally is effective only over short distances. Additionally, images are subject to cumbersome artifacts due to near-field detector-target geometry. In kind, new techniques in both CAI and DR address these limitations.

1.13 Challenges. In this application, an X-Ray source illuminates the field of view with a cone beam in order to maximize the amount of backscatter. Though CAI and DR make imaging with backscatter possible, they have challenges of their own. Additionally, the problem of spatially variant background noise is inescapable.

Because we are in a near-field geometry (compared to far-field applications in astronomy), care must be taken to avoid artifacts, with longer counting times to increase counting statistics. Increased signal implies using the largest hole-size possible, but the resolution of a coded aperture mask is maximized by using the smallest possible hole-size. Because we are working with lower flux as the input to the CAI system, using masks with thousands of holes achieves high sensitivity combined with the highest possible resolution. Signal throughput is increased, and a higher SNR ratio is the result provided the hole-size is kept small.

Newer techniques of DR do not use correlation and are fundamentally different from traditional coded aperture. In “fixed” CAI systems, the reconstruction technique uses correlation of the detector output pattern with the magnified mask pattern. This traditional static reconstruction technique does not work with a moving system because the CA allows radiation from multiple points on the target to reach a single point on the detector plane. So back-projection of that point on the detector would result in errors. On the contrary, dynamic reconstruction back-projects each event they accumulate provided there is known mask-source geometry.

Different fill-factor masks are tested to determine the relationship between the fraction of mask open area, reconstructed image resolution, and SNR. The drop in fill factor does not drastically reduce the received signal because the target is interrogated over a longer collection time while the detector system is moving. This collection time is proportional to the cross-track distance to the target’s original mask-source separation distance, z . In traditional imaging, increasing z produces a drop off that varies as $1/z^2$. However, with DR the target is in the FOV longer (observed over a time proportional to z) and the accumulated signal on the detector used in only falls off as $1/z$. This retention of sensitivity gives the DR

method the advantage when interrogating sources at a distance. A complete discussion on source-detector geometry and signal can be found in [21], [22].

Another distinct challenge is the removal of spatially-varying background noise. Even in head-on X-ray interrogation of an object with a detector on the opposite side there is background noise. Here, we are imaging from backscatter. An outgoing spectrum backscatters off a target, producing an incoming backscatter spectrum with a wider FWHM due to multiple Compton scattering events. Coded apertures are designed to collimate the desired X-rays (the ones traveling perpendicular to the mask plane) and the detector's energy windows can be set to filter out lower energy noise. However, with an outgoing and incoming beam air-scatter is a higher contributor of noise than in conventional X-ray imaging applications. Additionally, this higher noise pedestal will have a higher standard deviation which produces a lower overall contrast-to-noise ratio (CNR).

1.2. Theory

1.21. Coded Aperture Imaging.

1.21.1. Introduction to CAI. CAI is traditionally used to image radiation that cannot be reflected or refracted, such as gammas and hard X-rays. Though single pinholes can be used, the typical tradeoff between signal and resolution for pinhole systems deter their usage. In ideal pinhole imaging there is a 1:1 correspondence between the object and image with perfect resolution.² However, imaging times are long and there is little to no signal throughput. In 1961, Mertz and Young introduced the first CA for far-field imaging-which increased signal 10,000 times and allowed 3-D depth information gathering.³ CAs gain the resolution of a small pinhole but the increased SNR of a larger hole by having multiple small holes in a recognizable pattern called an array. CAI also allows imaging with higher energies and larger FOVs than focusing techniques. CAI has been mostly implemented in far-field geometry applications using long imaging times with point sources. Such applications produced nearly artifact-free images with

high SNR. However, when CAI is applied to near-field geometries the images are subject to artifacts and increased noise.

A CAI system consists of three components: a coded aperture mask, a position and energy-sensitive detector, and a back-projection algorithm. The first two components, when coupled, are collectively referred to as a coded aperture camera. Coded aperture masks have transparent and opaque areas (mask elements) sized according to the detector's spatial resolution limitations. Transparent and opaque mask elements will have values in the array of zero and one, respectively. The mask elements are spaced equidistant in a pre-determined basic pattern called an array. Arrays are 2-D compilations of repeating 1-D binary sequences assigned to a grid. The basic pattern repeats itself with overlapping edges. CA basic patterns are further discussed in Appendix B. The detector used in this investigation is an Anger Camera, further discussed in Section 2.1.1.

Imaging a source with the coded aperture camera encodes the data by convolving the original image with the mask pattern. Specifically, each point in the source (source in this case refers to backscattered radiation from the target) casts an enlarged, shifted shadow of the mask on detector as shown in Figure 5⁴. The size and location of the mask shadow depends on the mask-source distance and the source's lateral translation with respect to the mask's origin. Illumination will travel through transparent mask elements and be recorded on the detector. Opaque mask elements will correspond to shadowed areas. Because an area source is a collection of N point sources, the detector accumulates a sum of N magnified, shifted mask shadows. As a result, spatial information about the source is first encoded for subsequent decoding by the back-projection algorithm.

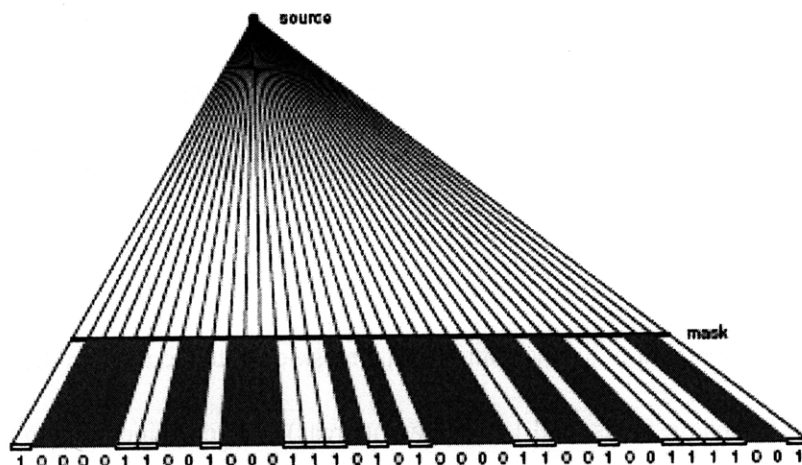


Figure 5. Encoding of the signal. Radiation from a single point casts an enlarged, shifted mask shadow on the detector. Radiation passing through transparent mask elements will be accumulated on the detector for later decoding by back-projection. Image is from [9].

The decoding process involves correlating the detector output with the same mask pattern which also serves as a decoding array. Assuming known mask-source separation distance, each event on the detector is geometrically “back-projected” by connecting rays from the x, y position on the detector to locations in the target area. This target area is setup as an accumulator array which is incremented for each event back-projected through a transparent mask element.

Ideal masks possess the bi-level impulse auto-correlation, where the mask serves as its own decoding array. If the mask and decoding array are correlated such that the result is a delta function (shown in the next section), the system output is the best possible estimate of the original object. CAI fundamentals are reviewed in [2],[3],[4],[7],[8].

1.21.2 Mathematics of CAI.

Encoding. Encoding spatial and depth information about a target involves convolving the original object image with the CA mask. Let \times denote convolution and $*$ denote correlation. The object’s projection through the mask on the detector surface creates a distribution

$$P(x, y) = \sum_z [O_z(x, y) \times M_z(x, y)], \quad (1)$$

where $P(x, y)$ is the photon distribution on the detector, $O_z(x, y)$ is the object distribution, and $M_z(x, y)$ is the mask pattern. The mask pattern will be magnified according to the imaging geometry by an amount :

$$m = \frac{(z + f)}{z}, \quad (2)$$

where z is the source-mask separation distance, and f is the mask-detector separation distance.

$M_z(x, y)$ has values of 0 (opaque areas) and 1 (transparent areas). For each incoming photon, the projected mask pattern will be shifted relative to how much the photon's back azimuth has laterally translated away from the axis of symmetry. The detector accumulates $P(x, y)$, whereby every shift encodes the position of the incoming photon and the strength encodes the intensity of the source.⁵

Decoding. To regain the image \hat{O} , $P(x, y)$ must be correlated with a decoding array $A(x, y)$, also magnified according to the geometry of the experimental setup where

$$\hat{O}(x, y) = P(x, y) * A(x, y). \quad (3)$$

Assuming a linear detector response and a planar source distribution we have a linear shift-invariant system where

$$O \rightarrow M \rightarrow A \rightarrow \hat{O}. \quad (4)$$

In this application, the mask M is also used as the decoding array because masks with ideal bi-level autocorrelation properties are implemented. A mask with this property must auto-correlate where

$$M * M = \delta, \quad (5)$$

where δ is an impulse at the origin. The mask, M is related to the underlying ideal mask by

$$M = \frac{(1 + M_{pattern})}{2}, \quad (6)$$

where $M_{pattern}$ has values of +1 and -1 and also retains ideal impulse correlation where auto-correlating results in δ times the number of mask elements N (holes and no holes). Because correlations are commutative an ideal replica \hat{O} is obtained from the original image O in the following manner, where

$$O \times M * M = \hat{O}. \quad (7)$$

The end result is the same when the object is correlated with the mask, convolved with itself. The convolution process and an extension of this imaging process where the mask is in an anti-mask (rotated 60 degrees) configuration are described in Appendix A.

The correlated mask and decoding array, or point spread function (PSF), defines a CA system's imaging capability because it is the system's response to a point source.⁶ The resultant image will have some smearing because no imaging system is truly ideal. If the system input and PSF are known, the system output can be predicted. A complete discussion on the mathematics of CAI and DFTs can be found in [3], [7], [10].

1.22. Metrics Affecting an Ideal Image. Obtaining the best image quality drives the design of both the mask and the reconstruction algorithm. Additionally, the limitations of the detector must be considered. A complete discussion on mask design is in Appendix B. Ideal images have: high contrast, high resolution, and retain geometric accuracy with respect to the original image. This section defines these three measures of image quality, lists how they are optimized, and lists the applicable equations used in this research.

1.22.1. Contrast-to-noise ratio. The CNR is the primary way to quantify image quality and varies according to the amount of signal throughput and both the height and uniformity of the background pedestal. CNR is defined as difference of the peak signal response to a source and the background pedestal divided by the standard deviation of the background. CNR is generally high for point sources and lower for area sources or extended scenes. An empirical derivation for the decrease in contrast for area versus point sources is in Appendix A. Though the decoding process manipulates the signal, it is important to note the CNR is unaffected by these manipulations.

A similar measure of image quality is the signal-to-noise ratio, or the peak signal divided by the background pedestal. It has been shown that both the CNR and SNR give similar measures of image

quality and can be used interchangeably.⁷ In this experiment, both the CNR and SNR are evaluated because quantitative measures of both the contrast and the uniformity of the background pedestal were desired.

The amount of signal throughput, which affects CNR, is determined by the mask's fill factor. The fill factor is the ratio of open area to total area, also equal to the fraction of holes lit up when the detector is viewed from a position other than the actual source position.⁸ High fill factor masks produce better CNR ratios for point sources in the absence of excessive noise. On the contrary, lower fill factor masks produce the best CNR for non-point source targets and extended sources despite the loss in signal throughput.⁹

CNR is improved by reducing the fill factor because the signal is directly proportional, but the noise pedestal is proportional to the square of the fill factor. The contrast (peak – pedestal / pedestal) is given by

$$\left(\frac{1}{ff} - 1\right)\left(\frac{1}{N}\right), \quad (8)$$

where ff is the fill factor for N sources of equal strength. The CNR can also be empirically predicted from using the fill factor alone, equal to:

$$(1 - ff) \sqrt{\frac{A}{N}} \quad (9)$$

Thus, reducing the fill-factor increases the contrast. For example, reducing ff from 50% to 25% increases contrast by a factor of three¹⁰.

1.22.2 Resolution. Resolution is another metric used to analyze image quality that is chiefly dependent on hole size but also varies with mask thickness and the system's PSF. Resolution is defined as the minimum distance between two points on the object's surface where their image is resolved separately on the resultant image.¹¹ Smaller mask holes improve resolution for an imaging system but decrease the available signal. The amount of signal also decreases as you move away from the mask-

detector axis of symmetry. The surface area experiencing gamma ray throughput in this situation is given by:

$$\frac{A_p}{A_T} = \left[1 - \left(\frac{2}{\pi} \right) \left(\frac{t}{r_{hole}} \right) \left(\frac{r_d}{(f + z)} \right) \right], \quad (10)$$

where A_p is the surface area receiving gamma throughput, A_T is the full area of the hole, t is the mask thickness, r_{hole} is the hole radius, r_d the distance from the center of the detector. Equation 10 assumes the source is an on-axis source and is a good approximation. In light of this tradeoff between CNR and resolution, choosing a large number of small holes is the first step in improving resolution at no cost to signal.

Another limit on resolution is mask thickness.¹² An ideal mask would have zero attenuation and be infinitesimally thin. However, real masks are made from high density metals with near perfect attenuation properties. For fabrication and cost considerations, masks are made from the highest density materials possible, but must be reinforced with stronger metals with lower attenuation coefficients to avoid warping. Thicker masks produce holes with collimation effects known as “thickness artifacts.”

The system PSF (and similarly Modulation Transfer Function) limits the achievable resolution because it determines how much smear is produced for a point (and similarly which frequency responses are imaged with good sharpness) in an imaging system. In the mask design process, using target array pixels smaller than the PSF only results in empty magnification.¹³

The FT of the system PSF yields the system’s Modulation Transfer Function (MTF). The system MTF describes an imaging system’s spatial frequency measured in cycles (pairs of lines) per millimeter. The system’s MTF (and PSF) are composed of three individual MTFs (PSFs) from the gamma camera, the mask, and target pattern. Hence, the individual MTFs must be known to determine the system MTF. Because the MTF of ideal masks and point sources are both flat, the MTF of the gamma camera is the main contributor to the overall system MTF. Determining at what cycles per mm the system MTF drops off in sensitivity (by 50%) optimizes the imaging system’s capability to reproduce a sharp image with the

highest possible resolution.

1.22.3. Geometric Accuracy and magnification. An image with ideal geometric accuracy has appropriate dimensions according to the pixel size and the magnification factor of the image.

Furthermore, rigid lines in the object will not appear wavy in the image, nor is there any localized distortion.

The mask's hole diameter determines the magnification effects from source-mask geometry. If two points on an area source are separated a distance d , a distance z from the mask, they will project an image of height D' through a hole of diameter D , as illustrated in

Figure 6.

From geometrical relationships, the detector will display an image of height D' according to:

$$\frac{D'}{D} = 1 + \frac{f}{z} \quad (11)$$

Similarly, the best image possible is obtained when a source of height δ is emplaced at a mask-source distance z , a mask-detector distance of f , using a detector with D' resolution (mm) according to the equality,

$$\frac{\delta}{z} = \frac{D'}{f}, \quad (12)$$

which optimizes the imaging geometry based on the FWHM of the gamma camera. Finally, the whole area being imaged must be projected onto the detector in such a way that it fits entirely inside the detector face plate. The target size, magnified by m (Equation 2), should be less than 0.42 m x 0.536 m for the Anger Camera.

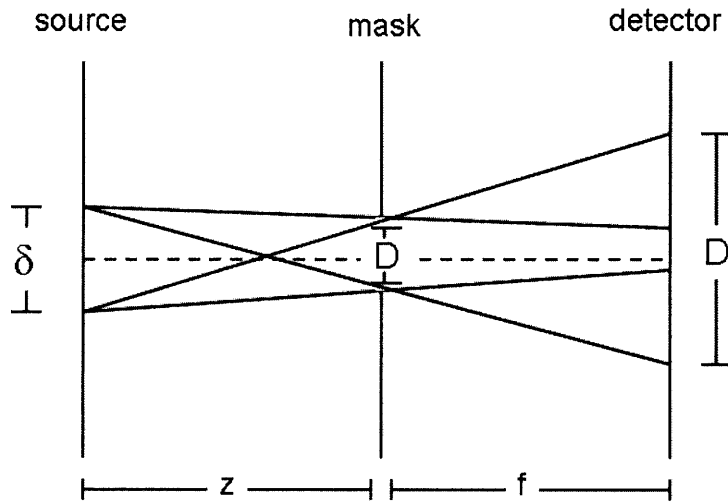


Figure 6. Magnification effects from mask hole diameter. An area source, with height δ will project an image of height D' through a mask with hole diameter D .

1.23. Dynamic Reconstruction. Dynamic Reconstruction generates image sequences from data obtained from moving radiation detection systems. Traditional reconstruction algorithms fail with moving systems because the back-projection is along a single axis and does not allow for relative motion between the imaging system and the target. Here, the process forms images computationally and can recover depth information with sensitivity that drops off with the inverse of distance versus the inverse of distance squared from solid angle calculations.¹⁴ For a complete discussion on DR, see [9].

DR has increased sensitivity and CNR because it affords longer imaging time of the target. Usually, radiation from a source decreases as $1/d^2$ because the solid angle visible by a detector element decreases with increasing radius. But, the sensitivity does not fall off with $1/d^2$ because the source is imaged over a time proportional to the distance between camera and target and thus, will fall off over $1/d$. Given a CAI system and known geometry, each point in the target illuminates the same total detector area through the mask and is then back-projected with an algorithm. Target areas called “accumulator cells” are created in the scene and are incremented or decremented based on input from the algorithm.

Back-projection algorithm. Every photon detected is deemed an “event” by the algorithm and is back-projected through each hole in the mask. The algorithm creates target areas called accumulator

cells located in a 2-D plane at a distance given by the known mask-to-target geometry. It creates vectors which connect all events on the detector surface back to the 2-D target plane. Each accumulator cell receives the same total contributions from the detector elements.

Weighting accumulator cells. Weights are given to the accumulator cells where cells closer to the event are weighted higher than cells further away. In positions away from the source, there will be some contributions to pixels in the back-projection algorithm. However, this “off-target” contribution is lower through multiplication by the mask fill factor. Target cells visible through the mask receive a positive “vote” (one minus the fill factor) and cells not visible receive a negative vote (the fill factor).¹⁵ This weighting scheme cancels the background pedestal because target cells not associated with a source will get equal numbers of positive and negative votes that cancel each other out. The selection of weighting scheme relies on the desired system PSF, noise, and artifact suppression.¹⁶ Error in the gamma camera- the detector readout did not give exact x, y location of events, but was off by 1 to 3 mm. As a result, this system limitation always introduced slight blurring to the reconstructed images.

1.24. Compton Theory. Arthur Compton redefined a more modern view of the photon as a particle of electromagnetic radiation following his precise experiments measuring scattered X-rays’ wavelengths. Qualitatively, physicists understood that X ray penetration decreased following a scattering event. Quantitatively, Compton’s high-resolution X-ray spectrometry experiments showed that the incident and scattered X-rays occurred at two distinct spectral lines. Though Bragg reflection could explain the coherently scattered X-rays, Compton’s theory proved that incoherent scattered occurred, which produced a shift in wavelength proportional to the scattering angle. X-rays, being electromagnetic radiation of very short wavelength, interact with electrons like particles of zero rest mass. Their energy $E = h\nu = hc/\lambda$ and momentum p are related by the relativistic equation for particles of zero rest mass, namely $p = E/c$. Using relativistic mechanics and conservation equations for both energy and momentum, the interaction of an

X-ray quantum and a free electron could be modeled like an elastic collision. Thus, the formula for the “Compton shift” in the wavelength of incoherently scattered X-rays, is

$$\Delta\lambda = \frac{h}{mc} (1 - \cos \theta), \quad (13)$$

where h is Planck’s constant, m is the mass of the electron, and θ is the angle between the trajectories of the incident and scattered photon.

Gamma rays are electromagnetic radiations produced by nuclear interactions. The attenuation of a beam of incident radiation through an absorber material of thickness x is expressed as an exponential relationship:

$$I(x) = I_0 e^{-\mu x} \quad (14)$$

where μ is the linear attenuation coefficient, which depends only on the energy of the incident radiation. μ is the probability per unit path length of an interaction by Compton, photoelectric effect, coherent scatter, or pair production. Each process has a dependence on the atomic number of the absorber and energy of the incident radiation. Compton scattering is defined as the inelastic, relativistic scattering of a photon by a free electron, treated relativistically. For Compton scattering to occur, it is assumed that a photon has energy comparable or greater than the rest mass of an electron.

The energy of a photon after a scattering event is determined by the Compton equation:

$$E' = \frac{E_0}{1 + \alpha(1 - \cos \theta)}, \quad (15)$$

where E_0 is the incident energy, E' is the final energy, α is the fundamental constant, and θ is the scattering angle. The parameter α is a measure of the photon energy in units of the electron rest mass energy (511 keV) and is equal to

$$\alpha = \frac{\hbar \omega}{m_e c^2}, \quad (16)$$

where $\hbar\omega$ is the photon energy (keV), and m_e is the classical radius of the electron.

Lower energy photons are scattered with only a small change in energy, whereas high energy photons (>10 MeV) lose nearly all their incident energy. The minimum energy for the scattered gamma occurs at 180 degrees; it should also be noted that even in the limit of infinite incident energy gammas, the backscattered gamma can never be more than $m_e c^2 / 2$ (255 keV) and never more than $m_e c^2$ (511 keV) for a 90 degree scatter. Our radiation of interest (225 keV X-rays), after backscattering at an angle of 180° , produce final energy is 113 keV from Equation 13. Similarly, for the highest energy outgoing X-rays, the return energy will be a constant at 255 keV.

Klein-Nishina. The probability for Compton scattering at a given angle or energy can be determined by the Klein-Nishina formula. The differential cross section of photons scattered per electron is given by Equation 17:

$$\frac{d\sigma}{d\Omega} = \frac{1}{2} \alpha^2 r_e^2 P(E_\gamma, \theta)^2 \left[P(E_\gamma, \theta) + P(E_\gamma, \theta)^{-1} - 1 + \cos^2(\theta) \right], \quad (17)$$

where $r_e \left(\frac{\hbar}{m_e c} \right)$ is the Compton radius of the electron, and $P(E_\gamma, \theta)$ is the ratio of photon energy before and after collision. For an incident photon of energy E_γ , the following relationship holds:

$$P(E_\gamma, \theta) = \frac{1}{1 + \frac{E_\gamma}{m_e c^2} (1 - \cos \theta)}. \quad (18)$$

Thus, photons with lower incident energies have higher Compton scattering cross sections. A similar phenomenon relates the energy of scattered radiation to the angle of incidence. Near vertical angles of incidence enable X-rays to attenuate deeper through objects before higher probabilities of scatter occur. In the opposite manner, X-rays with a high grazing incidence angle have a higher incidence of

backscatter.¹⁷ When the incident X-rays hit a target plane at an angle, many of the scattered rays are not absorbed and can be deflected as useable backscatter.

Photons within the sodium iodide (NaI) crystal. The NaI detector detects incident photons by the photoelectric effect. Incident photons with energy E undergo a quantum mechanical transition. The photons' final state consists of an excited ion with a vacancy in one of its inner shells where the electron was formerly bound and a free "photoelectron" with kinetic energy $E - W$, where W is the binding energy of the electron in the neutral atom. The photoelectron undergoes multiple coulomb interactions with electrons and nuclei in the sodium iodide crystal and loses all of its energy within a fraction of a μ sec. A small percentage of the lost energy is converted into scintillation light. At the same time, the ion from which the photoelectron emerged loses its energy of excitation through a series of transitions that fill the vacancy in its electronic structure. This process results in lower energy photons or electrons that lose their energy in the crystal and generate additional scintillation light in a cycle.

The total amount of scintillation light in the crystal is closely proportional to the total amount of energy dissipated in the aforementioned processes. As a consequence the pulse height spectrum of a NaI scintillation counter exposed to mono-energetic gamma rays shows a distinct "photoelectric" peak whereby accurate calibration in terms of pulse height versus energy deposited is possible. The counters can then be used to measure the energies of scattered photons and recoil electrons.

1.3 Approach and Objectives of the Project. This research used a four phased method of approach.

- Camera imaging protocols are optimized, a moving mono-energetic source proves that CAI with DR works in the simplest case
- A moving area source allows testing of non-point targets
- X-ray source tests SNR and how well we can image backscatter in the presence of background
- SNR and resolution are optimized leading to final system design

The ultimate objective of this research is to prove that DR can successfully reconstruct extended scenes with wide-area targets where there is relative motion between CAI system and target. Secondary to that main objective, the effects on image quality will be observed when the following parameters are altered:

- mask fill-factor (50%, 25%, 12.5%)
- the outgoing and incoming (backscatter) energy spectrum
- reducing air scatter

After analyzing the image quality of the reconstructions, the optimal fill-factor mask and imaging parameters will be selected. The goal is to optimize resolution and CNR (and SNR) of the resultant images. A CNR above 15.0 (and SNR above 3.0) are desired for the optimized images.

2. APPARATUS AND PROCEDURES

2.1. Apparatus. This chapter introduces the apparatus common to all experiments. The gamma camera, coded aperture masks, and X-ray tube. The gamma camera with mask affixed is the coded aperture imaging system.

2.1.1 Gamma Camera. The ISOCAM II gamma camera¹⁸ has two detector heads, a gantry, a SMARTSCOPE hand control, and an ISOSTATION user entry module. The gamma, or Anger, camera has a 419 mm x 536 mm field of view (FOV) and 2.7 mm spatial resolution (FWHM). The detectors are made of 12.7 mm thick sodium iodide crystal with thallium doping (Na-I (Tl)). The crystals are optically coupled to an array of 86 photomultiplier tubes (PMTs), collectively known as “heads.” Two detector heads are mounted on a rotating drum on the camera gantry. The ISOSTATION controls gantry and camera operation, acquisitions, and storage of acquired images. System specifications for the detector heads are shown in

Table 1.

Table 1. Gamma Camera Specifications.¹⁹ Energy resolution and uniformity values were measured at 140 keV with a count rate of less than 20,000 cps.

Parameter	Specification	Value
Useful Field of View	3/8" Crystal	419 mm x 536 mm
Intrinsic Spatial Resolution	FWHM	2.7 mm
	FWTM	5.1 mm
Intrinsic Energy Resolution		9.5%
Intrinsic Flood Field Uniformity	Integral	±2.0%
	Differential	±1.5%
Multiple Window Spatial Registration Error	Maximum error within the 84keV to 330 keV Energy Window	<0.2 mm
Intrinsic Count Rate Performance (per detector)	20% Window Maximum	230 keps
	20% window	150 keps

Photomultiplier tubes directly behind the crystals detect each photon with x, y location information and the ISOSTATION sums the total counts. The ISOSTATION displays a 2-D image of the relative spatial count density with positional readout quantized to multiples of 0.672 mm.

2.1.2 Coded Aperture Masks. Three coded aperture masks were designed with open areas of 50%, 25%, and 12.5% with associated metrics as shown in

Table 2. The mask design process is covered in Appendix B. Design parameters such as hole size and spacing were experimentally determined as shown in Section 3.1.

Table 2. Mask Metrics for 50%, 25%, and 12.5% fill factor masks used in backscatter experiments.

Mask Fill Factor	Hole Diameter (mm)	Hole Spacing (mm)	Residue	p-value	Total Holes
50%	3.1	3.5	quadratic	5419	10711
25%	3.5	3.9	bi-quadratic	4357	4357
12.5%	1.45	1.625	octic	26041	13021

All three masks shared the basic properties of a HURA with a central basic pattern surrounded by six halves of the same pattern as shown in Figure 7. Tilting the patterns 15° enabled the maximum p-value for each respective fill-factor. The masks were fabricated from 3.2 mm thick, 600 mm x 600 mm

lead alloy sheets chosen for its less than 1% transmission rate for incoming 115 keV X-rays.

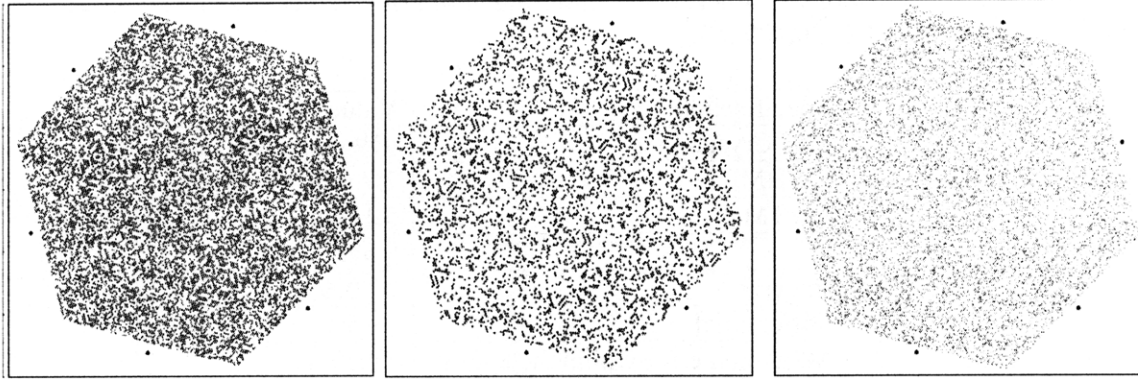


Figure 7. Hexagonal uniformly redundant array mask drill patterns for the a) 50% fill factor mask b) 25% fill factor mask, and c) 12.5% fill factor mask based on quadratic, bi-quadratic and octic residues. Tilting the patterns by 15° allowed the maximum number of holes per mask.

The masks were mounted parallel to the detector and object plane as shown in Figure 8. A trapezoidal lead box shielded the detector from background noise. As shown in Figure 8, the gamma camera with affixed mask constitutes the coded aperture imaging system described in all experiments.

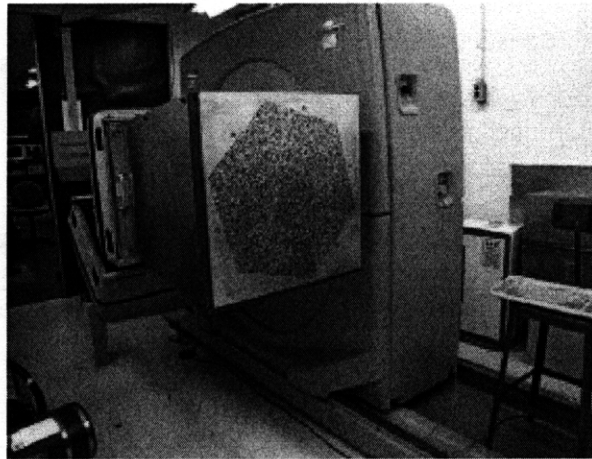


Figure 8. Coded aperture camera with hexagonal mask affixed to the gamma camera's detector head using a trapezoidal lead shield.

2.1.3 X-ray Tube. A 225 kV, 13.5 mA X-ray tube was provided by American Science & Engineering, Billerica, MA. The pallet-mounted system consisted of the X-ray tube, a 220/240 V 60 A high voltage

power supply (HVPS), a 230 V, 3.5 A chiller, and a 220 V, 0.5 A, controller. In order not to saturate the Anger camera (~250 kcps with no mask and ~500 kcps with mask) the X-ray tube's output was reduced with lead filters with varying thicknesses ranging from 1/16 in to 3/16 in. Before daily operation, a 17.5-min warm up sequence was run in order to stabilize the system for operation. When the tube was not used for greater than 7 days a 75 min warm-up was run.

2.2 Procedures. This chapter reviews conduct of the 4 phases of this research: preparation for imaging, proof-of-principle with a point source, proof of principle imaging an area source, and X-ray backscatter tests. The preparation phase included lab preparation and equipment calibration. Phase II used existing coded aperture masks to prove dynamic reconstruction (DR) would work with the simplest case of imaging a mono-energetic point source in a near field experiment. This phase also included tests to finalize the mask design. Phase III tested a mono-energetic area source to shape test non-point like objects in the absence of problems that would later be introduced by backscatter in Phase IV. Phase IV attempted to optimize the DR of an image produced by backscattered radiation by examining mask open area, effects of changing target parameters, and other spectral considerations.

2.2.3 PHASE I. Lab preparation consisted of cleaning and radiation protection hardening of the site. Equipment preparation included gamma camera calibration, verification of camera imaging capabilities, selection of optimal imaging protocols, target fabrication, and confirmation of the X-ray backscatter spectrum.

2.2.3.1. Lab Preparation. The lab room was first prepared by removing unused equipment and given a thorough cleaning to remove particulates that could later interfere with backscatter. The experimental apparatus was setup as shown in Figure 9.

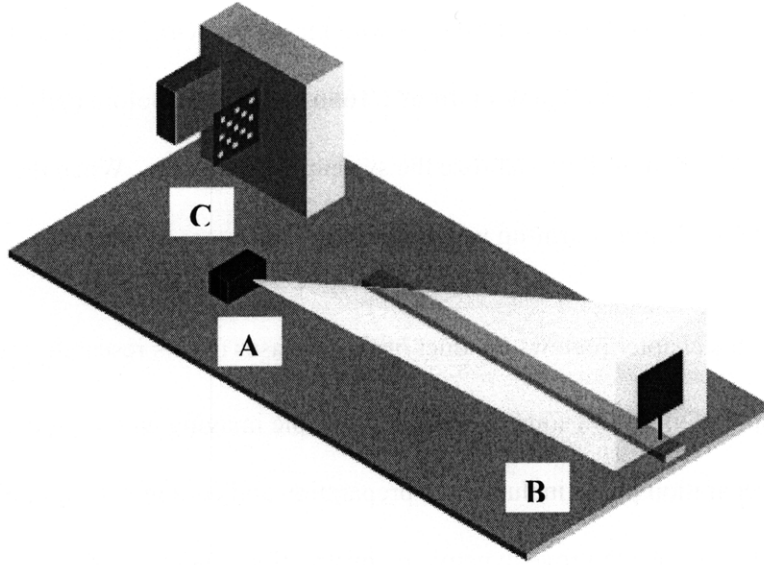


Figure 9. Geometry of initial gamma camera experiments. The X-ray tube (A) was positioned with the cone beam illuminating a target (B) at the far wall. Backscattered X-rays were directed through the coded aperture into the gamma camera's detector (C).

The coded aperture mask was mounted on a trapezoidal lead shield affixed to the gamma camera's detector head. The X-ray tube was positioned with a 750 mm diameter cone beam illuminating the target, approximately 5 m away at the wall. Targets were mounted on a remote-controlled carriage (or tug) that moved the target from 5 m to 2 m from the detector surface during data acquisitions. The planes of the detector head, mask, and target were checked to ensure they were parallel and level $\pm 2^\circ$ with respect to both the horizontal and vertical. The camera's output data were collected at the ISOSTATION for batching and subsequent input to the dynamic reconstruction algorithm.

A 195 mm thick, concrete radiation shielding wall was erected behind the target. This thickness was determined from attenuation calculations to reduce the potential dose to the public to less than two mrem/hr as required by RPO. The dose rate was never greater than two mrem per hour outside or inside the vault except directly in the cone beam. Outside of the vault, the maximum dose rate was about one mrem per hour behind the back wall in the path of the beam. To reduce backscatter from the concrete, a 2.5 mm thick plate of steel was placed against the concrete facing the target. A lead collimator was fabricated to produce a cone beam that concentrated the X-rays on the target and reduced the dose to the

operator during operation. Additionally, a 150 A breaker was installed in the room to support the X-ray tube's power requirements.

2.2.1.2. Equipment Preparation.

Gamma Camera System Calibration and Quality Control Testing. To ensure the system was functioning properly and at the desired energy ranges, the manufacturer recommended calibrating the system. First, the PMTs in both heads were each calibrated with a 3.5 mCi Tc-99m source. Then, an internal energy correction was performed. Finally, uniformity corrections were run on both heads using 500 μ Ci of Tc-99m placed 3000 mm away. The system was calibrated for running at count rates between 10,000 to 30,000 cps. To confirm the system was calibrated properly, the aforementioned Tc-99m source was imaged. The camera's peak energy spectrum was confirmed at 140 keV by observing the displayed "quality assurance (QA) peak" at 140 keV with energy windows were set at 20%. QA flood field images were run to check for subtle non-uniformities and to ensure that the uniformity corrections removed them. Geometric accuracy and resolution were checked by imaging a four-quadrant bar pattern with known separation distances, discussed in the next section.²⁰ Finally, the ISOCAM workstations were replaced with SUN™ CPUs with increased memory because the gamma camera was being used in a manner for which it was not originally designed. The camera would be used to take hundreds of data-intensive static images in a sequence.

Verification of Camera Resolution and MTF. The gamma camera's intrinsic spatial resolution was verified by imaging a mono-energetic source through a standard 4-quadrant bar phantom with 2.0, 2.5, 3.0, and 3.5 mm wide lead bars as shown in Figure 10. This experiment also tested for response uniformity and geometric accuracy. First, a background measurement was first taken for subtraction. The phantom was placed directly on the detector while imaging a 10 ml vial filled with 3.5 mCi of Tc99m. Gamma camera output header (.hdr) files from the test images quoted 0.672 mm per pixel. These trials experimentally confirmed this effective pixel size in mm. Three trials were conducted at matrix size 256 x 256, 512 x 512, and 1024 x 1024. Files were saved as Interfile 3.3 with data acquisition

information saved in a separate header file.

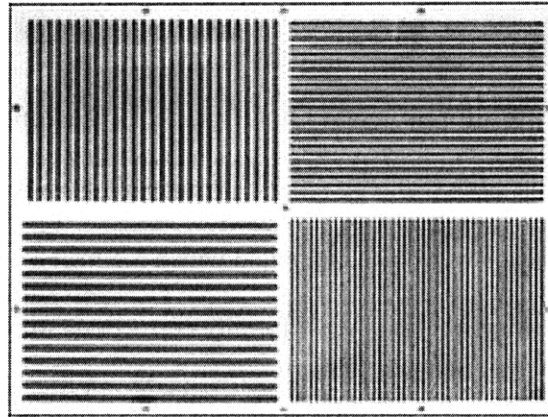


Figure 10. 4-Quadrant lead phantom used to verify gamma camera spatial resolution and linearity. The quadrants have 2.0, 2.5, 3.0, and 3.5 mm wide lead bars.

Determining the gamma camera's MTF was vitally important for two reasons. First, knowing the camera MTF is required to accurately restore the original image in the deconvolution process. Second, the gamma camera's MTF needed to be analyzed to support the mask design's hole separation distance. The MTF would be examined to see how the response dropped off with increasing frequency. From the results of the grating experiments, a target hole separation distance of 3.5 mm was examined first.

The MTF was obtained by imaging a preexisting, coded aperture mask and taking the FT of the magnified mask shadow. The mask was a 62 x 62 array, Modified Uniformly Redundant Array (MURA) with square holes spaced 2.2 mm apart. The mask was mounted on a lead-shield with 356 mm mask-detector separation distance. A magnification of 1.58 was required for the mask shadow to have 3.5 mm hole spacing. Accordingly, Equation 2 required positioning of the source 610 mm from the mask surface. The source was a full 10 mL vial of 3.5 mCi Tc99m, collimated in a lead cylinder with a small aperture. The cylinder was placed on its side with the aperture directed toward the center of the mask. One 5 million-count acquisition was taken and the gamma camera output was given in 1024 x 1024 matrix size. The MTF of the detector output pattern served as a close approximation to the MTF of the gamma camera. The MTF was then analyzed for frequency response and rotational symmetry.

Determination of Imaging and Reconstruction Sequence. Each of the camera's preset internal imaging protocols was run to determine which imaging sequence best supported the metrics desired for the backscatter experiments. Three prefabricated masks and multiple point sources were used to perfect the imaging sequence and achieve the highest resultant image quality. The Anger camera's "Hepatobiliary" study type and "isotope" study mode were selected because multiple static acquisitions were possible with the detector heads in any user-defined position. The uniformity correction mode, "Single Isotope", was selected because it produced the clearest images. Tests were also run to determine which resolution to use for future imaging. Test images were taken at 256 x 256, 512 x 512 and 1024 x 1024 to qualitatively investigate what resolution was suitable. The optimal images had 1024 x 1024 matrix size and at least one million total counts.

The reconstruction sequence consisted of file saving, post-processing, decoding by an appropriate algorithm and analysis. All files were saved as Interfile 3.3 and burned to CD for transfer to a laptop computer. The interfile formats were converted to bmp images by an executable file. The bitmap images were inputs into the reconstruction algorithm, which output the reconstructed images of the original target. Those images were analyzed both in a stand alone format and as part of a gif sequence simulating relative motion. A final, fielded system of this type would have faster one-step processing. However, due to equipment and processor constraints post-processing was necessary. Of utmost importance was the successful demonstration of the DR technique.

Target Selection and fabrication. Targets for the backscattered X-ray experiment consisted of polyethylene and water because both materials have low X-ray attenuation coefficients. Backscatter count rates from successive additions of 250 mm-thick polyethylene sheets were measured to determine optimal target thickness. X-ray backscatter targets are shown in Figure 11. A 76 mm-thick polyethylene arrow (height 584 mm, arrowhead width 355 mm) and annulus (outer diameter 350 mm, inner diameter 80 mm) were fabricated in order to test resolution, depth perception, and sharpness along defined edges. A 5-gallon water jug (diameter 305 mm, height 560 mm) was added to explore backscatter from

cylindrical objects.

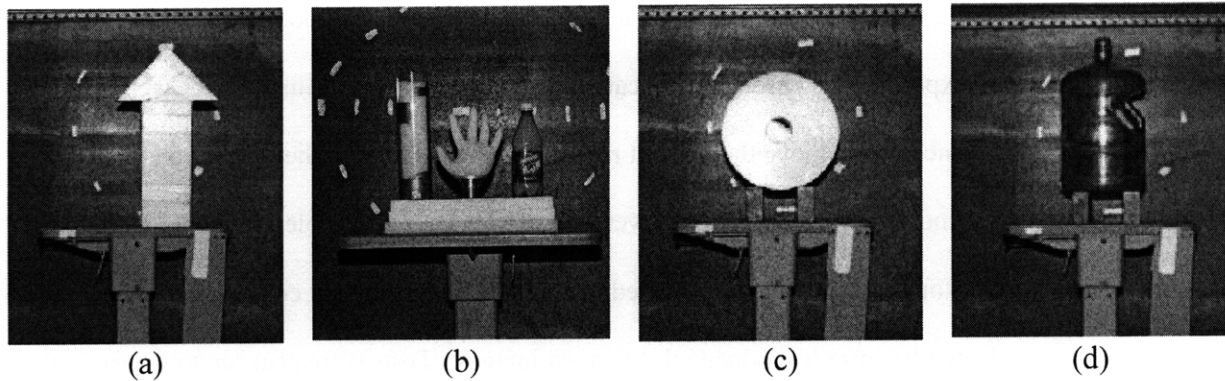


Figure 11. Targets used for X-ray backscatter experiments. Polyethylene was used to fabricate an a) arrow, b) an annulus, and c) multiple object scene. Because of water's similar attenuation properties water-filled 5-gallon water bottle, shown in d) was also used.

Additionally, polyethylene resin beads and water were used to fill smaller objects such as a glove, a cylinder, and bottle for a multiple-object scene. For the area source tests, 6 mm-thick lead shapes partially occluded the surface of a 5 mCi, 610 mm x 419 mm active-area Co-57 area source as shown in Figure 12.

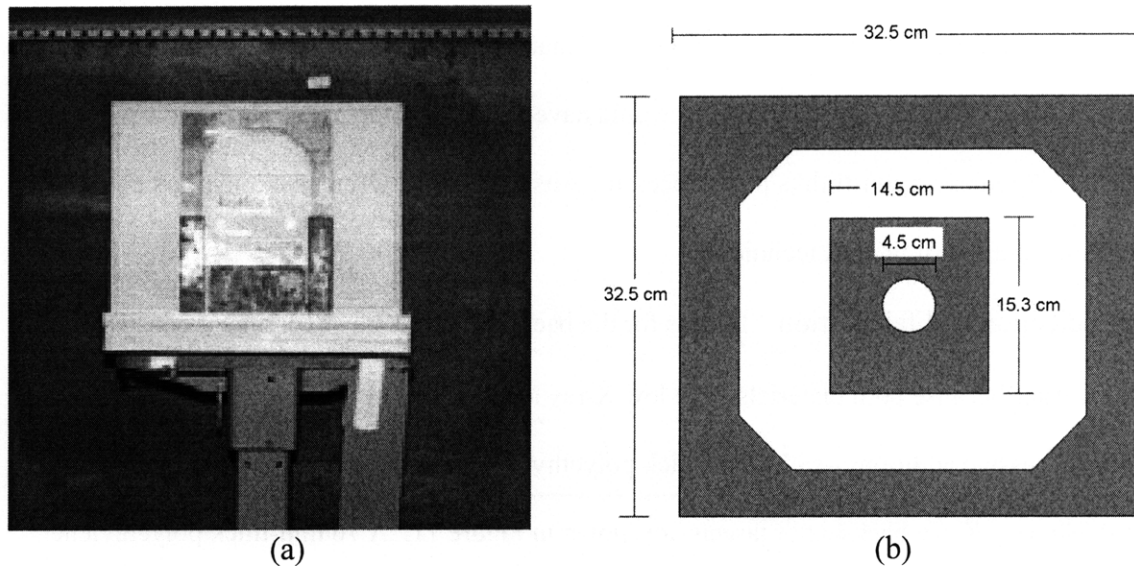


Figure 12. Lead shields used to partially occlude the area source during acquisitions. The same hexagonal cutout shown was used in a) the 50% and 25% fill mask tests. The 12.5% mask tests added a smaller lead cutout in b) to aid in resolution testing.

Confirmation of X-ray Backscatter Spectrum. The energy spectrum of backscattered radiation was simulated and confirmed using an HPGe detector. First, the outgoing beam was simulated with the Monte Carlo radiation transport code Geant 4 9.0²¹. Next, the spectrum was experimentally verified using a Canberra 3 in crystal intrinsic Germanium detector with MAESTRO software. The X-ray source was run at 225keV and 0.3 mA. The outgoing beam backscattered from 100 mm of polyethylene placed 5 m away. The HPGe detector crystal was placed directly in front of the mask.

2.2.2 PHASE II. Phase II consisted of proof of principle using a point source. Additional objectives included: examine setup geometry, test the reconstruction algorithm's performance, test the FOV and system PSF, examine artifacting, and attempt to identify and remove any systematic errors. Phase II was complete when the CAI system, with 50% fill mask, had been optimized with a point source.

Preparation. The gamma camera was prepared for imaging by initializing the uniformity corrections for 345 mCi of Tc99m. The imaging mode was set to dynamic, obtaining 10^6 total counts per image. A 10-ml vial of Tc-99m, collimated in lead cylinder (160 mm tall and 75 mm diameter with 5 mm-diameter aperture) was placed along a 3000 mm track running perpendicular to the mask at its centerline. A temporary mask holder, fabricated from lead and concrete, was used to shield background radiation. The mask-detector distance, f , was 450 mm for the duration of Phase II testing. The mask magnification and source activity was used to determine the optimal ranges of z to keep the count rate below 50,000 cps to not overwhelm the detector. A far sequence, with z -values between 2000 and 3000 mm, was examined. To test the effects of magnification on resultant images, a near sequence with z -values between 1000 and 2000 mm was also imaged.

Testing. 9 acquisitions were taken in dynamic mode at 1024 x 1024 matrix size. The far sequence (acquisitions 1 through 5) had z -values of 2000, 2250, 2500, 2750, and 3000 mm. Z -values were measured along the floor with a tape measure. The near sequence (acquisitions 6 through 9) had z -values of 1750, 1500, 1250, and 1000 mm. The average count rate for each set was 7800 cps.

Acquisitions lasted between 40 to 100 seconds per frame depending on z. Images were saved and reconstructed according to the method described in Section 2.1.

Analysis. The reconstructed image represented the system PSF. The image's SNR was also evaluated. Numerical tests were run to check mask-source alignment and sensitivity to errors in rotation or distance. Last, the reconstructed images were compiled as gif animations to examine drift.

2.2.3 PHASE III. Mono-energetic Area Source Tests

2.2.3.1 Objectives. The CAI system imaged a partially occluded mono-energetic area source to test non-point like imaging in the presence of background but not backscatter. Proving that imaging area sources was possible was necessary to demonstrate that this technique could image complex scenes prior to adding the problem of backscatter. The approach consisted of imaging the target, shown in Figure 12a, placed on the tug and imaged sequentially with varying z-values. The target was tested with each mask for proof of principle with a mono-energetic source in the absence of backscatter. Next, the target was imaged with the 25% fill mask to investigate system sensitivity to angle of incidence. Energy windowing was also investigated as a method to remove air scatter in support of future X-ray backscatter tests. Accordingly, image quality was further optimized during this phase of testing in preparation for X-ray tests. The experiment geometry is shown in Figure 13.

12.5% fill factor mask. 10 acquisitions of the 2.8 mCi area source target with extra lead cutout, Figure 12b. were taken with z-values ranging from 4866 to 615 mm in roughly 500 mm increments as shown in Table 3. More acquisitions were taken with this mask because we were testing resolution and contrast for the octic-residue mask under conditions not limited by the gamma camera's 4 mm FWHM resolution. Further, testing for mask magnification and self-collimation effects required more acquisitions to analyze both individual frames as well as gradual changes in the animated sequence. Closer camera-target distances were also used to simulate having a higher resolution camera or a larger detector and examine resultant effects on image quality.

Table 3. Acquisitions for the 12.5% fill factor mask. Tests with the octic-residue mask sought to investigate resolution, magnification, and mask self-collimation which required analysis of multiple frames stand-alone and in an animated sequence.

Acquisition	1	2	3	4	5	6	7	8	9	10
z (mm)	4866	4349	3777	3462	2992	2502	1999	1499	998	615

2.2.4 PHASE IV. X-ray Backscatter Tests

2.2.4.1. Objectives. This phase of tests sought to:

- investigate large area CA masks to image wide scenes and area targets
- evaluate usefulness of 50%, 25%, and 12.5% fill factor masks
- develop a DR algorithm and demonstrate it for each large area CA mask
- optimize the CAI system and imaging process, and
- determine the SNR and resolution of optimized CAI system.

Pre-existing limitations of CAI and reconstruction drove the testing methodology. Limited flux from backscatter requires large area, high resolution (less than 20 mm) masks with an efficient detector. The detector typically must operate in pulse counting mode with a low pulse floor. Even with standard CA imaging, the system is permitted to stare for minutes or hours per image. Here, shorter imaging times are required. In addition, the targets are complex, area targets in a noisy environment from backscatter versus the sparse scenes against minimal background in typical CA imaging. The DR algorithm must account for rapid changes in scene and geometry. Further, the algorithm must be able to account for some

system vibration, as no system under normal operating conditions would be a pristine platform.

2.2.4.2. Experiments. A summary of experiments for each mask fill factor test series is shown in Table 4. System calibration with a point source preceded each test series. Next, the quality of the initial image was optimized with successive modifications to the DR algorithm for each mask. Initial tests were all for proof of principle and resulted in a working (though not optimized) DR algorithm for each mask. Results from each mask’s initial test determined follow-on tests to investigate how changes on the system optimized image quality. “Image optimization” consisted of increasing the signal, reducing the noise, resolution improvement, and artifact reduction. Subsequent tests re-imaged the same wide-area targets for direct comparison.

Table 4. Summary of Experiments for X-ray Backscatter Experiments. Initial images were taken with each mask for proof of principle. Follow-on tests optimized image quality.

Experiment	Mask fill-factor test series		
	50% quadratic residue	25% quartic residue	12.5% octic-residue
Initial	Imaged wide-scene targets to test standard fill-factor CA Response	Imaged wide-scene targets to confirm lower fill-factor CA produced better results over 50% mask	Testing of arrow target for direct comparison to 25% mask
2	Modified gamma camera imaging protocols and DR algorithm to optimize images	Changed energy spectrum shape <ul style="list-style-type: none"> • decreased tube filtration • widened cone beam by shortening collimator 	Imaged multiple objects in one scene for direct comparison to 25% mask
3	Changed source and detector geometry to reduce air scatter	Imaged multiple objects in one scene to test limits of resolution	Tried post-processing “smoothing” to increase contrast
4	Mask / Anti-mask	Tested all resolution “matrix sizes” to determine minimum required	Self-collimation w/ area so & pt so

The geometry for the X-ray tests is shown in Figure 14. Mask-detector distance remained fixed for all experiments. The mask-target distance and other applicable distances were modified for each test as described in the following section.

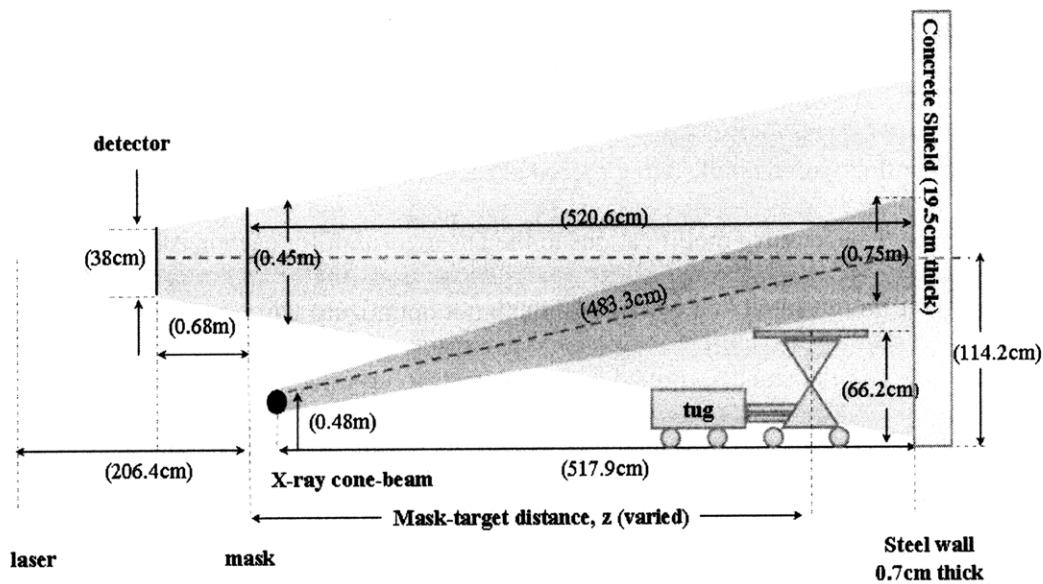


Figure 14. Experiment geometry for X-ray backscatter tests. Mask-detector distance remained fixed. Mask-target distance was varied according to each experiment. The source illuminated an area 600 mm in diameter against the wall.

50% fill factor mask. Initial tests examined reconstructions from the quadratic mask, which is the standard open-area mask used in CA imaging. Experiments with the 50% fill mask sought to establish a baseline imaging technique from which systematic errors in the imaging and reconstruction process were identified and ameliorated. First, a single-frame reconstruction of the water jug ($z = 5179$) was obtained to confirm the DR algorithm. Two acquisitions were obtained with five million and one million total counts to determine a minimum number of total counts per image for acceptable image quality. All later acquisitions were conducted with at least one million counts per image. Next, multiple-frame reconstructions were attempted with the water jug and polyethylene rings. The water jug was imaged six times from $z = 4770$ to $z = 5185$ mm in 80 mm increments. Then, 14 acquisitions of the rings were taken from $z = 4315$ to $z = 4815$ mm in 100 mm increments for the first four images and then 20 mm increments for the remaining ten. The rings were first imaged on top of two 600 mm x 600 mm polyethylene sheets to increase the amount of detected backscatter. Then, the rings were re-imaged at $z = 4815$ mm after removing these backdrop sheets to reduce the noise.

Second, four acquisitions of the arrow were taken to ensure previously optimized imaging protocols for the area source tests were still applicable in the presence of increased scatter. The following protocols were tested:

- widening or narrowing energy windows
- tests effect of using energy bands on Anger camera
- changing source type from “Spectral” to “Isotope”
- changing uniformity correction type (point source, area source, and X-ray)

in order to test which camera protocols were most effective in producing the sharpest image with backscattered X-rays as the source. The gamma camera’s energy banding feature enabled the camera to split a specified energy window into a user-specified number of narrow slices for analysis of multiple smaller windows. After the optimal imaging protocol was selected, the DR algorithm was tested for depth and rotational accuracies.

The third test sought to reduce the amount of air scattered radiation that was detected as un-encoded noise. The experiment geometry was altered by moving the source closer to the wall and the gamma camera further away. The source to wall distance shown in Figure 14 was decreased to 1988 mm and the laser-to-mask distance was decreased to 4748 mm. The water jug was re-imaged along the aforementioned 500 mm track at the same six distances. Additionally, the arrow was imaged five times from $z = 4962$ to $z = 5230$ mm in 80 mm increments. The arrow was imaged at higher z -distances because the height of the arrow forced the “arrowhead” out of the cone beam as it progressed along the track.

To determine how well mask and anti-mask coupling would improve image quality, six acquisitions of the arrow were taken in 500 mm increments along the track. The same acquisitions were repeated with the anti-mask (mask rotated 60 degrees.) The highest quality reconstructed mask and anti-mask images were averaged. The method of mask and anti-mask averaging is fully developed in Appendix A.

After image optimization was complete, CNR and SNR were calculated for each target. The system resolution was determined with the optimized CAI system (25% fill factor mask).

25% fill factor mask. The initial tests imaged both the arrow and water jug to confirm the bi-quadratic mask's performance. Gamma camera imaging protocols optimized during the previous 50% fill experiments were left in place. Both the arrow and water jug were imaged four times along a 240 mm track in 60 mm increments. In addition, the water jug was imaged in two separate ways. For the first two acquisitions, the water jug was placed against the back wall on two lead bricks. This placement ensured the jug was illuminated by more of the beam. Next, the jug was imaged twice on three horizontal polyethylene sheets to test an object that had both rounded and flat backscattering surfaces.

After a working CAI system with 25% mask was confirmed, tests were run to examine effects of altering both the beam's outgoing spectrum and the camera's incoming spectrum. The next tests were conducted with increased count rates and to examine the effect of altering the energy spectrum. First, the outgoing energy spectrum was altered by reducing the tube filtration. Reducing the tube filtration narrowed the energy spectrum. The X-ray cone beam was widened by shortening the lead collimator from 124 mm to 77 mm. The wider cone beam illuminated a larger FOV at the target, hence producing more detectable photons. Shortening the collimator had secondary effects of increasing air scatter and altering the energy spectrum. Accordingly, these tests examined the bi-quadratic mask's reaction to changes in the energy spectrum and the ability to shield against increased air scatter. Further, the tube's filtration was reduced from 4.76 mm (3/16 in) to 3.18 mm (1/8 in) to increase the count rate. Additional shielding was added to the tube at this time to reduce X-ray leakage from the tube that produces un-encoded noise at the detector.

The incoming energy spectrum was altered by altering the energy windows and source geometry by moving the source closer and camera further.²² All the targets described above were re-imaged under these conditions to observe effects on image quality. After the 25% fill CAI system was optimized, a final test imaged one scene containing a polyethylene cylinder, a water-filled glove, and an 8-oz plastic beverage bottle, shown in Figure 11b, to investigate illuminating multiple objects with the wider cone

beam. Last, SNR and resolution were calculated for the different targets. Because the 25% fill factor yielded the highest quality images, different gamma camera resolution settings (matrix sizes) were investigated to determine the minimal resolution required for a final system. Picking the lowest possible matrix size would speed up the reconstruction algorithm. The possible matrix sizes investigated included 64 x 64, 128 x 128, 256 x 256, 512 x 512, and 1024 x 1024.

12.5% fill factor mask. The first test with the octic residue mask sought to verify that increasing p to 26041 (octic residue) increased the number of pixels in the final image. All gamma camera optimized settings were left unchanged for the duration of testing with this mask. The arrow target was imaged at $z = 4781$ mm for direct comparison to the 25% and 50% fill images.

Next, the multiple object scene described in Section 4.2.2 was re-imaged for direct comparison. Image post-processing algorithm modifications were investigated for possible improvements to image quality. The multi-scene results were smoothed in an attempt to achieve image quality commensurate with the 25% fill factor mask results.

Results from the first and second octic-residue tests in Table 4 indicated results may have been skewed due to mask self-collimation because the hole diameters were similar to the mask thickness. Both the area source and point source were re-imaged 10 times along a 5000 mm track in roughly 500 mm increments to confirm or deny the presence of self-collimation effects. After the presence of these self-collimation effects were confirmed, CNR and SNR were calculated. The arrow reconstruction was used for the contrast analysis because it was the best quality. Additional targets were not imaged because this mask would not be recommended for use in a final system due to poor image quality.

3. RESULTS

3.1 PHASE I.

3.1.1 Verification of Camera Resolution and MTF. To quantitatively confirm the gamma camera spatial resolution listed in

Table 1. For each quadrant, the pixels spanning one cycle of line intervals were counted as listed in

Table 5. One cycle (or wavelength) is defined as one opaque and one transparent bar. The wavelength was obtained by multiplying the number of pixels per cycle by the scaling factor (0.672 mm per pixel) given in the 1024 x 1024 image .hdr file. Signal-to-noise ratios were also calculated by averaging the signal along the bright and dark strips, then taking the ratio. The wavelengths, when divided by two, produced bar widths all within 1.2% error as shown in both quantitatively and qualitatively in

Table 5 and **Figure 16**, respectively.

Table 5. Determination of wavelength from four-quadrant bar phantom to confirm gamma camera spatial resolution. Calculated lead strip widths matched the actual widths (2.0, 2.5, 3.0, and 3.5 mm) indicating at least 3.0 mm resolution and 3.0 mm hole spacing for the mask design was a plausible result.

Quadrant	pixels/cycle	wavelength (mm/cycle)	calculated bar width (mm)	signal-to-noise ratio
Lower Left	10.53	7.08	3.54	4.50
Upper Left	8.97	6.00	3.00	2.37
Upper Right	7.53	5.02	2.51	1.75
Lower Right	6.02	4.03	2.00	1.45

The image was also qualitatively assessed for contrast. Though the bar pattern in all four quadrants was visible, overall contrast drastically decreased with decreasing wavelength as shown in Figure 16. In the lower left quadrant (3.5 mm bars), the lines are well delineated and contrast is high. Conversely, the lower right quadrant (2.0 mm bars), the lines are noticeable but blurred together. In

ascending order, the 2.0, 2.5, 3.0 and 3.5 mm quadrants had 10%, 20%, 32%, and 42% contrast with respect to the ideal.

The quadrants with bar widths of 3.0 mm and higher had the best geometric accuracy and response uniformity. At the image's left and right edges there is visible line waviness and spatial variation of the spacing between lines as shown in Figure 15. Further, the hexagonal pattern of the underlying PMTs is noticeable in each quadrant, though most pronounced in the upper and lower right quadrants because of the finer spacing between bars. Within each PMT, the response varies spatially with maximums at the PMT center and minimums at the boundary.

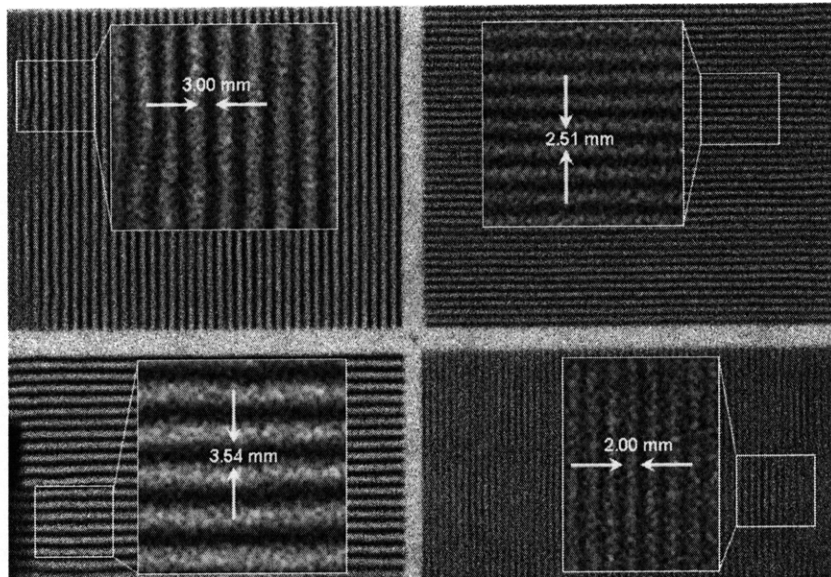


Figure 15. Anger camera resolution was verified with a point source and a lead grating mounted in front of the camera. The lower right quadrant suggests imaging gratings finer than 3.0 mm was possible. Image matrix size is 1024 x 1024 with 0.672 mm per pixel scaling factor.

The signal-to-noise was calculated in each quadrant and plotted versus wavelength (mm) in Figure 16. Images with SNR greater than two were desired for the final system. Only the 6.00 and 7.08 mm wavelength quadrants had SNRs higher than two as shown in Figure 16. However, resolution is optimized by using the smallest diameter hole. So, the wavelength of 6.00 mm was selected as the threshold. A wavelength of 6.00 mm (3.0 mm wide bars) implies the final mask design should have a

similar wavelength. Thus, hole spacings of 3 mm or higher were adequate to ensure optimal image quality.

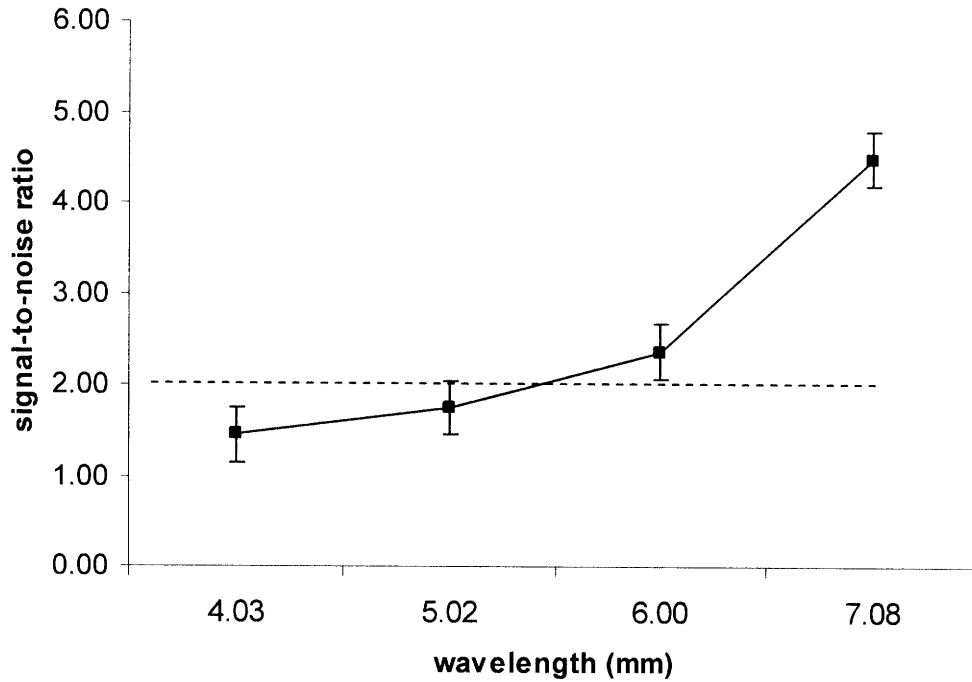


Figure 16. Signal-to-noise (SNR) versus wavelength (mm) where the quadrants with 3.0 mm (6.0 mm wavelength) and 3.5 mm (7.08 mm wavelength) spacing had SNR above the 2.0 threshold (dashed line). A solid line connects data points to aid the eye.

MTF. The magnified mask shadow and its FT are shown in Figure 17. In Figure 17a, the mask shadow was magnified 1.58 times from experiment geometry. The mask shadow is 322 x 322 pixels corresponding to 216 mm x 216 mm. Hence, the lowest frequency in the FT (Figure 17b) is one cycle per 216 mm. The four bright points at the edges of the FT along the horizontal and vertical axes represent aliases of zero frequency. These points are 62 steps from the origin, or 62 cycles per 216 mm which correspond to one cycle per 3.49 mm.

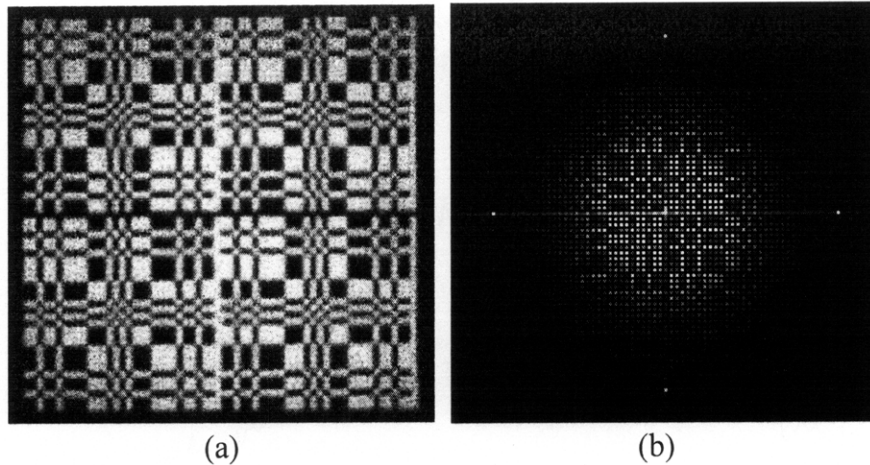


Figure 17. A preexisting 62 x 62 a) mask shadow (magnified 1.58 times from imaging geometry) and b) the central part of its FT representing the system Modulation Transfer Function.

The DC response, though suppressed in the center of Figure 17b, has an amplitude approximately 30 times the amplitude of the other components. Ignoring this large DC response, the MTF at low frequencies is approximately 3 and decreases to approximately half at 28 steps away from the origin. This equates to 28 cycles per 216 mm, or one cycle per 7.7 mm.

The FT is symmetric about the origin with a pattern that resembles the mask hole pattern. Every second row and column in the FT are zero because the mask has a 2 x 2 repetition of the basic pattern exhibiting even harmonics.

3.1.2 Confirmation of X-ray Backscatter Spectrum. The energy spectrum of backscattered radiation was experimentally confirmed using an HPGe detector. From Equation 15, an outgoing X-ray at 225 keV would produce backscatter at approximately 119 keV. The backscatter spectrum, acquired with the Germanium is shown in

Figure 18. The peak is centered about 114 keV, slightly skewed to the left due to low energy lead X-rays. Accordingly, all future acquisitions had 20% open energy windows centered about this peak energy. The 102 to 125 keV energy window limited low energy noise from the lead X-rays that peaked at 85 keV.

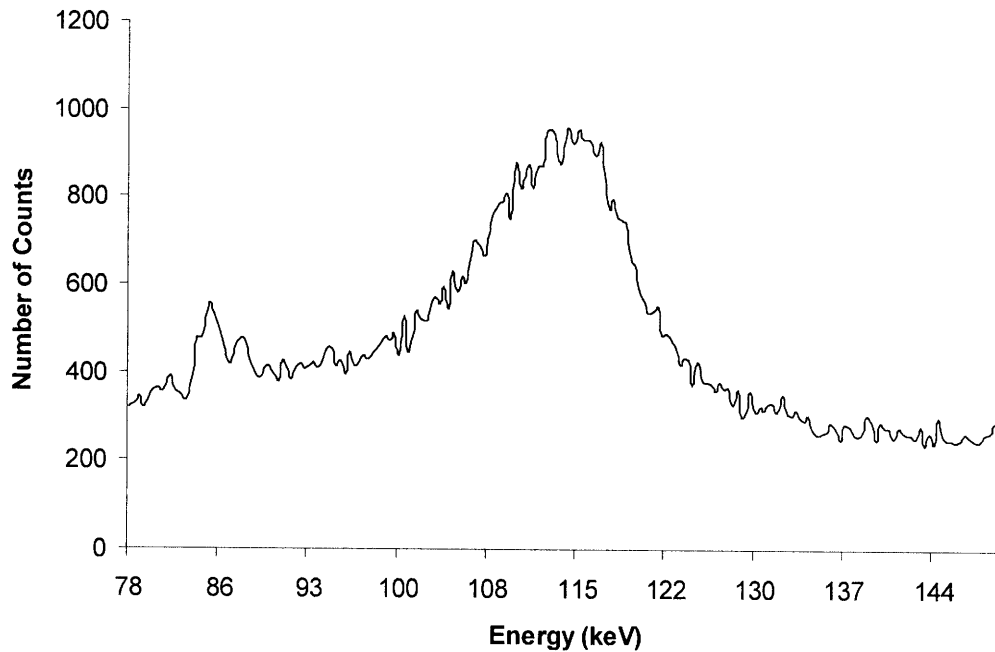


Figure 18. 225 keV X-rays produced a backscatter energy spectrum centered about 114 keV. All future experiments were run with 20% open energy windows centered about this energy.

3.2 PHASE II: Proof of Principle.

The reconstructed point source using the 50% fill aperture is shown in Figure 19, demonstrating the imaging technique and reconstruction algorithm worked with the new mask. The gamma camera outputs (798 x 626) were reconstructed to bmp images (128 x 128) and enlarged by a factor of two for display purposes. The reconstructions were later compiled in a sequence to examine changes as a function of changing z . Image FOV size was 1600 x 1600 mm for all reconstructions in this sequence.

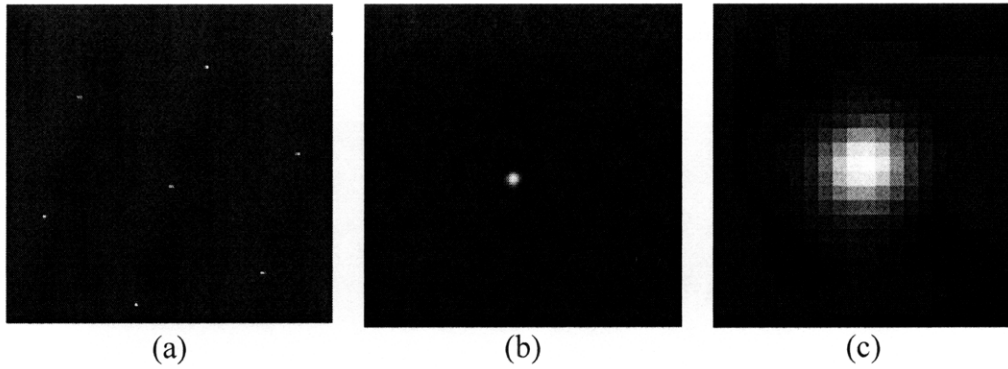


Figure 19. Reconstructed point source with 50% fill mask. The full HURA FOV was utilized in the back-projection producing (a) a central point surrounded by additional copies because of the repeating basic mask pattern. The central point represents b) the system PSF shown in c) enlarged 1200%.

The full HURA mask, with central basic pattern surrounded by 6 half-copies, was used in the back-projection. Consequently, Figure 19a shows a central point surrounded by additional copies of the source. The reconstructed point in Figure 19b represents the system PSF. The system PSF, shown enlarged 1200% Figure 19c is 12 pixels across and 12 pixels tall with a FWHM of about 8 pixels across. 4 mm per pixel corresponds to 32 mm at the target, located 5000 mm away. 32 mm normalized by the magnification factor ($700 \text{ mm} / 5000 \text{ mm}$) gives a system PSF of 4.5 mm on the detector.

In the sequence, the PSF “blob” experiences slight elongation in the vertical direction with increasing z . This appears to be due to a small change in imaging geometry. There are also small but noticeable artifacts in the background. The artifacts worsened when the detector output data was block-averaged or down-sampled in efforts to reduce the computational load. When viewing the reconstructed images as a sequence, there was some apparent lateral drift of the target that is more pronounced in the far (2000 to 3000 mm) sequence.

The magnified mask shadows from both the far (2000 to 3000 mm) sequence and the near (1000 to 2000 mm) sequence are shown in Figure 20. Individual holes in the mask shadow are resolved and geometry was preserved. There were no shifting of lines and symmetry remained about the horizontal and vertical axes. As z decreased, target resolution improved. The blurriness surrounding the target faded and echoes appeared with decreasing z -values. The resolution improved until the target reached

2000 mm mask-target separation distance.

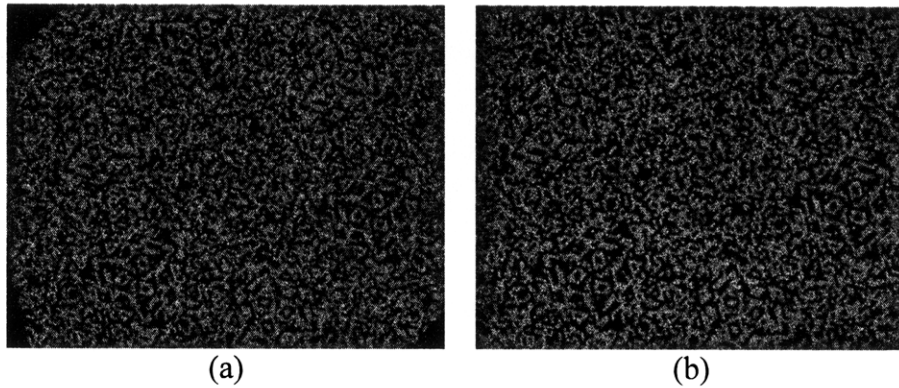


Figure 20. Magnified 50% fill factor mask shadow from the a) far sequence and b) the near sequence. Individual holes in each mask shadow are resolved and geometrical accuracy is preserved. The near sequence exhibited limitations on system resolution due to the mask-source proximity.

3.3 PHASE III Area Source Tests.

3.3.1 50% fill factor mask. Reconstructed images of the area source target are shown in Figure 21.

Image sizes are 128 x 128 pixels with 1536 mm x 1536 mm area. The raw detector output had dark edges around the border where the mask shadow ended. Initial reconstruction attempts had noticeable parallax, as shown by the two sides of the target in Figure 21a not being parallel. Smoothing the results, shown in Figure 21b, removed some artifacts and slightly improved contrast. The animated 15-image sequence exhibited apparent drift to the right and down with decreasing z -values.

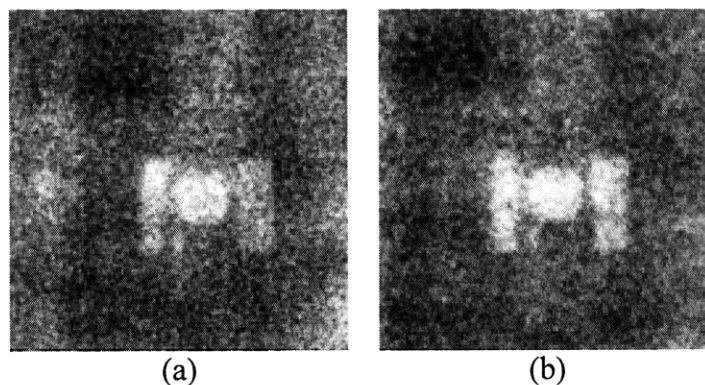


Figure 21. Single frame reconstruction of area source target imaged with the 50% fill mask. The a) initial reconstructed image contrast was improved slightly by smoothing, as shown in b). The contrast-to-noise ratio is not desirable.

Nearer frames were noticeably brighter. The most noticeable difference was a small jump between 5055 mm & 4991 mm.²³ The estimated lateral motion of the tug is shown in Figure 22.

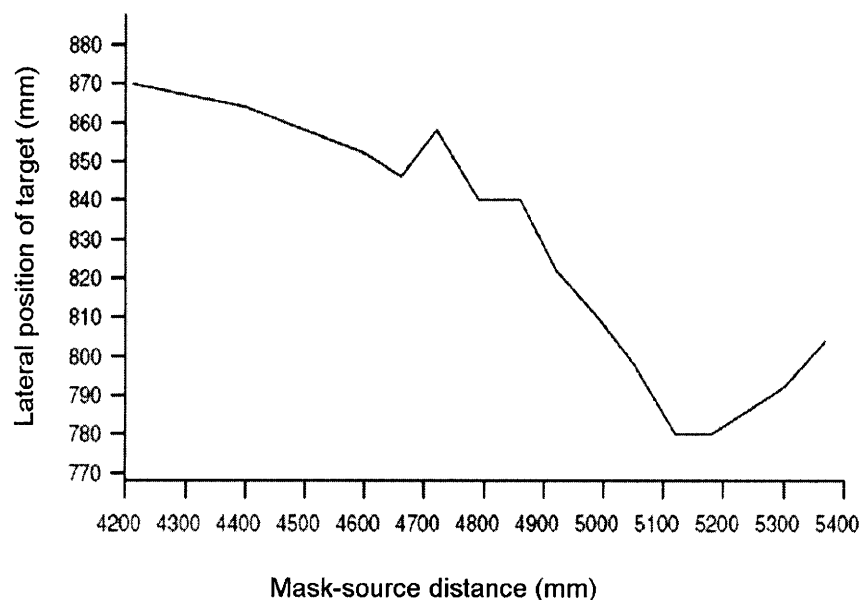


Figure 22. Estimated lateral motion of the tug shown as lateral position of the target center (mm) versus distance from camera (mm).

The "peak to peak" motion in the cumulative dynamic reconstructions is almost 100 mm. Vertical motion towards the camera was barely noticeable. Cumulative dynamic reconstruction sequences become less noisy for the first 6 frames, but then get smeared horizontally after the unexplained change in alignment.

3.3.2 25% fill factor mask. Reconstructed images of the area source target are shown in Figure 23.

Image sizes are 128 x 128 covering a 1536 x 1536 mm FOV. There was an expected three-fold improvement in CNR, from 1% to 3%. The wide (20% open) energy window images had higher contrast than the narrow (6% open) energy window images. The shadow of the edge of the mask is apparent in the edges of the detector output. If the edges were not discarded, there were visible vertical and horizontal line artifacts as shown in Figure 24.

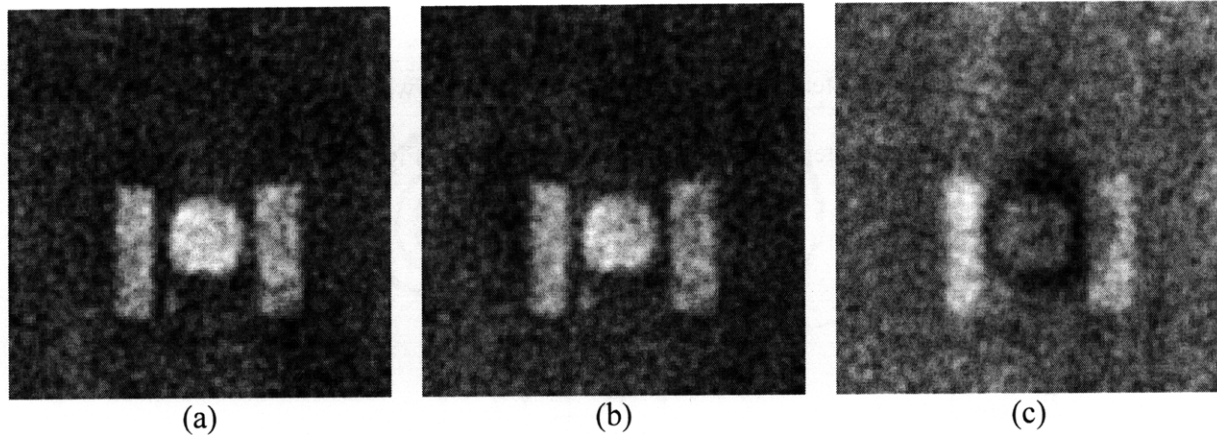


Figure 23. Reconstructed area source images with 25% fill mask taken with a) 20% open and b) 6% open energy windows. Images acquired near the limit of the 6% energy windows shown in c) experienced heavy artifacts. Contrast to noise ratio is very good overall.

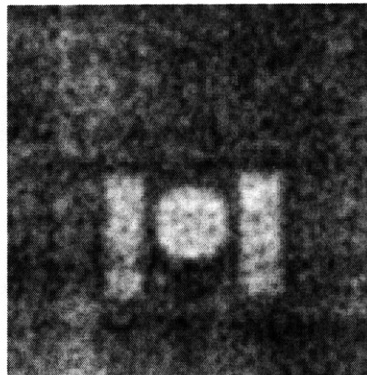


Figure 24. Reconstructed results without discarded edges of detector output. Horizontal and vertical line artifacts are clearly visible.

3.3.3 12.5% fill factor mask. The 10-frame sequence of area source reconstructions are shown in Figure 25. Contrast to noise degrades with descending mask-source distance. The acquisitions taken furthest from the mask surface had the greatest overall resolution. The acquisitions at $z = 615$ and 998 mm were resolved but heavily blurred. The target is almost indistinguishable above background at $z = 1499$ mm, but resolution improves as the target continues to move further away from the mask.

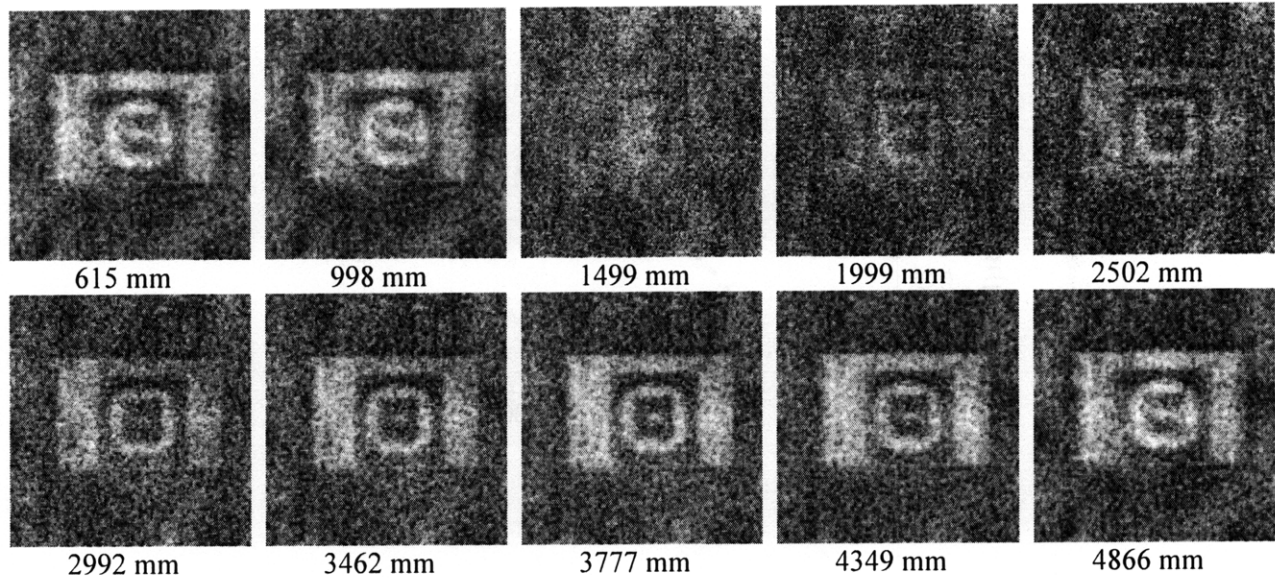


Figure 25. Reconstructed area-source target acquired with the 12.5% fill factor mask. Contrast to noise degrades as the target nears the mask. Off-axis illumination through the smaller holes of this mask prevented uniform illumination of the detector in near positions.

The amount of gamma ray throughput declined as the target neared the mask. An on-axis area source with geometry as shown in Figure 13 provides both on-axis illumination and off-axis illumination to each single mask element. The declining amount of gamma ray throughput using Equation 10, Section 1.22.2, is shown in Figure 26. The amount of gamma throughput zeroes at approximately $z = 1500$ mm, concurrent with the results in Figure 25.

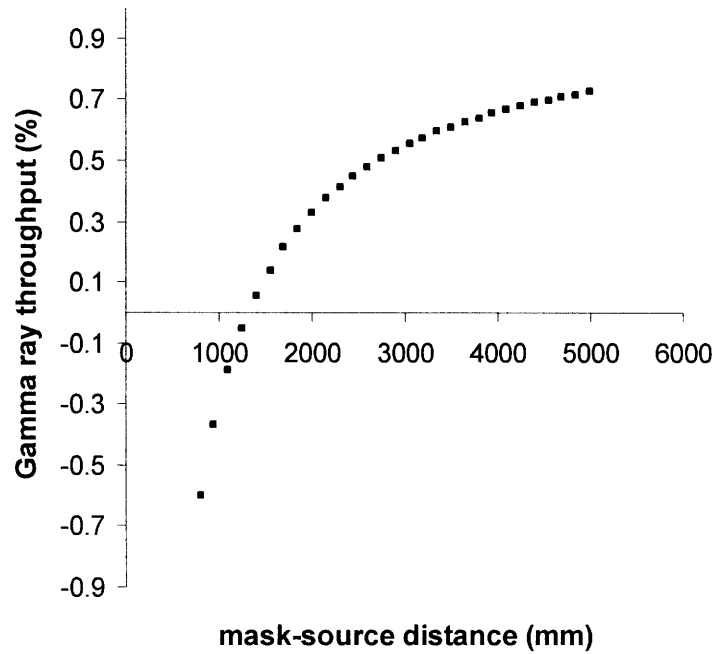


Figure 26. Percentage of gamma ray throughput as a function of mask-source distance (mm). As the target nears the mask, the amount of gamma rays that can actually pass through the holes in the mask decrease to zero at roughly 1500 mm. Crossover occurs below 1500 mm.

A logarithmic plot of count rate versus mask-source distance is shown in Figure 27. Self-collimation reduces the expected count rate beginning at $z = 2000$ mm and rapidly degrades with decreasing z values. These effects are in concert with the image results in Figure 25.

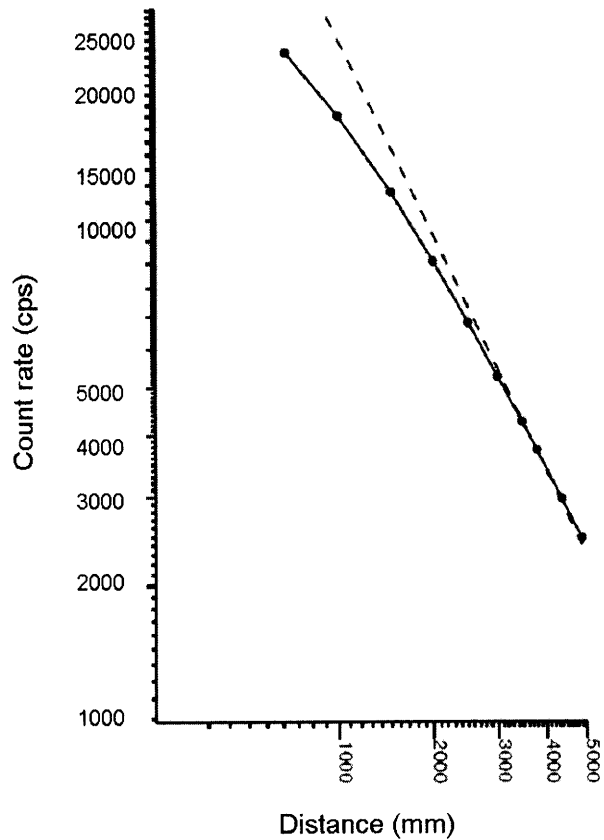


Figure 27. LOG of Count Rate versus LOG Distance .Data points are connected to aid the eye. The ideal slope is -2, shown as a dashed line. The decrease in count rate at closer distances is commensurate with loss due to self collimation.

3.4 PHASE IV. X-ray Source Tests

3.4.1 50% fill factor mask.

3.4.1.1 Initial tests. The water jug, reconstructed from one and five-million counts and counts is shown in Figure 28. The bright rectangular region in Figure 28a is 50 pixels across and 75 pixels tall. Pixels correspond to 5 mm x 5 mm at the object distance, thus the object is 250 mm wide and 375 mm tall. The target is not centered in the FOV. A bright “halo” surrounds the area to the upper left of the target in both images. The target plus the halos are approximately 100 pixels across. Contrast is exceedingly low.

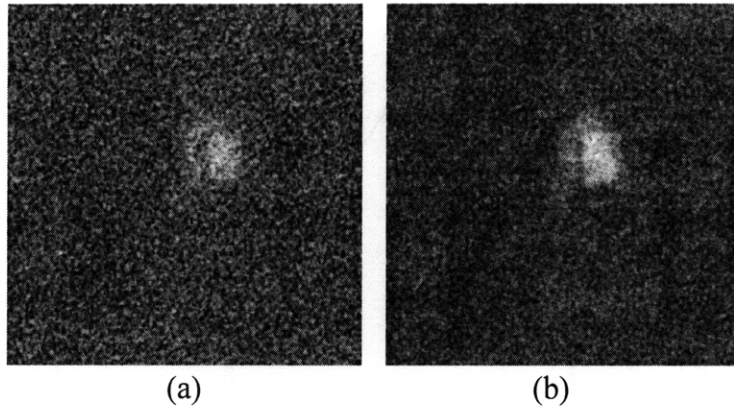


Figure 28. Two single-frame reconstructions of the water jug ($z = 5179$ mm) imaged with a) 1-million total counts with and 2560 mm x 2560 mm FOV and b) 5-million total counts with 1280 mm x 1280 mm FOV.

The misalignment of the system's optical axis resulted in systematic error. Only the upper left portion of the hexagonal basic pattern is noticeable in the raw detector output, shown in Figure 29a. The dark corners in the upper and lower left corners are the opaque areas of the mask plate. Reconstructed results, both including the dark corners and discarding the dark corners from the algorithm, are shown in Figure 29b and Figure 29c., respectively. Dark artifacts are visible when the dark corners are not removed. When the dark corners are removed, the target shifts location within the FOV and artifacts were reduced.

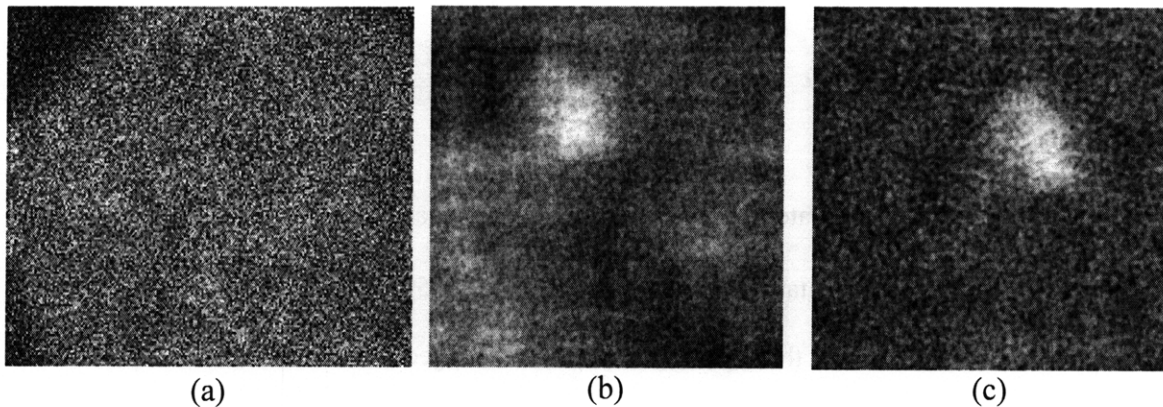


Figure 29. Systematic error due to misalignment of mask and detector centers. Dark corners in the a) raw detector output caused b) dark artifacts in the reconstructed image. Removing the corners moved the target center and reduced artifacts in c) the optimized reconstructed image.

The six-frame water jug sequence was acquired with the permanent mask shielding fixture in place. Near ($z = 4770$ mm) and far ($z = 5087$ mm) acquisitions of the reconstructed water jug sequence are shown in Figure 30. The entire sequence is shown in Appendix C. The reconstructed target area is approximately 250 mm wide and 350 mm tall. There is a dark horizontal area below and to the left of the bottle. There is a noticeable shadow/halo behind the water jug in the far image. This shadow was not noticeable in the rest of the sequence.

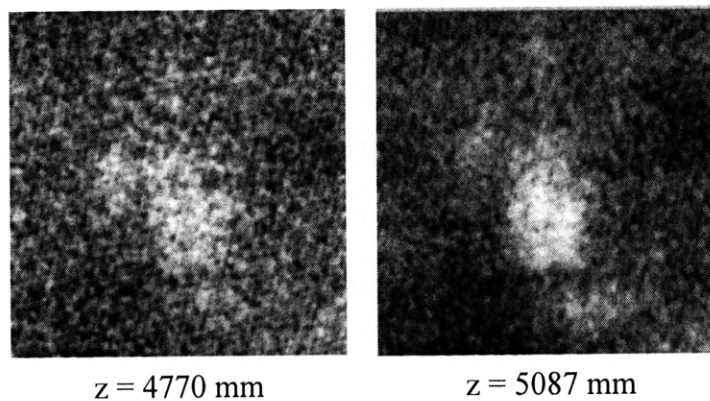


Figure 30. Water Jug Sequence reacquired with optical axis aligned. A near image ($z = 4770$ mm) is shown at left, far ($z = 5087$ mm) at right. Overall contrast improved with the optical axis aligned. Image matrix size is 256 x 256 covering a 1280 mm x 1280 mm FOV.

The DR algorithm successfully reconstructed the 14-frame ring sequence. The nearest and furthest reconstructions of the rings atop 2 poly sheets are shown in Figure 31. Though, the reconstructed images become cleaner as information accumulates, the central hole is not discernable. The two poly sheets behind the rings are not visible, but cause an overall increase in backscatter, visible as a lighter background in Figure 31. The last frame (4814 mm) of the sequence shows some distortion to the ring. The ring becomes smaller, more oval and displaces to the right because the target slowly leaves the X-ray cone beam.

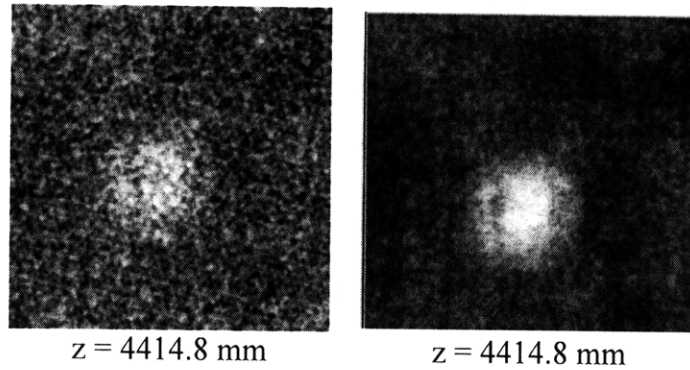


Figure 31. Near ($z = 4414.8$ mm) and far $z = (4414.8$ mm) reconstructions of the 14-frame polyethylene ring sequence. The rings were acquired atop two 600 mm x 600 mm polyethylene sheets to increase the backscatter signal. Images are 128 x 128 pixels covering a 1536 mm x 1536 mm FOV.

A high resolution sequence was acquired without the poly sheet backdrop. The first and last frames are shown in Figure 32 covering distances from 4815 mm to 4315 mm. The entire sequence is shown in Appendix C. The lead bricks used to support the rings are not visible. The nearest acquisition ($z = 4414.8$ mm) has a noisy background. The furthest frame ($z = 4814.8$ mm) has more contrast against a darker background.

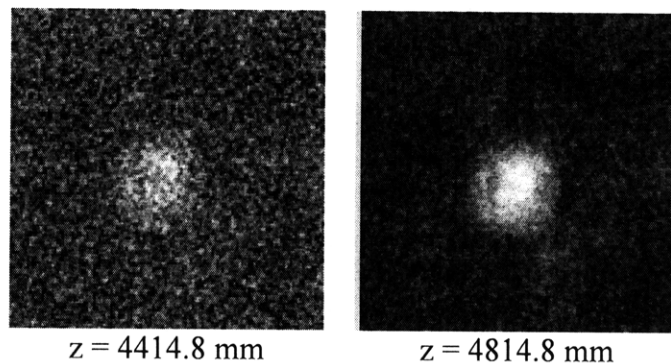


Figure 32. High resolution reconstructed ring sequence. The furthest and nearest frames are shown at left and right, respectively. The rings were acquired atop two lead bricks to reduce noise from backscatter. Images are 256 x 256 pixels covering a FOV of 1280 x 1280 mm.

3.4.1.2 Selection of optimum imaging protocols. The results of the camera imaging protocols tests are shown in Figure 33. The arrow is clearly distinguishable in the image, pointed at a 45° angle to the upper left quadrant. The sharpest reconstructed image was produced using the hepatobiliary

protocol, single isotope study, and 20% open energy windows. The results produced from using both narrow energy windows and the gamma camera's energy banding feature were not resolvable.

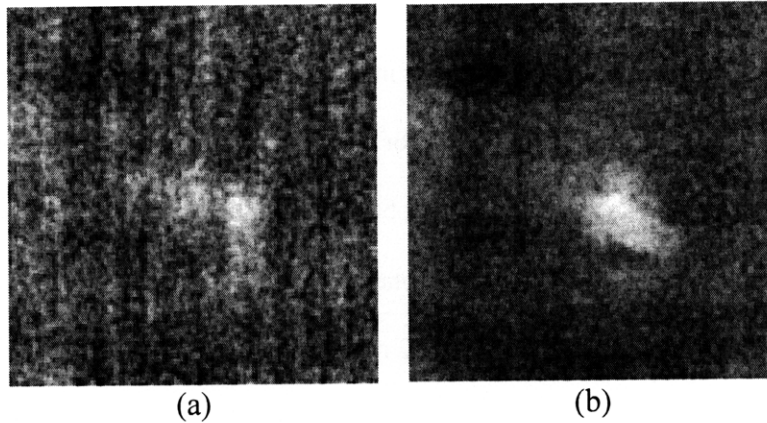


Figure 33. Reconstructed arrow ($z = 5208$ mm) after optimizing gamma camera imaging protocols. Energy windows are a) 6% open and b) 20% open. Image size is 128×128 pixels covering a 1536×1536 mm FOV.

3.4.1.3 Change of geometry. The water jug, imaged with the old and new source-detector geometry, is shown in Figure 34. The amount of scatter is reduced and overall contrast is improved between the old geometry in Figure 34a and the new geometry in

Figure 34b. New and old geometry reconstructions with the arrow are shown in Appendix C, and show similar results.

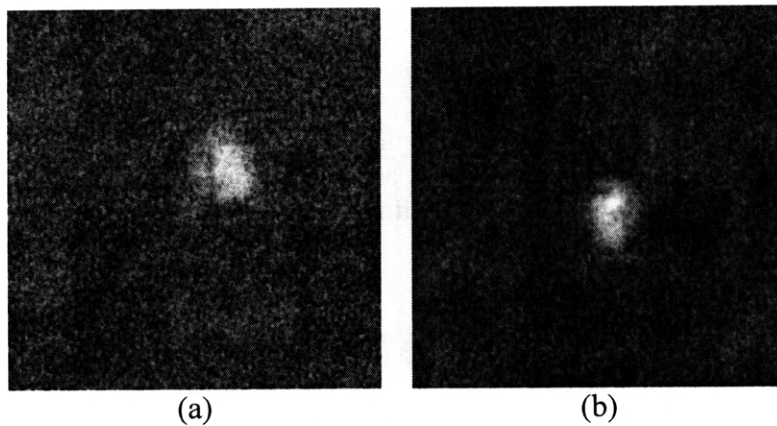


Figure 34. Reducing the source-target distance and increasing the mask-target distance improved contrast. The water jug ($z = 5172$ mm) was imaged with a) old geometry and b) new geometry and additional shielding around the X-ray tube. Images are 256×256 pixels covering a 2560×2560 mm FOV.

4.2.1.4 Mask and Anti-mask addition. After both the mask and anti-mask images were reconstructed, there were two associated images for each z-value. The mask and anti-mask reconstructions of the arrow ($z = 4470$ mm) are shown in Figure 35a and Figure 35b, respectively. The arrow is shown upright. These images were selected for coupling because they had the best contrast in the sequence. The full reconstructed arrow sequences obtained with both the mask and anti-mask are shown in Appendix C. The raw detector output was rotated 60 degrees to obtain the anti-mask results. The edges and corners were trimmed 150 pixels and 12 rows, respectively. The outline of the arrow, though blurred, is noticeable in both images. The mask and anti-mask reconstructions were added pixel by pixel and then renormalized using the Image Calculator tool in ImageJ™. The resultant image was averaged using ImageJ's internal division tool. The results using this method are shown in Figure 35c.

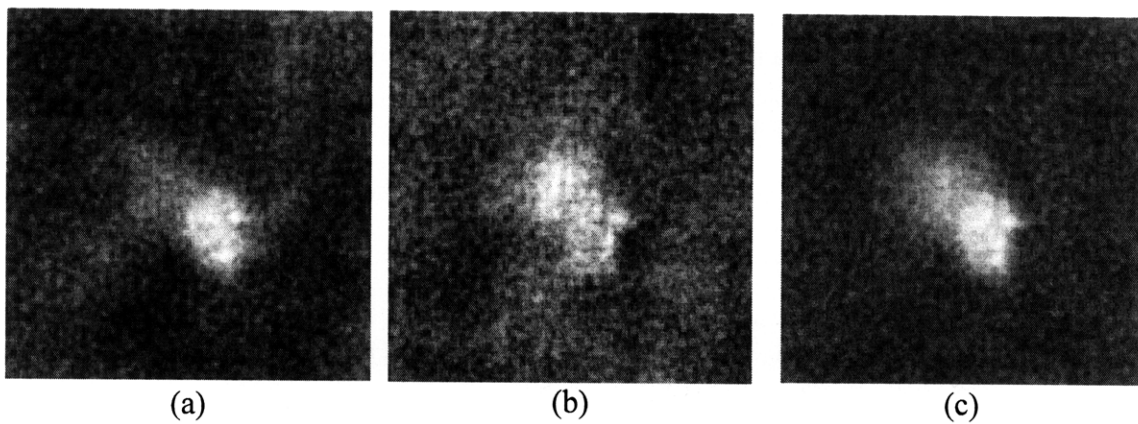
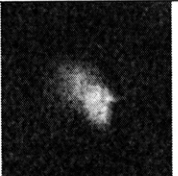
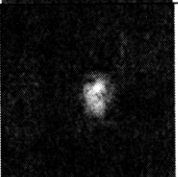
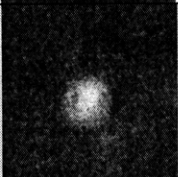
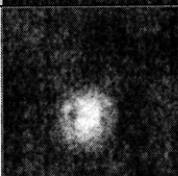


Figure 35. The reconstructed, upright arrow ($z = 4470$ mm) with Mask-Anti-mask image addition improved contrast and smoothed artifacts. The a) mask and b) anti-mask images were averaged to produce the c) final smoother image against a more uniform background. Image FOV is 1280 x 1280 mm FOV.

3.4.1.5. Contrast-to-Noise Ratios. The rings on polyethylene sheets (Figure 31b), rings on lead bricks (Figure 32b), water jug (Figure 34b), and mask/anti-mask (Figure 35c) were analyzed for CNR because they had the best overall contrast based on a qualitative, visual assessment. The method

used to empirically calculate CNR is explained in Appendix C. Results are listed in Table 6. All subsequent images were analyzed in this same manner.

Table 6. Contrast-to-noise ratio results (in descending order) for 50% fill factor reconstructions. The water jug had highest overall contrast-to-noise ratio. Signal-to-noise ratios are listed for comparison. All images had 10^6 total counts per image.

Target	Image	CNR	SNR	Mean Target Intensity (0-255)	Mean Background Intensity (0-255)
mask/anti-mask		11.0 ± 0.4	2.7 ± 0.6	191.4	69.7
water jug		9.0 ± 0.8	3.6 ± 0.8	191.5	52.9
Ring on lead bricks		8.6 ± 0.8	3.4 ± 0.9	209.0	62.0
Ring on polyethylene sheets		6.2 ± 0.7	2.9 ± 1.2	216.6	72.6

3.4.2 25% fill factor mask.

3.4.2.1 Initial tests. A single frame of the reconstructed arrow sequence is shown in Figure 36. Reconstructions throughout the sequence showed similar contrast, much improved over the 50% fill mask (Figure 33b). The arrow is fully delineated against the background. The halo from backscatter on the steel backdrop is still visible to the left and above the target. A dark, circular shadow exists behind the target and halo.



$z = 4701 \text{ mm}$

Figure 36. Single frame reconstruction of the arrow ($z = 470.1$) with 25% fill mask. The backscatter halo behind target is due to source geometry. Image size is 128×128 pixels covering a 1280×1280 mm FOV.

The reconstructed water jug imaged on lead bricks is shown below. The jug handles are clearly visible in both images in Figure 37. In the reconstruction of the jug on lead, a darker shadow is cast behind and to the upper left of the target. However, in Figure 37a there is not much contrast between the target and background notably at the top of the target. The brightest portion of the target atop the bricks is in the lower right hand corner. There is a small, dark shadow behind and to the upper left of the jug.

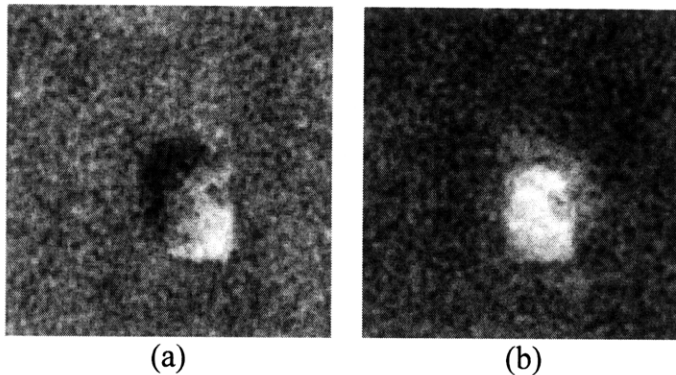


Figure 37. Reconstructed Water jug imaged on a) lead bricks ($z = 4514 \text{ mm}$) and b) three horizontal polyethylene sheets ($z = 4617 \text{ mm}$). Photons backscattering off the polyethylene sheets increased the background noise.

In contrast, the reconstructed jug on polyethylene sheets is brighter and more uniformly illuminated against a darker background. There is a noticeable halo of backscatter from the steel behind the target. This halo is centered about the target. The CNR in Figure 32 and Figure 33 is improved 3

times over the 50% fill mask.

3.4.2.2 Effects of altering the energy spectrum.

Decreased filtration. The near and far frame of the reconstructed ring sequence, taken after the X-ray tube's filtration was decreased, are shown in Figure 34. The entire sequence is shown in Appendix C. The rings partially obscure the beam's illumination on the wall. When observing the trimmed images of the raw detector output, the corners and edges of the images were noticeably darker. The near images are noisier than those taken furthest from the mask.

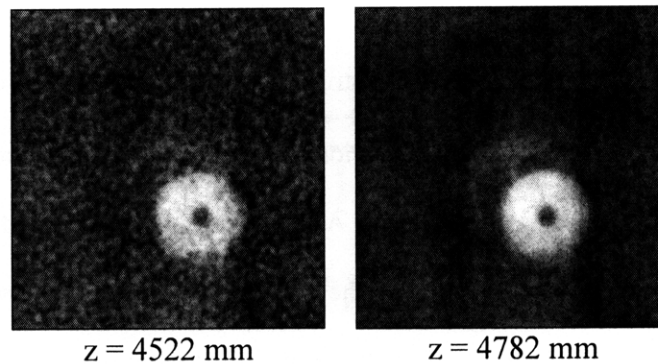


Figure 38. Two-frames of the reconstructed ring sequence with 25% fill mask and decreased X-ray tube filtration. 100K total counts were acquired per image. Animation was near ($z = 4522$ mm) to far ($z = 4782$ mm).

Widened Cone Beam. The reconstructed arrow, shown after the cone beam was widened, is shown in Figure 39. Three frames of the sequence are shown, from near to far. The entire sequence is shown in Appendix C. The corners (with command line entry `-c=175`) and edges (command line entry `-e=20`) of the raw detector output were trimmed to remove the dark areas. Both the wide and narrow cone beam reconstructions had the dark corners of the detector output removed. Even after trimming, there are dark blobby artifacts surrounding the arrow in all the images. The contrast is noticeably worse than when the cone beam was narrower, as shown in Figure 32. Still, the reconstructed arrows in Figure 35 are not uniformly illuminated. The arrow is brightest at the top right of the arrowhead and on the bottom.

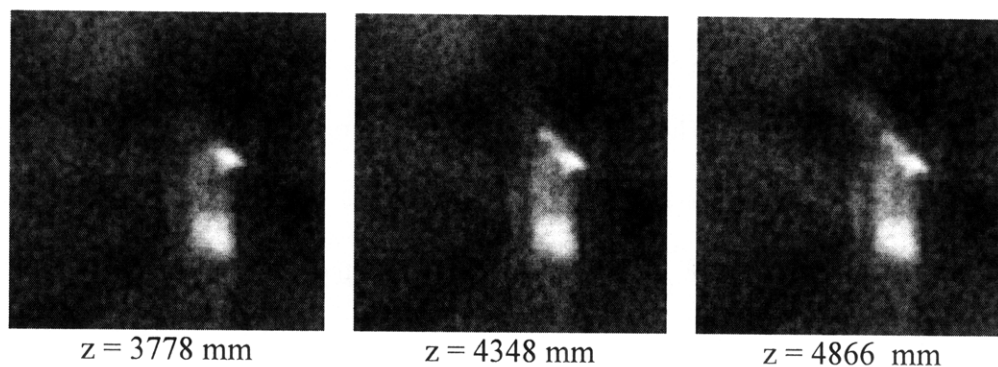


Figure 39. Reconstructed arrow sequence after widening of cone beam. Horizontally streaking artifacts remained even after trimming detector output. Image size is 128 x 128 pixels covering a 1280 x 1280 mm FOV.

3.4.2.3 Multiple Object Scene. The reconstructed multiple object scene is shown in Figure 40. The images were acquired with 8.0 mA and 5 million total counts in order to obtain enough information about the target in the least possible time. All three objects are clearly delineated as well as the stack of polyethylene sheets they are resting on. The cylinder shows up only partially illuminated, with a bright blob about as tall as the bright glove in the center. The palm of the glove is brightly illuminated, but the fingers are only faintly noticeable. There is a dark area below the glove because the glove was resting on a cylindrical, lead support. The bottle's wide base and narrow top are delineable. The space between the objects is not as dark as the background noise. The halo from backscatter on the steel is apparent, but there is no noticeable shadow from any of the objects. The illumination of the stack of poly sheets is the most uniform of all the objects.

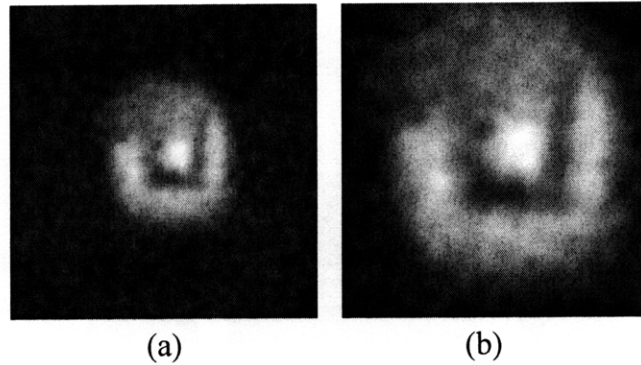


Figure 40. Multiple Object scene acquired with the 25% fill factor mask. From left to right, a cylinder, glove, and soda bottle are blurry because of a weak backscatter signal. Image size is a) 960 mm x 960mm and b) 512mm x 512mm.

3.4.2.4. Resolution Tests. The results of the resolution tests imaging the arrow with 1024 x 1024, 512 x 512, and 256 x 256 matrix sizes are shown in Figure 41. You can see some deterioration going from 1024 x 1024 to 512 x 512 and more going from 512 x 512 to 256 x 256. The loss in quality is not as bad as we had in early versions of the program. In the algorithm, the corners, top and bottom of each detector frame were trimmed to optimize the images. “-c” cut out corners of detector frame and “-e” trimmed the rows from top and bottom (e.g. -e=10). The bottom three frames of Figure 17 applied trimming to discard a portion of the detector output. The 1024 x 1024 trimmed image had 150 pixels trimmed from the corners and 12 rows of pixels trimmed from top and bottom. The 512 x 512 image had 75 pixels removed from the corners and 6 rows removed from top and bottom. Last, the 256 x 256 image had 37 pixels removed from the corners and 3 rows removed from top and bottom.

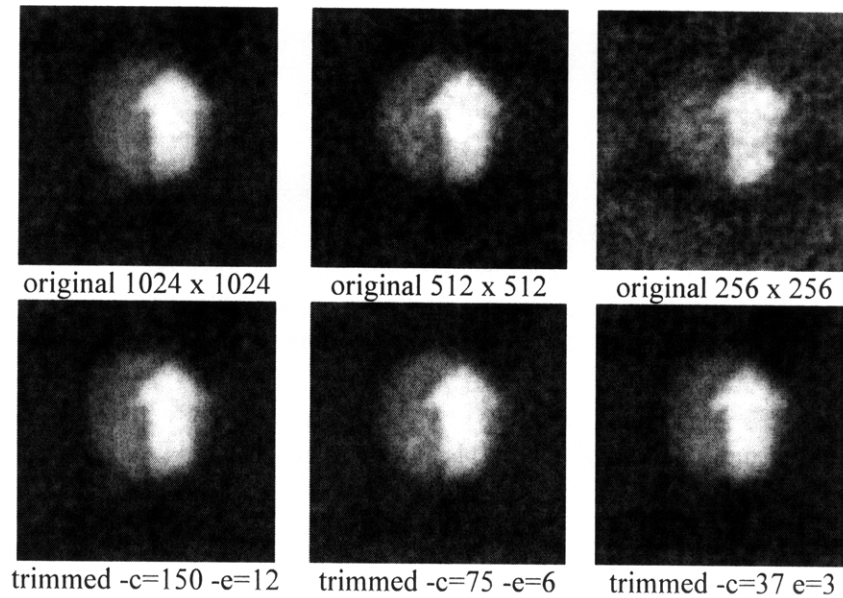


Figure 41. Reconstructed optimized arrow at 1024 x 1024, 512 x 512, and 256 x 256 with and without trimming height and corners. With trimming both the high and low resolution images are near equal and of acceptable quality.

With trimming, there is little deterioration from the 1024 x 1024 to 256 x 256 matrix size. These results could also be obtained by first using a 1024 x 1024 matrix size and then block average the image to reduce it to the equivalent 512 x 512 or 256 x 256 images.

The dynamic reconstruction algorithm was continually modified with updates designed to optimize the data handling or speed. Earlier versions of the algorithm produced cumbersome streaking artifacts with detector outputs below 512 x 512. A full description of these updates is covered in Appendix C. However, trimming the detector output and smoothing the results enabled reconstruction of images in 128 x 128 and 64 x 64 matrix size as shown in Figure 18. The 128 x 128 image had 18 rows trimmed from the corners and two rows trimmed from the height. The 64 x 64 image had nine rows and two rows trimmed from the corners and height, respectively. A quilt-like pattern of artifacts is noticeable in the 128 x 128 version but overwhelm the 64 x 64 reconstruction.

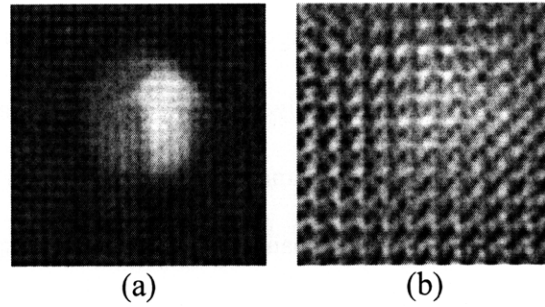
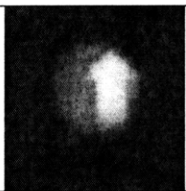
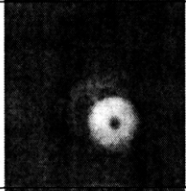



Figure 42. Reconstructed arrow using a) 128 x128 matrix size and b) 64 x 64 matrix size. Image quality is unacceptable.

3.4.2.5 Contrast-to-Noise Ratios for 25% fill mask. The water jug (Figure 37b), rings with less filtration (Figure 34b), trimmed 1024 x 1024 arrow with new geometry (Figure 37) were analyzed for CNR because they had the best overall contrast based on a qualitative, visual assessment. The method used to empirically calculate CNR is explained in Appendix C. Results are listed in Table 7. All subsequent images were analyzed in this same manner.

Table 7. Contrast-to-noise ratio results (in descending order) for 25% fill factor reconstructions. The arrow had highest overall contrast-to-noise ratio. Reducing the filtration and changing the geometry had the highest improvement on contrast. Signal-to-noise ratios are listed for comparison.

Target	Image	CNR	SNR	Mean Target Intensity (0-255)	Mean Background Intensity (0-255)
arrow, new geometry		19.6 ± 0.5	4.8 ± 0.8	238.6	49.2
rings, less filtration		16.6 ± 0.8	5.7 ± 1.3	233.4	41.0
water jug		8.1 ± 0.4	3.4 ± 0.9	213.6	62.4

3.4.2.6 Resolution tests with Optimized 25% Images (Rings). Resolution was calculated with the optimized reconstructed images. The reconstructed polyethylene ring, in comparison to an actual image, is shown in Figure 39. The actual ring has an outer diameter of 350 mm and an inner diameter of 80 mm. The reconstructed image's outer and inner diameter spans 72 and 16 pixels, respectively. At 5 mm per pixel, these distances equate to 350 mm and 80 mm.

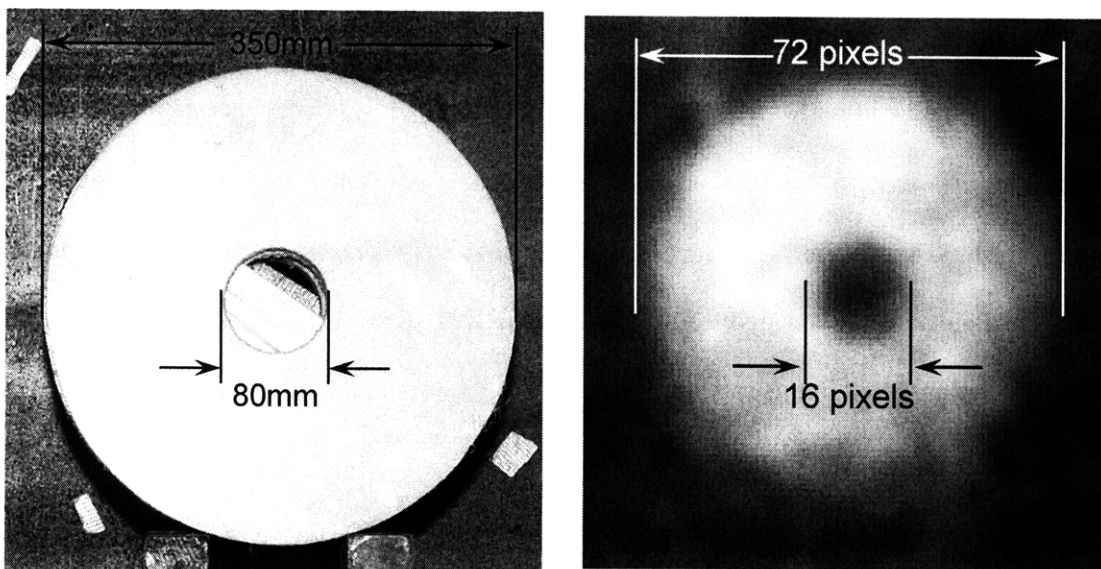


Figure 43. Resolution calculation for 25% fill factor mask. The ring diameter and cutout diameter were measured at left and compared to the reconstructed image at right. 25mm resolution at the target was achieved.

3.4.3. 12.5% fill factor mask.

3.4.3.1. Initial Calibration tests. The results of the initial calibration tests with the 1.67 mCi Co-57 point source are shown in Figure 44. The image FOV is 1536 x 1536 mm. The FWHM is 14 pixels or 28 mm. Equation 12, with $z = 5100$ mm and $f = 686$ mm, yields a FWHM on the gamma camera surface of 3.7 mm.

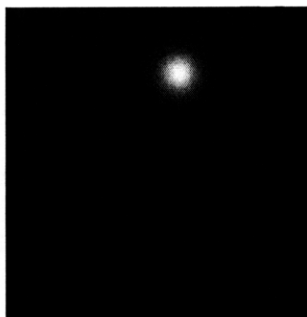


Figure 44. Initial point-source calibration image with 12.5% fill factor mask. The estimated FWHM (3.7 mm) was narrower than the 50% fill mask (4.5 mm FWHM) and the 25% fill masks (4 mm FWHM). Image is 256 x 256 pixels covering a 1536 x 1536 mm FOV.

3.4.3.2 Arrow comparison. The arrow, reconstructed with the 12.5% fill factor mask is shown in Figure 45. Only one image was acquired at 4781 mm with the wide beam and lower filtration. The total number of counts remained at 10^6 , as in previous images. The top of the arrowhead is not resolved, despite the arrow being fully illuminated against the wall. At left, the image was reconstructed with 128 x 128 matrix size and a 960 x 960 mm FOV. At right, the image was reconstructed using 200 x 200 matrix size covering a 1280 x 1280 FOV for direct comparison to previous reconstructions using the higher fill factor masks. The 960 x 960 image is shown enlarged for direct comparison to the 200 x 200 matrix reconstruction.

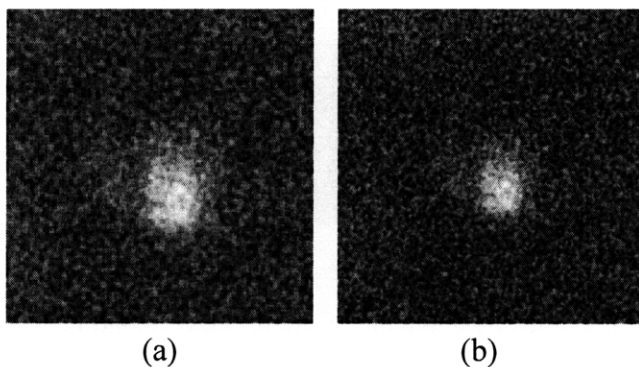


Figure 45. Reconstructed arrow ($z = 4781$ mm) with 12.5% mask with a) 128 x 128 matrix size covering 960 x 960 mm FOV and b) 200 x 200 matrix size covering 1280 x 1280 FOV. The 128 x 128 image is enlarged for direct comparison.

The arrow reconstruction in Figure 45a was the only 12.5% reconstruction analyzed for CNR. The mean intensity (212.9), mean background (79.9), and standard deviation (19.4), produced a CNR of 6.9 ± 0.9 . The values for both the 128 x 128 and 200 x 200 matrix sizes were comparable within half a standard deviation, so only the results of the first image are listed. The SNR, computed for comparison, is 2.7.

3.4.3.3 Multiple object scene. The reconstructed multiple object scene is shown in Figure 42. From left to right, the cylinder, glove, and soda bottle are visible but heavily blurred. The shadow of the cone beam is visible to the left and above the target group. The background, though noisy, is uniform and not dominated by artifacts. The bottom portion of Figure 42's reconstructed images appears brighter because the X-rays are backscattering off the stack of poly sheets used as a support. The bright, circular area to the upper left of the target is backscatter off the steel covered concrete wall. The glove appears the brightest, most likely because it contains the most backscattered material by volume (polyethylene beads and water). The bottle on right appears taller than the cylinder at left because the cylinder had leaked water during acquisition. These 12.5% reconstructions, though noisier, have finer resolution over the 25% reconstructions shown in Figure 40.

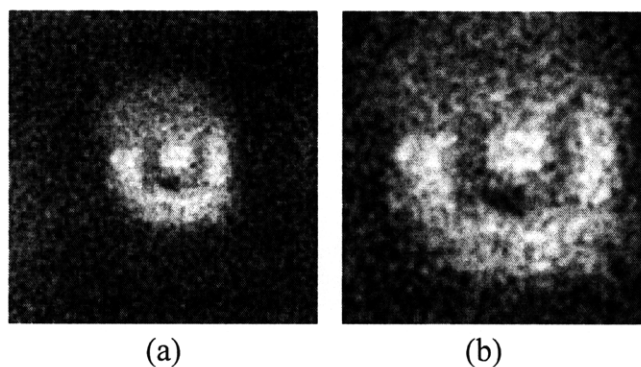


Figure 46. Reconstructed multiple object scene with 12.5% fill mask. Contrast is not improved over the 25% fill reconstructions. Image size is a) 960 x 960 mm and b) 512 x 512 mm.

After smoothing, the reconstructions had better overall contrast. The smoothed results are shown in Figure 47. The gamma resolution limitation has more impact on the images from the 12.5% mask because the hole-spacing is so much smaller (1.625 mm versus 3.9mm or 3.5mm). Accordingly, increased

smoothing was attempted to compensate as a technique to improve contrast and overall image quality.

The smoothing was conducted on the internal mask array during the reconstruction process.

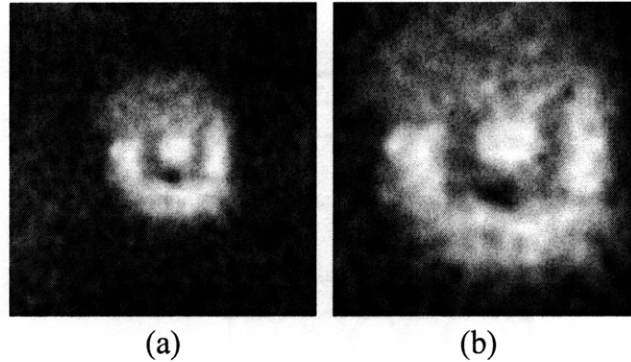


Figure 47. Smoothed reconstructions with 12.5% mask. The a) 960 x 960 mm image was smoothed with 15 passes and b) 512 x 512 mm image had 30 passes. Contrast is improved.

3.4.3.4 Self-Collimation Effects. The results of the area source self-collimation investigation are presented in Section 3.3.3 and confirmed the presence of self-collimation. The reconstructions, shown in Figure 44, illustrate the point source in the center of the FOV and echoes in the lower left and upper right corner. Qualitatively, these bright echoes noticeably increase in intensity from $z = 2992$ mm to the closest acquisition at $z = 615$ mm. Additionally, the overall background increases in the last six reconstructions. This increase is noticeable as the light, grainy background texture that appears lightest in the near reconstruction ($z = 615$ mm) and gradually fades to nearly a black background in the far reconstruction ($z = 4866$ mm).

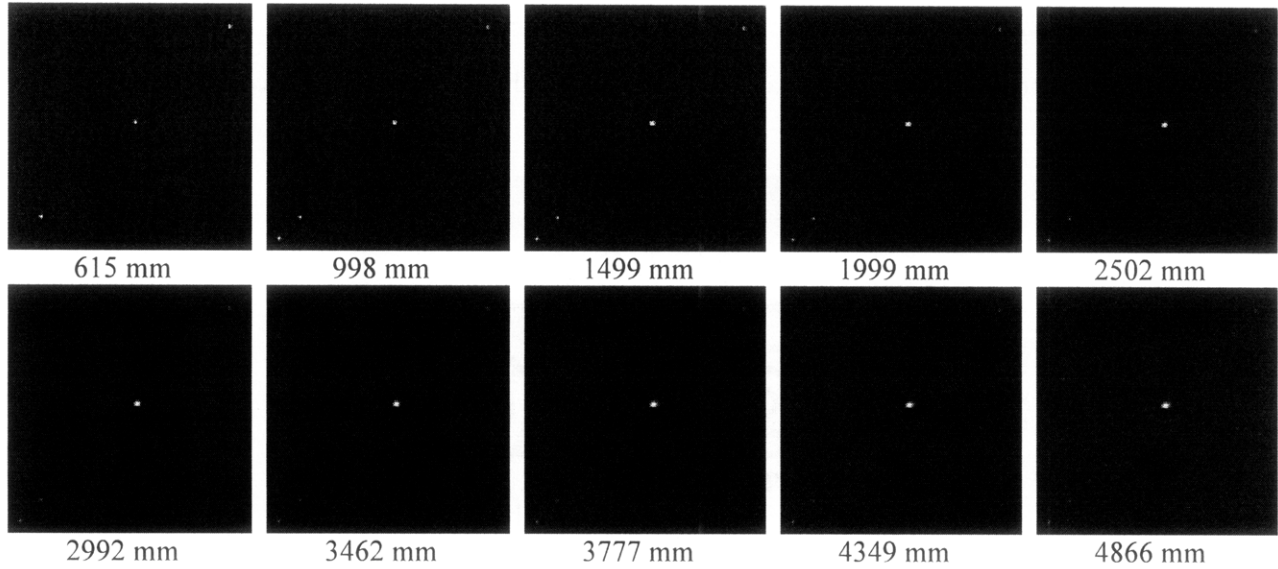


Figure 48. Point Source Series showing presence of self-collimation effects. Contrast to noise degrades as the target nears the mask. Off-axis illumination through the smaller holes of this mask prevented uniform illumination of the detector in near positions

The background noise in each image was quantified using ImageJ's histogram feature. The results are shown in Figure 45. The maximum brightness of the artifacts (not including the target) is shown as a dashed line that increases in value as the point source nears the mask. The echoes are brightest in the six nearest acquisitions, which begin increasing at $z = 2992$ mm. The intensity of the echoes remains bright through to the nearest acquisition at $z = 615$ mm. The mean background is shown as a solid line and increases as the source nears the mask. Standard deviation is shown as a dotted line and is higher near the mask, peaking in the middle acquisitions.

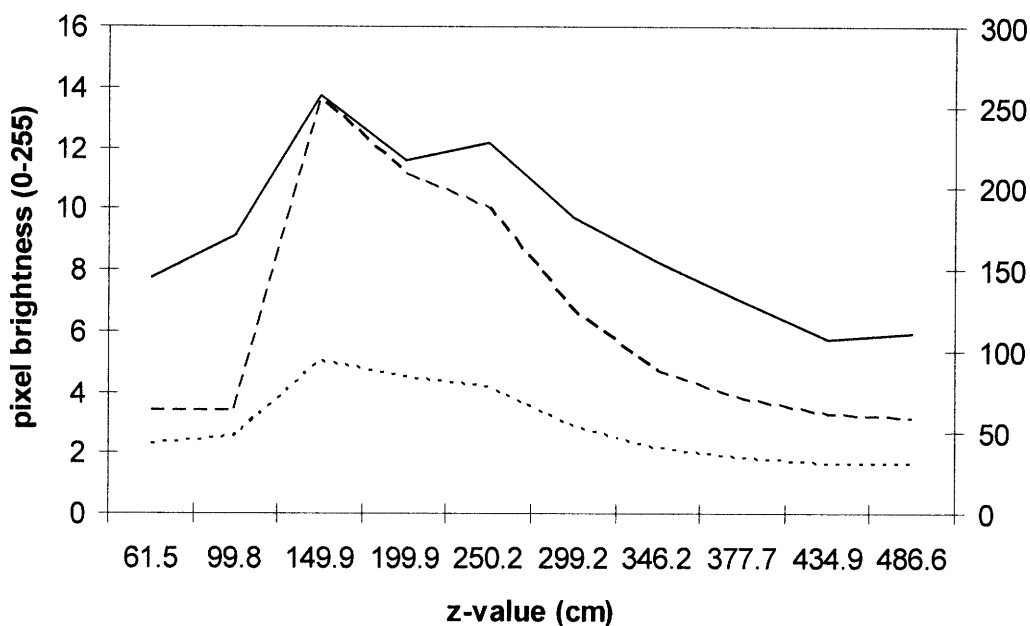


Figure 49. Self-collimation effects increased background noise at closer distances. The background (solid line), standard deviation (dotted line), and maximum background value (dashed line) all increased as the source neared the mask.

4. DISCUSSION

4.1 PHASE I.

Resolution and MTF. The Anger camera’s resolution was at least 3 mm as evidenced by the ability to resolve each quadrant in the bar phantom. The 2.5 mm and 2.0 mm quadrants were resolved but were of poor quality due to low contrast. Future backscatter experiments would only add noise on top of images with comparably poor quality, so those quadrants were not further analyzed. The calculated bar widths were 99% accurate to the actual widths in each quadrant, indicating excellent geometric accuracy. However, the poor contrast must be considered despite being able to see each pattern.

The waviness of the lines at the image’s edges in Figure 15 is caused by events detected at the limits of the detector’s “active area” getting misplaced due to the limitations of the Anger camera’s electronics. As a result of these non-uniformities, edges of the detector output were excluded from the reconstruction algorithm.

Maximum spatial frequency content in a coded aperture mask is achieved when the design includes a similar alternating pattern between opaque and transparent areas similar to the bar phantom. Though the 6.00 and 7.08 mm wavelength quadrants had acceptable SNR (above 2.0), resolution in a coded aperture mask is optimized by using the smallest diameter hole. So, the wavelength of 6.00 mm was selected as the threshold. A wavelength of 6.00 mm (3.0 mm wide bars) implies the final mask design should have a similar wavelength for comparable results using this camera. Thus, 3.0 mm (and higher) hole spacing were considered for the first mask. Larger hole spacing was not considered because they would increase the system PSF, further degrading resolution.

It was easy to obtain the MTF by imaging the preexisting mask and taking the FT because it possessed the ideal two-valued correlation property. More specifically, the correlation for zero-shift is one value while the correlation for other shifts is half that value. That is, the correlation is a pulse on top of a uniform background located at the origin of the FOV. Taking the Fourier Transform of the auto-correlation function (i.e. obtaining the power spectrum) gives the transform of the pulse (uniform pedestal) plus the transform of the uniform pedestal (a pulse). If the zero frequency (DC component) is ignored, a signal that is flat in the frequency domain is given as an input to the system. Accordingly, if the FT of the mask shadow image is measured without the DC component, the result is the system MTF.

Hole spacing of 3.5 mm was verified as the optimal spacing for the new 50% fill mask design because the gamma camera's MTF exhibited good frequency response with the same "simulated" hole spacing. There was relatively good response from the origin to approximately one cycle per 7.0 mm. This was half the frequency of the cell spacing, indicating that spacing of about 3.5 mm would be the optimal spacing for the final mask design.²⁴ Furthermore, the MTF in Figure 17b was also rotationally symmetric, indicating our system PSF did not have any directional biases.

Qualitatively, the gamma camera was able to successfully resolve the holes in the magnified mask shadow. The mask shadow in Figure 17a is magnified such that the hole spacing is 3.5 mm. Because these holes were successfully resolved, it implies that it is possible to successfully resolve the holes in a less magnified, new mask shadow with larger array size.

4.2 PHASE II.

Proof of Principle. Of primary importance is that the dynamic reconstruction algorithm successfully reconstructed the point source. Successive acquisitions in the sequence simulated smooth translation along the track with a z-separation distance not to exceed 1% of the total track length. Though future acquisitions did not require such a small separation distance, it was determined that this Δx between static acquisitions would best simulate relative motion.

Resolution improved as the target moved closer to the mask, as was expected. The resolution improved until the target passed the z-value corresponding to the maximum magnification of the mask shadow on the detector. The elongation of the reconstructed point source in Figure 19 was due to later data being taken closer to the mask. Because the source was closer, it had a smaller PSF when back projected into the image. As a result, the middle portion of the “blob” was narrower. Further, the noticeable artifacting in the background was due to how much of the detector frame was used in the back projection. The entire detector frame was used in this particular back-projection and the mask is represented as doubly periodic with no boundary.²⁵

The echoes in Figure 19 appear because the image covers a large 1600 mm x 1600 mm FOV. In the near sequence reconstructions, magnification was maximized and multiple points on the target produced the same mask shadow on the detector. As a result, those same points could not be distinguished in the back-projection. Though the near sequence imaging parameters (over magnification and FOVs greater than 1500 mm) would not be used in future acquisitions, it did illustrate the limitations of our imaging system.

The reconstructed images showed high sensitivity to lateral drift of the source and errors in distance. The source may have experienced a sideways jump due to changes in the geometry. This drift was most likely due to precision errors in z measurements as well as the track not being exactly perpendicular to the mask surface. The target was emplaced atop a small table and physically moved for

each acquisition. The target may have only been misaligned by a few degrees, however the drift became more pronounced as the source neared the mask and became more off-axis. To remove this systematic error, all subsequent distances were measured with a laser range finder. Additionally, the track was retrofitted with a steel “guide” to keep the path of the tug at a perfect 180 degrees from the mask. All movements of the source were done through mechanical movement of the tug and no longer by hand.

The reconstruction algorithm was also sensitive to errors in the assumed angle of the mask. The diameter of the basic repeating pattern for the 50% fill ($p=5491$) mask is 58. This implies that the mask rotation angle must be known to within $1 \text{ radian} / 58$ (about 1 degree). Similarly, distance should be known to within $650 \text{ mm} / 58$ (about 11 mm). These limits agree with the results, which had to be optimized to account for minor errors in distance and rotation.

Future testing. The dynamic imaging mode was not used in later acquisitions because the image resolution was limited to 128×128 . 1024×1024 images were not possible in dynamic mode due to DSP memory limitations of the Anger Camera. Though dynamic mode made it physically easier to acquire each image without constant intervention of the user between acquisitions, future acquisitions were all static because that mode enabled 1024×1024 imaging. Further, future tests would be conducted with less counts to test the reconstruction algorithm’s robustness. Information would be accumulated over multiple frames that would produce images with reasonable signal-to-noise ratios over time. These tests with a point source demonstrated the reconstruction algorithm worked but with pristine results not commensurate with extended, area scenes and excessive scatter.

4.3 PHASE III Area Source Tests. Overall, the area source targets being successfully reconstructed demonstrated the technique worked with a mono-energetic area source. There was a marked decrease in contrast from the point source reconstructions. This decrease was expected because the contrast is inversely proportional to the number of sources. An area source can be considered as a collection of N point sources. For each source location, the signal (peak minus pedestal) remains

constant with additional adjacent sources, while the background (pedestal) is linearly proportional with the number of sources N (Appendix A).

4.3.1 50% fill factor mask. The initial parallax noticeable in Figure 21 was most likely due to the cutout not being flush with the source, but rather leaning against it. The apparent drift of the system was due to misalignment of the tug track with the system axis. The image scaling was commensurate with the measurements, which verified that imaging with the laser range finder was successful.

Figure 22 not being a straight line implies there was track irregularity near 5000 mm. Possible causes include angular deviation of the floor, the tug may have rolled over some small foreign object, and the target may have leaned or moved during translation. As a result, the floor was re-swept, the tug wheels tightened and all future targets were leveled and secured with vice grips. However, algorithm alterations and post-processing were able to smooth the results, as shown in Figure 21b. Of note is that the algorithm could smooth minor instability or jiggling of the acquisition system during translation.

4.3.2 25% fill factor mask. Images taken with the narrow energy windows had a dark ring artifact around the opening in the lead cutout, as shown in Figure 23c. The camera could only acquire a small percentage of the exigent gammas with the windows set at 118 to 124 keV. Accordingly, nearly all of the narrow band reconstructions had these artifacts unless the image was taken at the very center of the energy window, as shown in Figure 23b. This “dark ring” artifact could also have been due to lessened sensitivity from bright spots robbing dim spots in a wide scene such as this. The suppression of brightness affected the hexagonal center cutout, the background near it, and a portion of the right "wing" of the area source. The area with lessened sensitivity has a diameter of about 420 mm at the target, approximately 42 pixels across (image covering 1280 mm x 1280 mm). The target is around 4200 mm from the camera. However, this effect was not apparent in the wide-band reconstructions in Figure 23a.

Another possibility for the dark ring in Figure 23c was because the target was not perfectly perpendicular to the mask. This small-angle tilt of the area source may have caused incident rays to be deflected from the mask. If the estimated energy of the incident rays was different than truly

perpendicular rays, then the energies could shift out of the energy window. From the imaging geometry, the difference in direction is around $\arctan(420 / 4600)$ or 8 degrees. The gamma camera is most likely not that sensitive to changes in incident gamma angle. The most probable causes of the artifacts, however, were the aforementioned systematic errors with the energy windows being too narrow or the tilt of the source.

The three-fold CNR improvement of the 25% images over the 50% fill images was expected due to Equations 8 and 9, Section 1.22.1. Historically, lower fill factors have performed better with wide scenes, while 50% fill factor masks perform best with point sources. To improve future imaging, the lessons learned from this phase were applied. Future acquisitions were taken with 20% open windows centered about the middle of the backscatter energy spectrum, 114 keV. Using narrow energy windows cut out too much fluence, which the mask was designed to do.

Also, the edges of the detector output were discarded from future reconstructions. If the edges of the detector output were not discarded, the outline of the mask's borders was reflected in the back-projections which caused the line artifacts as shown in Figure 24. Another systematic error we discovered and eradicated during this phase was failure of the camera gantry drum to sustain the weight of the mask-shield fixture. An internal error "arm failure" occurred repeatedly during the final acquisitions. As a result of this failure, the camera head rotated almost two degrees. Hence, the mask-shield fixture was supported for future tests by a fabricated stand.

4.3.3 12.5% fill factor mask. The image quality continually declined as the target descended towards the mask until the target was no longer visible at $z = 1500$ mm. However, subsequent images taken within 1000 mm of the mask were resolved. Image quality declined for two reasons. First, the basic mask pattern eventually got too big for the detector. Second, there was a gradual decrease in gamma-ray throughput from mask self-collimation. Equation 10, Section 1.22.2, predicted the best resolution for the octic residue mask's hole diameter would be obtained at $z = 4000$ mm. This numerical solution matched our results in Figure 25 where Acquisition 3 and 4 qualitatively had the best overall resolution and contrast-to-noise.

The first problem arose because closer mask-target distances increased the magnification of the mask shadow on the gamma camera face plate. But with increasing magnification, the basic repeating region kept increasing in size until it no longer fit on the detector. Target to detector magnification is $m = f/z$. Because the camera's 4 mm resolution is FWHM, target features imaging larger than this size yielded the best possible results possible. The target's surface area, magnified by m , should remain less than 420 mm x 536 mm. The magnification exceeded these limitations at about $z = 800$ mm. Thus, we observed a decline in image quality within about a meter of the mask visible in the heavily blurred images at $z = 615$ and 998 mm in Figure 25.

Successful reconstruction requires a complete shadow of at least one basic mask pattern on the detector. Though this imaging situation would be uncommon in future testing, the DR algorithm was modified to handle such possible systematic challenges. Of note is that classical correlation could not have successfully reconstructed images in this case.

The loss of gamma ray throughput also degraded image quality as shown in Figure 26. The throughput decreased as the target neared the mask to a minimum value (crossover) and then throughput began increasing again for the nearest two images. Crossover occurred around $z = 1500$ mm. As a result, we were able to obtain the two closest reconstructions.²⁶ Again, those results were of poor image quality from aforementioned magnification of the mask shadow, and lower counts from self-collimation which dominated the results beginning at $z = 2000$ mm as shown in Figure 27.

Mask self-collimation effects occurred due to the mask thickness being comparable to the hole size. These effects describe the loss of off-axis illumination through the cylindrical holes of the mask. The maximum angle permitting throughput from an on-axis source is determined by the ratio of the detector's radial distance divided by $(z + f)$. Given the detector's active area, the distance to a corner of the detector face from its center is about 340 mm. The ratio 340 divided by $(z + f)$ should remain substantially less than the ratio of the hole diameter to mask thickness or 1.45 divided by 3.0 (0.48). At closer distances, the throughput vanishes entirely. This issue was only apparent with the octic-residue

mask because the holes are smaller than the other masks despite the thickness being the same. As a result, non-uniform illumination of the detector plane prevented reconstruction of high quality images.

The CAI system with octic-residue mask exhibited three major challenges with wide scenes. Self collimation, the inability of the detector to resolve the hole shadows, and the camera's inaccuracy in reporting position all contributed large errors to the reconstruction algorithm. Gamma camera positional error is not uniform on the detector surface²⁷. Event locations can be moved toward or away from the nearest PMT in a systematic manner which contributes to reconstruction errors. For example, even gamma camera readout errors of one mm can shift a hole shadow to a non-hole shadow and back-project the wrong intensity.²⁸ These errors prevented optimal reconstructed results even in the absence of backscatter.

4.4 PHASE IV. X-ray Source Tests

4.4.1 50% fill mask.

4.4.1.1 Initial tests. Image quality was poor for reconstructions with less than 1-million counts. Hence, all future tests would have at least 1-million counts for complex scenes. The reconstructed target was not in the center of the image because the center of the mask and detector were misaligned from using a temporary mask fixture. This misalignment presented an algorithm with an image that was cropped on its left side. The algorithm assumes geometrically centered raw detector data as the input. The misalignment caused events to be back-projected at the wrong angles and reoriented the target. The water jug sequence was reacquired once the permanent mask fixture was installed. As a result, the optical axis was aligned and the reconstructed jug was centered in the FOV as shown in Figure 3.

The water jug was 270 mm in diameter and 480 mm tall, though the water level was only up to 390 mm. Hence, the first reconstructed image showed geometric accuracy with changes due to the experiment magnification, discussed in the next section.

The bright halo was due to X-rays that missed the top of the jug and backscattered off the steel backstop. The top of the water jug top is narrower than the base. Accordingly, the source illuminating the

target from below and to the right created noticeable backscatter from the steel plate in the upper left quadrant of the reconstructed target. Water has a low attenuation coefficient, however some X-rays attenuated through the 270 mm jug and scattered off the steel in several directions depending on what energy they emerged from the jug. The X-ray's cone beam illuminated a circular area 600 mm across (100 pixels), centered in the FOV.

The size of the halo can also be attributed to the angle of incidence being at a slight angle in reference to the line connecting the target and the detector. There was roughly 10 degrees between the target's line of sight to the mask and to the X-ray tube. Because of this difference, the water jug's shadow should have been small because of its positioning against the back wall. The water jug's shadow should have been narrow and only stick out to the upper left by approximately $150\text{mm} * \tan 10 \text{ degree}$ or about 25 mm, which would be 2.5 pixels. The actual jug shadow is larger than the predicted size because of extra illumination. This extra illumination was caused by rays that missed the jug completely and also rays that attenuated through it. Near vertical angles of incidence enable X-rays to attenuate deeper through objects before higher probabilities of scatter occur. Conversely, there is a higher incidence of backscatter for X-rays with a high grazing incidence angle.²⁹

Masking the dark corners was necessary to ensure the reconstructed image was geometrically accurate with the lowest number of artifacts. Figure 2b has heavy, dark streaking. After masking, Figure 2c. shows the target as a bright blur against a darker background. The dark corners in the gamma camera output result from the target being somewhat "off center" relative to where the camera was "aimed".

In the ring reconstructions, the polyethylene backdrop sheets may not have been visible because the backscatter signal was weak in comparison to the 4-layer stack of rings. The rings were thicker and centered within the beam. The 600 mm x 600 mm polyethylene sheets were $\frac{1}{2}$ the thickness of the rings. Thus, the rings presented a stronger backscatter signal over the sheets. The edges of the sheets are not visible, because the cone beam's diameter against the wall was less than 600 mm across. As a result, the FOV in Figure 31 appears as a ring against a noisy, uniform background. The distortion in the 4814 mm reconstructed image is due to the ring leaving the cone beam at that mask-source distance. The rings are

approximately 56 pixels across, comparable to 280 mm. So, this sequence also exhibits geometric accuracy in the system.

One small contributor of background noise is X-rays that scatter multiple times into the mask. The X-rays that scatter multiple times continue losing energy. Hence, most X-rays will fall below the gamma camera's lower energy window. Though energy windowing removes most of this noise, this is one disadvantage of "flood" illumination over pencil beam illumination.

4.4.1.2 Optimized Acquisition Protocols. The reconstructed arrow shown in Figure 33, was obtained by using the standard 20% open energy windows. Wider windows were examined to see if letting more radiation in would improve or decrease the SNR. In theory, the mask should filter out the unwanted photons (not hitting the mask perpendicularly), but the camera's energy windows were also able to filter the incident spectrum. Narrower energy windows produced artifacts, just as in the area source tests. 20% open energy windows would be used for all subsequent testing. Using the camera's internal energy banding function did not improve image contrast. Therefore, acquiring more information over a larger range outperformed acquiring less information keeping the total counts constant. Changing the source type and uniformity correction type had no noticeable effect on the reconstructed images. After the optimal imaging protocol was selected, the DR algorithm was tested for depth and rotational accuracies with this image.

4.4.1.3 Geometry Change. Less scatter reached the detector as un-encoded noise. With the source closer to the target, fewer photons scattered off particulates in the air near the mask. In addition to this air scatter, the X-ray tube had unavoidable leakage on the side facing the mask. Due to size constraints of the room, we could not move the source any further. In order to closely replicate backscatter the source had to be close to the detector. However, we were able to displace it forward to maintain backscatter geometry and still reduce the air scatter. Additional shielding placed around the X-ray tube reduced septal penetration of the sides and scatter near the front of the mask.

4.4.1.4 Mask & Anti-mask. Mask and anti-mask image averaging was used to remove

background noise from the original images. First, the imaging process created an image based on spatial variation in counts collected on the detector surface. In theory, this variation should only be due to the mask shadow. However, illumination was both added and suppressed from scatter off other structures, lead X-rays, and shielding of inner pixels by pixels on the detector array's edges.³⁰ Variations in the amount of illumination were present in each mask and anti-mask image in Appendix C. These variations manifested as the blobby artifacts and diagonal streaks from upper right to lower left of the field of view.

In Figure 35, both the mask and anti-mask acquisitions were equal time and of the same target. As a result, averaging the two images removed the variations in counts versus position. The final result, shown in Figure 31c, was a clear arrow against a uniform background. The mask-anti-mask addition method created the most optimal reconstructed image with the 50% fill mask. It had the best sharpness and highest CNR because of a uniform background pedestal. CNR is quantitatively analyzed in Section 4.5.

Though the mask-anti-mask image was of greatest contrast, a CAI system operating in a military environment could not feasibly support imaging in this manner. First, the system would have to have two separate detector-mask systems mounted in order to take the mask and anti-mask image simultaneously. Such a system would be too costly and cumbersome to operate and if one component failed, the system would have to solely rely on noisier images like that in the separate mask or anti-mask images to identify roadside explosives. The current operational tempo on the battlefield requires a system with higher contrast against a background undoubtedly littered with other objects that will produce background noise and obscure the targets in other ways.

The 50% fill mask was suboptimal for the following reasons. First, higher fill factor apertures work better with point sources versus area sources. Second, the limited resolution of gamma camera was unable to resolve individual holes at the magnifications typical of extended scenes (5000 mm or more). Last, the signal was swamped by background. In particular, the "un-encoded" radiation that did not come through the mask to reach the detector became noisy artifacts when back projected by the DR algorithm. Errors in the assumed mask to detector and mask to target distances caused additional blurriness.

However, when these errors were reduced the overall improvement in the images remained suboptimal.

4.4.2. 25% fill factor mask.

4.4.2.1 Initial tests. The three-fold improvement in numeric contrast for the initial images was expected (Section 1.22.1). The shadows in both Figure 33a and Figure 33b are consistent with the source placement below and to the right of the target. However, the shadow behind the jug atop bricks is smaller than behind the jug atop poly. There is less of a shadow effect visible in the jug atop poly. In Figure 11a, the jug is placed closer to the target and intersects the cone beam where its diameter is smallest. The angle between the target and the horizontal is larger than 90 degrees. Though there is a good amount of true 180 degree backscatter, due to the aforementioned geometry much of the beam is scattered in multiple directions off the rounded surface of the jug. The dark shadow in Figure 33a is larger and darker than in previous reconstructions because the water jug is the thickest target used and attenuates a majority of the beam. The steel wall behind the jug does not backscatter a signal comparable as either the target or the steel in the rest of the scene. Any radiation that may have attenuated through the jug and hit the wall behind it would be of such low energy that it would not make it back through the jug within the energy windows. Thus, there is a dark spot behind the jug in the reconstructions.

The jug is illuminated more uniformly than when imaged on the lead. The poly sheets are not clearly delineated in the reconstruction, but there is a brighter, rectangular area below the jug commensurate with the placement of 3-sheet stack. The bottom right corner of the jug is the brightest because it is the closest to the beam. Hence, it is fully illuminated by the beam. The jug's rounded edges scatter the radiation in multiple directions making for a uniformly noisy background.

Because the raw detector output had dark areas, the uniformity corrections were reacquired. Uniformity corrections were always acquired without an aperture on, so the blobby texture was independent of whatever mask fixture we used. The uniformity corrections were correlated at the energy

ranges within our preset windows. After the new uniformity corrections were implemented, the raw detector output was uniform again.

4.4.2.2. Energy Spectrum alterations.

Decreased filtration (increased CR). The edges and corners in Figure 34 were darker because the target was projecting the edges of the mask on the detector. These areas on the detector contained inconsistent data and were excluded from the reconstruction. When the edges were included, horizontal and vertical smeared lines appeared as artifacts. Overall, however the images obtained with the decreased filtration were of high quality. The beam fluence increased and the overall exigent energy spectrum became more forward-peaked.

Widened Beam. The arrowheads were not uniformly illuminated. The upper right portion of the arrowhead appears brighter than the rest of the arrowhead because it makes first contact with the beam. The arrow was facing perpendicular to the detector. Thus, any X-rays from the source (on the floor to the right of the detector) would hit the arrow at an angle. The middle of the arrow is not as bright as the rest of the target. The only plausible explanation is that the lead filter inside the collimator may have rotated slightly, allowing a higher intensity to escape the collimator at the top and bottom. Initially, the 0.635 mm (.25 in) filter was used to decrease the dose rate in the vault. The thinner filters, 4.76 mm (3/16 in) to 3.18 mm (1/8 in) were so thin they easily rotated in the collimator chamber when being changed. It was standard procedure to ensure the filters, collimator, and lead nose cap were properly in place before warm-up and operation. However, several “before and “after” acquisitions were conducted with the narrow and wide beams. Removing and adjusting the collimator during these acquisitions may have caused the filter to shift and was not corrected for this series of tests.

The images are fuzzier than with the narrow beam because there is more air scatter. Unless the beam is perfectly collimated, any object (including air) that comes in contact with the beam will become a source of scattered photons.³¹ After the collimator was cut, the new cone beam’s intensity was measured by running a count-rate meter across the cone beam’s cross section against the wall. The results of that

measurement yielded a Gaussian profile. The anticipated profile had a flatter plateau with smooth fall off on each side because the beam was designed to be a uniform source of photons within the FOV. The cause of the Gaussian profile was the filter in the collimator. With the shorter collimator, most of the scatter inside the filter escaped it. Before, with the longer collimator, a large portion of the scatter inside the filter was stopped or scattered to even lower energies in the collimator body³². At the Gaussian profile's edges, there was not a sharper falloff because there was still a significant amount of backscatter off the steel backdrop. Hence, the count rate would have a more bell-like shape with a true peak at the center and gradual falloff to a significant background pedestal.

4.4.2.3. Multiple Object Scene. The objects are all noticeable, but the entire scene is very blurry because all three objects were smaller relative to the cone beam's illuminated area. Each object was also spherical, which produced scatter in multiple directions. The surface areas in direct contact with the center of the beam are the brightest. These areas are the brightest because it is where the beam hits the objects perpendicularly. Accordingly, the detector picks up the backscatter normal to these surfaces the strongest. The cylinder, shown at left in Figure 40, is only partially visible because during acquisition the water began leaking out of a small crack in the base. Though the cylinder also contained poly beads, those did not backscatter a signal stronger than the steel backdrop. The fingers of the glove were only faintly visible because they were approximately 25 mm in diameter. This diameter was at the extreme limit of resolution for our CAI system. Of note is that the fingertips, less than 25 mm in diameter, are not clearly resolved. The base of the scene is bright, yet blurred because it is only half-illuminated by the beam. The lower right corner of the base is brighter than the remainder because it is in the most contact with the source. However, the stack of poly sheets is the most uniformly illuminated because it presents the flattest surface to the source for uniform backscatter along the edge.

4.2.3. 12.5% fill factor mask.

4.2.3.1 Initial tests. The calibration images illustrated that the FWHM was smaller than with previous masks. The FWHM is smaller than with previous masks because the hole size is smaller. The FWHM with the 50% and 25% fill mask was 4 mm. Here, it is reduced to 3.7 mm.

The width shown in Figure 40 is due to three factors. First, the isotope source has dimensions and is, therefore, not ideal. Second, the small hole size in octic-residue mask limited the ability to image them and their detailed layout in the mask pattern. The octic-residue hole spacing is approximately half that in the previous two masks. Those holes were at the limit of being resolvable in the image. Third, the resolution limitations of the gamma camera cause a single point to be smeared because of the camera's internal PSF.

4.2.3.2 Arrow. The partial illumination of the arrow may have been because the X-ray source was inadvertently knocked or moved. Even the top of the backscatter halo is not resolved and appears truncated. Hence, it does not appear that misplacement of the arrow within the beam was at fault. Still, the bottom of the arrow is clearly delineated against a uniform, though noisy background.

All the octic-residue reconstructions were initially tested at 960 x 960 mm FOV sizes due to the overall blurriness of the images. The higher fill factor reconstructions were all initially tested at matrix size 1280 x 1280 or higher with good results. Increasing p to 26041 for this mask did increase the number of pixels in the final image. We successfully reconstructed the 12.5% arrow using 200 x 200 matrix size, or 40000 useable pixels.

In theory, this mask should have produced four to five times as many useable pixels as the quadratic or bi-quadratic masks, based on the increase in p -value. Previous reconstructions with the higher fill factor masks were $128 \times 128 = 16384$ pixels. Though there were no obvious self-collimation

effects when looking at a single, reconstructed point source, the extended scene reconstructions over various z-values confirmed the presence of self-collimation.

4.2.3.3 Multiple Object Scene. The images in Figure 42 do not support the octic residue mask out-performing the quartic as originally proposed. This is because the mask's small hole size is smaller than the gamma camera can resolve. The multiple object scene did not resolve well in both the quartic and octic-residue tests mostly because of the small sizes of the objects. Still, showing the mask could reconstruct such a scene with "shape-recognition" of such objects proves this proposed large-area CAI system could be successful in other applications using near-field imaging z-values of 5 to 15 m. Distances higher than that would certainly limit resolution of such small objects due to Equation 12. Of note, we were able to obtain comparable results to the quartic mask by smearing the mask in the reconstruction to compensate for the camera's resolution-induced blur. However, there was not a notable improvement in image quality given the extra post-processing in the algorithm.

4.2.3.4 Self-Collimation Investigation. Similar to the area source tests conducted at the same z-values (Figure 23) echoes were observed that brightened as the source neared the mask. The echoes were brightest in the six acquisitions nearest the mask, as shown in Figure 44. The increase in the max background corresponds to the increasing brightness of the artifacts in the upper right and lower left corners in Figure 44's images

In theory, when imaging away from the mask-detector centerline (all within the same plane) echoes would appear if the target was placed close to the edge of the FOV. However, there were no apparent gradations from one side to the other when the point source was imaged in this manner during calibration. In contrast, self-collimation effects were noticeable when imaging closer to the mask.

Targets were placed closer to the mask in order to increase the magnification of the mask shadow on the gamma camera face plate. Magnifications of 50 to 100% required values of $z = 2f$ (1320 mm) to $z = f$ (680 mm) respectively.³³ For continuity, z-values producing magnifications of 15 through 100%, per Equation 2, were investigated. Though the range of z-values from 600 to about 1500 mm allowed us to

resolve the holes in the mask shadow, this range also produced the most effects due to self-collimation as shown in Figure 45.

The self-collimation effect is due to the mask thickness being comparable to the hole size. When the source illuminates the detector from an “off-axis” position, there is a subsequent reduction in intensity because of the small angular subtense. As a result, the mask array A is scaled (see Appendix A). Shadows from off-axis holes are smaller than on-axis holes. As a result the mask shadow is changed and artifacts are produced.³⁴ These artifacts were limited but still present.

The range of z -values producing this effect was calculated using Equation 10. The hole size was 1.45 mm diameter and mask was 3.0 mm thick. Accordingly, the maximum angle at which a ray from a source (on-axis) will go through the mask is determined by the ratio of the maximum distance on the detector from its center divided by $(z + f)$. The detector face is about 420 mm x 536 mm. Therefore, the distance to a corner of the detector face from its center is about 340 mm. To limit self-collimation, the ratio $340/(z + f)$ should remain substantially less than $1.45/3.0 = 0.48$.

Our results assert that degradations from self-collimation were prominent when this ratio was higher than 0.15. Reducing the mask-detector distance was not an option, nor would have presented a large benefit. Reducing the mask-detector distance to reduce the self-collimation effects would have also reduced our ability to resolve the finer holes in this mask. Unfortunately, these “self collimation” effects reduced the overall contrast such that there was no marked increase in image quality despite the increase in useable pixels.

We investigated $p = 26041$ with finer spacing because it was the only octic residue pattern size reasonable for practical fabrication. The next lower p value was 73 and the next higher was approximately 160 billion.³⁵ Additionally, the higher p value corresponds to more independent bits of information in the final reconstruction. Accordingly, we expected a higher number of useable pixels per reconstruction. The octic residue mask should have had four or five times as many useable pixels as the quadratic or bi-quadratic masks, where p was 5000. With the previous mask, images were $128 \times 128 = 16384$ pixels. This entailed some “over sampling,” but the octic residue p value enabled larger matrix

sizes, potentially 200 x 200 or greater. In theory, the octic residue mask should have worked with such small holes because of the flat power spectrum of these masks. Available energy in the mask is spread over a wider spectrum so that less is available in the low frequency region available for imaging. As a result, the limited resolution of the gamma camera works to our benefit. Some of the high frequency components are discarded, but the desirable lower frequency ones are retained.

Though we expected the octic-residue mask to outperform the bi-quadratic mask, the fluence was limited in the range with optimal magnification of the mask shadow. The creation of this mask was the first application of a low open area mask that had the ideal autocorrelation function.³⁶

4.5 Contrast-to-noise and Resolution. This section compares the CNR and resolution for each set of reconstructions. First, the changes in CNR are explained as a function of changing imaging parameters. A complete discussion of the CNR covers both the effects from changing the imaging techniques and predicted results from changing the mask fill factor. Second, the effects of altering the mask fill factor on CNR is discussed. The optimal imaging technique and mask are selected following close analysis of each reconstruction's image quality. Last, a recommendation for an optimal CAI system for military detection of explosives follows based on the experimental results.

CNR.

25% fill factor reconstructions. The 25% fill reconstructions had the best overall CNR, SNR, and resolution. The average CNR and SNR were 14.7 and 4.65, respectively. There was a near 50% increase in CNR and SNR over the 50% fill mask results and nearly a 75% increase over the 12.5% mask results.

Both the arrow and rings were of high quality, produced by imaging with lower tube filtration and a geometry with reduced source-target distance. The reconstruction with the highest CNR was the arrow with the new geometry (CNR = 19.6 ± 0.5). The rings with lowered tube filtration had second highest CNR at 16.6 ± 0.8 . Changing the tube filtration is another common method to alter contrast. Increasing

the filtration raises the effective photon energy by removing low energy components. Conversely, lowering the filtration ensures lower energy incident radiation. In radiographic imaging, where bone and tissue have excellent subject contrast, having a higher amount of photoelectric absorption is desirable and produces higher contrast.³⁷ Here, we are solely relying on Compton scatter through a large “air gap” and using the mask to collimate the unwanted scatter. The primary reason contrast improved was because the count rate increased.

Though the rings had lower CNR, they had higher SNR because the background intensity was lower than in the arrow reconstruction. The rings only had 100,000 total counts per image, yet still had comparable intensity as the arrow images with 10^6 counts. Had the number of counts been the same, the ring reconstructions may have had better overall contrast and CNR because with a greater number of counts the standard deviation of the noise decreases with increasing number of counts. The background in the arrow reconstruction, though higher, was more uniform. Thus, the smaller standard deviation in the background for the arrow produced a higher CNR.

50% fill factor reconstructions. The 50% fill reconstructions had an average CNR of 8.5 and an average SNR of 3.2. The mask/anti-mask reconstruction had the highest CNR (11.0 ± 0.4) but the lowest SNR (2.7 ± 0.6) of all reconstructions. The high CNR is due to the intensity of the target being about the same as the others, yet the standard deviation of the background is so low it produced a large CNR. The mask and anti-mask averaging technique is intended to reduce the amount of artifacts in the image and improve contrast.³⁸ The coupling removed the gross variations in intensity in the background, making it more uniform in accordance with the concepts in Appendix B. Though uniform, the background pedestal also had one of the brightest intensities (69.7) which decreased the overall SNR. The high background pedestal, in addition to the extra difficulty of obtaining the separate images, made this the least favorable method for producing a high CNR image.

The second highest CNR reconstruction was the water jug ($\text{CNR} = 9.0 \pm 0.8$) after the change in geometry. The CNR was high because the background intensity was the lowest of all the images, coupled with a low background standard deviation. This was manifested as a dark, fairly uniform background

against which the jug stood out fairly well. The SNR was also highest at 3.6 ± 0.8 . These ratios affirmed that reducing the source-target distance and increasing the mask-target distance improved contrast by reducing the amount of air scatter. Previously, the source was so close to the mask that photons leaving the tube (via the collimator or from septal leakage) would enter the mask without even interacting with the target. The standard deviation in both the mean target and background intensities were slightly higher than the other targets mostly because of the rounded nature of the object not presenting a surface normal to the photon beam. Still, the contrast (difference in intensities between target and background) was so high the higher standard deviations did not drastically reduce the CNR.

The rings on lead bricks had better CNR than the rings on polyethylene sheets, 8.6 ± 0.8 versus 6.2 ± 0.7 , respectively. The SNR for the rings on bricks was second highest at 3.4 ± 0.9 mostly because the rings on the polyethylene backdrop nearly filled the entire FOV. Despite this increasing the backscatter signal, it had the highest amount of background noise of all the raw reconstructions.

12.5% fill factor reconstructions. The arrow reconstruction in Figure 41a was the only 12.5% reconstruction analyzed for CNR. The mean intensity (212.9), mean background (79.9), and standard deviation (19.4), produced a CNR of 6.9 ± 0.9 . The values for both the 128 x 128 and 200 x 200 matrix sizes were comparable within half a standard deviation, so only the results of the first image are listed. Reducing the fill factor from 50 to 25% increased the ability to resolve holes in the mask shadow. But with the 12.5% fill mask, the radiation not coming through the mask began to outnumber the radiation coming through the remaining holes. This mask was nearly opaque to radiation. This ameliorated the advantage of having more useable pixels. Contrast was not acceptable for any military necessity to quickly identify targets solely from image quality.

Effect from mask fill factor. Lowering the fill factor is one of the most common methods for improving the contrast. Until now, fill factors below 50% did not retain the ideal bi-level autocorrelation property required for optimized coded aperture imaging. The 25% fill mask was designed with "quartic" residues with p-value of 4357. The number of mask elements being smaller than the 50% fill mask ($p =$

5419) means there were less useable pixels in the image. However, we were able to increase the hole spacing from 3.5 mm to 3.9 mm and diameter from 0.122 in to 0.137 in. Doing so increased contrast of reconstructions by increasing the ability to resolve holes in the mask shadow. The 50% fill mask hole pattern was not discernable on the gamma camera which is another reason those images were of lower overall quality with respect to resolution and sharpness.

The contrast, the ratio of scene range of brightness over reconstruction background, was 3% for the 25% fill mask, 1% for the 50% fill mask. The contrast in the 12.5% mask was unacceptable and is not further discussed. The increase in contrast for the 25% over the 50% fill mask equates to the reconstructed image standing out better above background and measurement noise in the background signal. Though there is some small statistical fluctuation in the reconstruction background, the steady background can be subtracted out.

Contrast was improved by reducing the fill factor. For area sources, lower fill factor masks yield better CNR despite a slight decrease in signal.³⁹ Because the signal is proportional to the fill factor and the pedestal is proportional to the square of the fill-factor, the contrast was improved from 50% to 25%. From Equation 9, Section 1.22.1, reducing the fill factor from 50% to 25%, the contrast increased by a factor of 3.

Theoretically, the contrast for N sources should have been $1/N$, $3/N$, and $7/N$ for the 50%, 25%, and 12.5% masks, respectively. The factor of seven increase in contrast was not observed with the 12.5% fill mask because the results were severely hampered by noise and mask self-collimation effects that further reduced the detected photons.

Resolution. The optimized “rings with less filtration” reconstruction was used because it had the highest CNR and sharpness. Because the resolution is worse than 5 mm, the reconstructed image in Figure 34 is blurred. For 25 mm per pixel resolution, the inner ring in the reconstructed image would only span three pixels. However, the reconstruction clearly shows that a minimum of 25 mm resolution in the reconstructed image was achieved. This is consistent with calculations using the zoom factor, Equation 12, where f was 0.6 m and z was 5 m on average. Hence, the zoom factor was 0.12 for the majority of the

experiments in Phase 4. A resolution of 3 mm resolution corresponds to a resolution of $3 / 0.12$, or 25 mm, at the target. As a result, target objects smaller than 25 mm would not be noticeable in reconstructed images. This resolution was confirmed in the acquisition of multiple targets in one scene (Section 3.4.2.3).

Minimum Camera Resolution Required. The conclusion of the resolution tests is that excellent images can be obtained from 1024×1024 , 512×512 and to a degree even 256×256 detector mode outputs. There is an obvious tradeoff between image degradation in the lower matrix sizes and increase in processing time. With the 128×128 matrix size, sufficient image quality was obtained with smoothing of the internal mask array.

Modifications to the DR algorithm to accommodate 128×128 or lower would not present an acceptable cost-benefit ratio because there would not be a gain in image quality or overall processing time. The processing time for 512×512 is 4 times the speed of 1024×1024 (i.e. about 8.5 seconds). 256×256 runs about 16 times as fast as 1024×1024 (i.e. about 2.5 sec). Degrading to matrix sizes lower than 256×256 requires rescaling and trimming in post-processing. Over the course of several reconstructions, acceptable images are obtained with a comparable processing time just using 256×256 or above, as shown in Figure 41.

As artifacts were suppressed, degradation in resolution was observed. The decrease in resolution with increased smoothing (10 through 30 times) is commensurate with attempts to suppress aliasing by low pass filtering. The 64×64 matrix size was not useable. Hundreds of passes were required to remove the artifacts and the image was gone by that time. The standard deviation of the blob with which the mask array is convolved is approximately the square root of the number of smoothing passes.

The results of these resolution tests illustrate the importance of using continuous rather than pixilated detectors. If a scintillator was made of a higher density material, it could have a thinner cross section. The Anger camera used in these experiments used NaI (density 3.67). However, a scintillator made of Cesium Iodide (CsI) (density 4.51) or Germanate Detector (BGO), (density 7.130) could be used to make a higher efficiency coded aperture camera better suited for this application.

CONCLUSION

This research demonstrated that imaging wide, extended scenes was possible using an X-ray backscatter coded-aperture imaging system. The Anger Camera experimental set-up confirmed this technique by imaging scenes at 5 m, producing reconstructed images with CNR greater than 8.0, SNR above 3.0, and 25 mm resolution. Before this technology was proven, coded-aperture imaging systems were only used in astronomy applications to image scenes with few point sources on a dark background. However, extending this technology to image wide and complex scenes enables it to be used in the active detection of roadside explosives (IEDs) in military reconnaissance operations. This imaging system highlights organic material (with low attenuation coefficients) such as explosives used in IEDs that may be missed by other detection systems currently employed in theater.

Three large-area hexagonal, coded aperture masks were designed, built, and successfully tested with 50%, 25%, and 12.5% fill factors. The designs were the first ever to demonstrate lower fill factor masks, based on residues, retained ideal bi-level autocorrelation. Overall, the 25% fill factor reconstructed images had the highest CNR, resolution and sharpness. The average CNR (14.7) and SNR (4.65) showed a near 50% increase over the 50% fill mask results and nearly a 75% increase over the 12.5% mask results. Increasing the hole spacing allowed the system to image the holes in the mask shadow, therefore improving contrast.

The 50% fill factor reconstructions were sub-optimal because the overall CNR and sharpness was limited by the gamma camera's inability to resolve individual holes in the mask. With an average CNR of 8.5 the reconstructions clearly demonstrated that a target was obvious within the scene. However, longer z-values (and inherently more air-scatter) required in a final system demands the best possible image in a pristine laboratory environment.

The 12.5% fill factor reconstructions were lowest in quality with a CNR of 6.9. The already reduced signal was further limited by self-collimation effects due to the mask thickness being comparable

to the hole size. Though the mask should have had enabled the system to utilize more pixels, this advantage was not noticed when imaging extended scenes.

Altering the mask fill factor had the most noticeable affect on image quality, but optimizing the imaging parameters, experiment geometry, and dynamic reconstruction algorithm provided additional improvements to the CAI system's imaging capabilities. The dynamic reconstruction algorithm required trimming of raw detector output, smoothing of the internal mask array, and could generate sequences in near real-time. A final system would have faster processors to enable a system to reconstruct on-the-fly as it translated towards interrogated objects. Further, 20% energy windows ensured optimal CNR despite the CA masks being designed to collimate incident radiation not traveling normal to the mask surface. A shielded, narrow cone-beam, positioned as far forward of the mask as possible, was the optimal source-detector geometry for imaging. Providing additional shielding around the X-ray tube (not interfering with the FOV) reduced air scatter.

The 25% fill factor mask is the most desirable because it achieved the highest contrast in the experimental setup. Undoubtedly, a military operational environment in the desert would be wrought with dust, rain, and ground clutter that would produce higher background (noise) pedestals. Accordingly, the best possible image is desired prior to adding additional noise by increasing the range. Moreover, the source would have to be sturdily mounted in conjunction with the detector, where the entire system is hardened against excessive vibrations that would damage the detector crystals. Additionally, the recommended minimal matrix size (resolution) required for a final system would be 128 x 128 if the quilt-like artifacts shown in Figure 18 are acceptable for the end-user. However, given current operational constraints and limited end-user response time, the 256 x 256 matrix size is the minimal resolution for optimal CAI system performance (when including the user).

Simulations proved that X-ray backscatter coded-aperture imaging system could successfully reconstruct test images obtained at distances of 50 m with a high energy, 6 MeV LINAC as the source. The dynamic reconstruction algorithm successfully reconstructed simulated raw detector output produced from Geant. Though results were marred by air scatter, time gating the results improved the overall CNR.

An actual investigation of this technology at distances of 50 to 100 m is recommended, but with two requirements. First, a higher-energy, well-collimated source must be used. Second, a large, high-efficiency detector is required in this application because acquisition time and total photon counts are so low. A majority of the exigent beam is lost to the environment. Every possible photon that backscatters must be obtained by the detector. The BGO detector, for example, provides spectral coverage from about 150 keV to 30 MeV. BGO is a high-density material which provides good sensitivity over this difficult energy range. The energy resolution of the 127 mm x 127 mm, cylindrical BGO crystal is 4% at 10 MeV.⁴⁰ Thus, performing additional tests with a vehicle-mounted X-ray backscatter CAI system with these additional modifications could examine the capabilities and limitations of this technique at the ranges required by military operations.

REFERENCES

- ¹ United States. Headquarters of the Marine Corps. Field Manual Interim No. 3-34.119 Marine Corps Information Publication No. 3-17.01: Improvised Explosive Device Defeat. Sept. 2005, 3-1.
- ² Stephen Leary, *Improvised Explosive Devices (IEDs) & Counterinsurgency*. Library Institute for Defense Analyses. Revised and Updated Feb. 26, 2007. <<http://www.ida.org>>.
- ³ “Improvised Explosive Devices (IEDs) –Iraq”. [Globalsecurity.org](http://www.globalsecurity.org). 12 Mar. 2007. <<http://www.globalsecurity.org/military/intro/ied-iraq.htm>>.
- ⁴ Richard Lanza, “Measurement Times for IED Detection”, 2008, Massachusetts Institute of Technology.
- ⁵ Accorsi, Roberto, “Design of Near-Field Coded Aperture Cameras for High-Resolution Medical and Industrial Gamma-Ray Imaging,” June 2001, Massachusetts Institute of Technology, 20.
- ⁶ Mertz, L. and Young, N.O., in *Proceedings of the International Conference on Optical Instruments and Techniques*, K.J. Habell, Ed. (Chapman and Hall, London, 1961).
- ⁷ Horn, Berthold K.P., “Dynamic Reconstruction,” *IEEE Transactions on Image Processing*, 2008, submitted for publication, Manuscript ID: TNS-00021-2009, 2.
- ⁸ Zand, J. J. M. in ‘t. (1992, 1996) *Coded aperture imaging in high-energy astronomy*. [Nasa.gov](http://astrophysics.gsfc.nasa.gov/cai/coded_intr.html). <http://astrophysics.gsfc.nasa.gov/cai/coded_intr.html>.
- ⁹ Accorsi, “Design,” 24.
- ¹⁰ Accorsi, Roberto, “Analytic Derivation of the Contrast to Noise Ratio in Coded Aperture Imaging,” *Optical Society of America*, 2005, 1.
- ¹¹ Horn, “Dynamic Reconstruction”, 4.
- ¹² E. E. Fenimore, “Coded aperture imaging: predicted performance of uniformly redundant arrays,” *Applied Optics*, 17(22): 3562-3570 (1978).
- ¹³ Horn, “Dynamic Reconstruction”, 7.
- ¹⁴ Accorsi, “Design”, 30.
- ¹⁵ Accorsi, “Design”, 28.
- ¹⁶ Horn, “Dynamic Reconstruction”, 6.
- ¹⁷ Horn, “Dynamic Reconstruction,” 1.
- ¹⁸ *Ibid.*, 6.
- ¹⁹ *Ibid.*, 3.

- ²⁰ Sembiring, B., O'Connor, D., Li, A., van Riessen, C. "Grazing Incidence X-Ray Diffraction characterization of Corrosion Deposits by Carbon Dioxide on Mild Steels", International Centre for Diffraction Data 2000, *Advances in X-ray Analysis*, Vol.43, 319.
- ²¹ Park Medical Systems, ISOCAM II Operator's Manual. Park Medical Systems: 2005, 1-2.
- ²² Park Medical Systems, Inc. NEMA Performance Specifications for SMART Digital ISOCAM I and ISOCAM II Systems (1996)
<<http://www.med.harvard.edu/JPNM/physics/corps/park/specs.html>>.
- ²³ Zimmerman, Robert E. Instrument Quality Assurance: What is Required, Joint Program in Nuclear Medicine, Brigham & Women's Hospital, Harvard Medical School. Oct 2007.
<<http://www.med.harvard.edu/JPNM/physics/Zimmerman/Robert.html>>.
- ²⁴ Agostinelli, S. et al, *Nuclear Instruments and Methods in Physics Research A* 506, 250-303, (2003).
- ²⁵ The change in geometry was the same geometry change referenced in the 50% fill mask tests.
- ²⁶ Berthold K.P. Horn (personal communication, April 30, 2008).
- ²⁷ Berthold K.P. Horn (personal communication, November 5, 2007).
- ²⁸ Berthold K.P. Horn (personal communication, January 28, 2008).
- ²⁹ "Pinhole optics," Rice University Physics Department, Course 231. Rice.edu. 12 Mar. 2009.
<<http://www.owl.net.rice.edu/~dodds/Files231/pinhole.pdf>>.
- ³⁰ Knoll, Glenn F. Radiation Detection and Measurement, Third Edition. (Ann Arbor: John Wiley & Sons, Inc., 2000), 329.
- ³¹ Berthold K.P. Horn (personal communication, February 2, 2008).
- ³² B. Sembiring et. al, 319.
- ³³ K. P. Ziock et. al, 1617.
- ³⁴ John Ball and Tony Price. Chesney's Radiographic Imaging, Sixth Edition. (Malden: Wiley-Blackwell, 1995), 23.
- ³⁵ Dan-Cristian Dinca (personal communication, March 22, 2009).
- ³⁶ Berthold K.P. Horn (personal communication, July 21, 2008).
- ³⁷ Fenimore, "Tomographic," 1057.
- ³⁸ Berthold K.P. Horn (personal communication, April 13, 2008).
- ³⁹ Zand, J. J. M. in 't. (1992, 1996) Coded aperture imaging in high-energy astronomy. 24 Apr 2008.
<http://astrophysics.gsfc.nasa.gov/cai/coded_intr.html>.

- ⁴⁰ Ball, 21.
- ⁴¹ K.P. Ziock et. al, 324.
- ⁴² Horn, “Dynamic Reconstruction,” 7.
- ⁴³ “Bismuth Germanate Detectors.” Nasa.gov. 14 April 2009
<<http://www.batse.msfc.nasa.gov/gbm/instrument/description/BGO.html>>.
- ⁴⁴ Berthold K. P. Horn, “Sequence with bi-level auto-correlation property equals its own DFT,” *IEEE Transactions on Image Processing*, 2008, submitted for publication, 4.
- ⁴⁵ Accorsi “Design”, 36.
- ⁴⁶ Horn, “Dynamic Reconstruction,”3.
- ⁴⁷ Ibid., 4.
- ⁴⁸ Ibid., 1.
- ⁴⁹ T.M. Cannon and E.E. Fenimore, “Tomographic Imaging using uniformly redundant arrays,” *Applied Optics*, 18(7): 1052-1057 (1979).
- ⁵⁰ Zand.
- ⁵¹ L.D. Baumert, Lecture Notes in Mathematics No. 182. “Cyclic Difference Sets”, (Berlin: Springer, 1971).
- ⁵² Baumert.
- ⁵³ Fenimore, 337.
- ⁵⁴ Baumert.
- ⁵⁵ Berthold K.P. Horn (personal communication, January 11, 2008).
- ⁵⁶ Horn, “Sequence,” 7.
- ⁵⁷ Ibid.
- ⁵⁸ Berthold K.P. Horn (personal communication, January 11, 2008).
- ⁵⁹ Horn “Dynamic Reconstruction,” 7.

ACKNOWLEDGEMENTS

My thesis advisor, Dr. Richard Lanza, has been my mentor, counsel, teacher, and guide throughout the duration of my master's work. He spent countless hours teaching and coaching me to acquire the necessary background theory requisite for study in nuclear detection and research in general.

Dr. Gordon Kohse spent countless hours helping me in the laboratory and machine shop. Where there was a will and creativity, Dr. Kohse assisted me preparing the lab, transporting a ton of concrete blocks for radiation shielding, and fashioning lead shields without contaminating myself.

Professor Berthold K.P. Horn dedicated hours of instruction on signal processing and image reconstruction. His professionalism, sense of humor, and patience is appreciated immensely.

Professor Jacquelyn Yanch provided irreplaceable assistance with scientific writing and professional support any time it was needed.

American Science & Engineering (AS&E) from Billerica, MA. AS&E provided the X-Ray source and hours of engineering support in preparation and execution of this research project. Without their modeling, analysis, and assistance ameliorating problems as they arose, this research could not have happened.

Dr. Vered Anzenberg was my office mate, colleague, and best friend while at MIT. She provided me with a lot of constructive criticism on my final product and tremendous support in countless other ways.

Mrs. Rachel Batista was always supportive with both administrative requirements, assisting me with seeking professional development opportunities within the department, and supportive friendship.

The MIT Facilities evening janitorial staff who let me back into my office or lab on the countless occasions when I locked myself out.

The undergraduate curriculum at the United States Military Academy at West Point prepared me for this thesis work, the profession of arms, and for life. I also thank the U.S. Army for providing me with the opportunity to attend advanced schooling. Serving my country and leading Soldiers has been the most rewarding and professionally fulfilling experience I have had to date. This thesis is dedicated to my family and my extended military family, especially those who gave the ultimate sacrifice.

APPENDICES

Appendix A. An Addendum to Coded Aperture Imaging Mathematics

A.1 Convolutions. The convolutions are performed with the Discrete Fourier Transform (DFT).

Direct convolution is computationally expensive with large numbers of holes and as a result DFTs are used instead of directly convoluting the mask matrix M with whatever decoding array is used. DFTs can be implemented because convolution in the frequency domain corresponds to multiplication in the spatial domain.⁴¹ In the real case, $P(x, y)$ also has background noise N added, whereby the resultant transforms dictate:

$$F[P(x, y)] = F[O]F[M] + F[N], \quad (\text{A-1})$$

where F denotes the Fourier Transform, and N is the background noise. Therefore, to obtain the estimate of the original object from $P(x, y)$ one obtains:

$$\hat{O} = F^{-1}\left(\frac{F(P(x, y))}{F(M)}\right) - F^{-1}\left(\frac{F(N)}{F(M)}\right) = O - F^{-1}\left(\frac{F(P(x, y))}{F(M)}\right)^{42} \quad (\text{A-2})$$

where F^{-1} denotes the inverse FT. Therefore, the goal is to optimize Equation A-2 to produce the most ideal reconstruction of the original object. Further discussion on the mathematics of CAI and DFTs can be found in [3],[10].

A.2 Mathematics of Mask and Anti-mask Addition. This section describes the image formation process using the anti-mask and the mathematics of coupling the two images. Let \times denote convolution and $*$ denote correlation.

Encoding. The anti-mask pattern (mask rotated 60 degrees) is related to the original mask and ideal mask pattern by the relation

$$AM_z(x, y) = 1 - M_z(x, y) = \frac{(1 - M_{\text{pattern}})}{2}, \quad (\text{A-3})$$

where $G(x, y)$ is the photon distribution on the detector and $M_z(x, y)$ is the original mask pattern not rotated. The object's projection through the anti-mask is encoded in the same manner as the mask image, but gives a different distribution

$$G(x, y) = \sum_z [O_z(x, y) \times AM_z(x, y)], \quad (\text{A-4})$$

where $G(x, y)$ is the photon distribution on the detector.

Decoding. To regain the anti-mask image \tilde{O} , $P(x, y)$ must be correlated with a decoding array $A(x, y)$, also magnified according to the geometry of the experimental setup where

$$\tilde{O}(x, y) = G(x, y) * AM(x, y) = O_z(x, y) \times AM(x, y) * AM(x, y), \quad (\text{A-5})$$

which simplifies by the commutative property to

$$\tilde{O}(x, y) = O_z(x, y) * (1 - M(x, y)) \times (1 - M(x, y)), \quad (\text{A-6})$$

where

$$(1 - M(x, y)) \times (1 - M(x, y)) = \frac{N(\delta - 1)}{4}, \quad (\text{A-7})$$

from Equation 6, Section 1.21.2.

There are two equivalent ways to obtain the final image. Each way reduces the background pedestal and removes artifacts. In the first method, the mask image \hat{O} , and anti-mask image \tilde{O} , are reconstructed separately as described above and then the results are averaged where

$$(\hat{O} + \tilde{O})/2 = [(O * N(\delta + 1)/4) + (O * N(\delta + 1)/4)]/2, \quad (\text{A-8})$$

or, equivalently

$$(\hat{O} + \tilde{O})/2 = \frac{O * N\delta}{2} = O * \left(\frac{N}{2}\right), \quad (\text{A-9})$$

which removes the background pedestal.

There is also a second method, in which the raw anti-mask data is subtracted from the raw mask data

$$(\hat{O} - \tilde{O}) = (F \times M) - (F \times (1 - M)) = F \times (2M - 1) = F \times M_{pattern}, \quad (A-10)$$

and the result is correlated with the ideal underlying mask filter to obtain the initial image where

$$O \times M_{pattern} * M_{pattern} = O * (N\delta) = O * N. \quad (A-11)$$

A.3 An empirical demonstration of the decrease in contrast from imaging a point source to imaging an area source.

The contrast for a reconstructed coded-aperture image is directly related to both the mask fill factor and if the source is a point source or an area source (collection of point sources). In the simplest case, if a point source were imaged using a CAI system it would cast a mask shadow on the detector which would then be back-projected onto the scene. From the source position in the scene, the parts of the detector visible through the mask would be illuminated. When viewed from any other position (at least 1 resolution element away from the source) only a fraction r will be illuminated.⁴³ In the reconstructed image, the source location will have a peak intensity of amplitude A . The background has an intensity, I , a fraction ff as high as the peak where $I = A * ff$. For the 50% fill mask, the fill factor $ff = 0.5$. Thus, a single point source, will have a contrast (peak – background)/background given by

$$Contrast_{1Source} = \frac{(A - A * ff)}{A * ff} = \frac{(1 - ff)}{ff} = 1. \quad (A-12)$$

The peak height above the background = the background height. Masks with low ff increase this contrast. However, lower values of ff lowers the signal and reduces SNR.

For N multiple sources, of equal strength at different locations within the scene, linear superposition applies. The peaks in the reconstructed image at all the source locations add to the background of the other sources. The intensity in the reconstructed image at each source location is $A + A(N - 1) ff$. At all other locations, the intensity is $A N ff$. Each source contributes to the background

but only one contributes to the peak at a particular source location. Mathematically, the contrast for multiple sources is given by

$$Contrast_{N\ Sources} = \frac{(A + A(N-1)ff) - AN * ff}{AN * ff}, \quad (A-13)$$

which reduces to

$$Contrast_{N\ Sources} = \frac{Contrast_{1\ Source}}{N}. \quad (A-14)$$

Therefore, contrast is inversely proportional to the number of sources. An area source can be divided up into N point sources. Those point sources, for our purposes, must be one resolution element in area. Accordingly, an area source made up of N resolution elements will have contrast of $1/N$ times the contrast for a single point source.

Appendix B. Coded Aperture Mask Design

B.1 Overview. The design of the coded aperture masks in this research was largely defined by selecting a mask with ideal bi-level autocorrelation properties with the largest possible number (and smallest diameter) of mask elements to increase the overall signal. The limitations of the detector were also taken into consideration. The Mask Design process involved:

- picking a suitable prime p suitable for bi-level autocorrelation
- creating a one-dimensional, binary sequence using residues
- selecting the number of rows required to create a two-dimensional sequence with ideal bi-level autocorrelation
- creating a two-dimensional array from

Selecting the modulo p is limited by four factors. First, ideal bi-level correlation patterns only exist for certain values of p . Second, the number of independent pixels in the reconstructed image is equal to p . Accordingly, larger values of p are desired. Third, the size of p is limited because the finalized 2-D array has to cast a mask shadow that will fit on the detector's active area. Finally, the hole spacing cannot be too small because limitations of the detector will prevent optimal resolution if the mask hole spacing (in cycles per mm) is smaller than what the system Modulation Transfer Function allows.

B.2 Bi-level auto-correlation Property. Ideal images are obtained when using a mask family with ideal bi-level autocorrelation. Because of bi-level autocorrelation, off target responses are the same in all areas and are easily removed as pedestal noise.⁴⁴ Periodic auto-correlation of the pattern has only two values, a "1" for zero-shift and "0" for all other shifts. The power spectrum (magnitude of the Fourier transform) is also 2-valued 1 value for DC and another value for all other frequencies.⁴⁵

For imaging distance or planar sources, the Uniformly Redundant Array (URA) is ideal because it accomplishes autocorrelation as shown in Equation 5, Section 1.21.2.⁴⁶ Though there are 8 classes of coded aperture families, URAs based on cyclic difference sets are preferred because it is the most systematic method for producing the ideal bi-level autocorrelation. A full discussion on CA families and

array design is discussed in References [3], [4], [7], [8], [10]. The mask pattern's autocorrelation function, ideally a delta function, constrains both the pattern and how the shifted projections are detected.⁴⁷ And unlike Random or Non-redundant arrays which have non-optimal imaging properties, URAs require every point of the object to be uniquely encoded on the detector. The decoding array is simply the Fourier Transform of the mask pattern. The FT (power spectrum) is flat.

B.3 Cyclic Difference Sets. A cyclic difference set D is the set of k numbers with integer values between 0 and p - 1, where all possible differences modulo p are taken. All solutions between 1 and p - 1 appear z times within D. Binary sequences are typically used where a_i ($i = 0, \dots, n - 1$) is equal to 1 if i is a member of D and $a_i = 0$ otherwise. The cyclic autocorrelation c_r of a_i is⁴⁸

$$c_r = \sum_{i=0}^{p-1} a_i a_{\text{mod}(i+r, p)} = \begin{cases} k & \text{if } \text{mod}(r, p) = 0 \\ z = \frac{k(k-1)}{p-1} & \text{if } \text{mod}(r, p) \neq 0 \end{cases} \quad (\text{B-1})$$

where a_i represents the mask pattern, assigning a transparent element to $a_i = 1$ and an opaque one to $a_i = 0$, and r is the number of 1-D rows in the mask.⁴⁹ Equation B-1 corresponds to a delta function. Thus, a mask pattern generating a_i will create the best image possible. Because each difference $i - j$ between a_i and a_j is sampled, these arrays are called URAs.⁵⁰ Why the HURA is the best selection for this application is discussed next.

From Equation B-1, the largest possible difference between k and z results in the best possible CNR (k determines the signal and z the background noise). The maximum difference is reached if $n = 4t - 1$, $k = 2t - 1$ and $z = t - 1$ if t is integer⁵¹. These cyclic difference sets are called Hadamard difference sets. There are three types, according to the value of n. A complete discussion on cyclic difference sets are in references [2] [22]

B.4 Quadratic Residues. Quadratic residues generate the members of D from the squares, modulo n, of the first $(n + 1)/2$ integers. To design an ideal mask, one must first select the largest possible p-value (call this a prime?) suitable for the imaging system's FOV (or active area). Larger p-values are desirable

because more pixels are available in the resultant image. The basic pattern is created by generating a 1-D sequence of opaque and open areas based on quadratic, bi-quadratic or octic residues depending on the desired fill factor using Equation B-1.

The number n is a quadratic residue modulus p if there exists a number j such that $j^2 = n \pmod{p}$. Bi-quadratic residues and octic residues require $j^4 = n \pmod{p}$ and $j^8 = n \pmod{p}$, respectively. For n -values from 0 to $p-1$, each value is multiplied according to the residue. The remainders dictate which entries of the 1-D sequence are opaque or open. To illustrate this process, one can use a small p -value of 7 as shown in Table B-1. From 0 to 6 ($p-1$) the values would be listed first, then squared. Next, the quadratic residue is the remainder of $j^2 \pmod{p}$. Finally, the series of residues are 1, 2 and 4. As a result, the 1-D sequence of 7 spaces would consist of holes in the 1st, 2nd, and 4th spaces.

Table B-1. Generation of 1-D sequence using quadratic residues for example prime number, $p = 7$.

j	j^2	$j^2 \pmod{p}$
0	0	0
1	1	1
2	4	4
3	9	2
4	16	2
5	25	4
6	36	1

Finally, the 2-D sequence is generated by adding additional rows of the 1-D sequence atop the first with each row shifted r spaces to the right. The modulo p also dictates the number of rows. The resulting pattern will only have ideal bi-level auto-correlation properties for two values of r , either r_1 or r_2 , that together sum to p ($r_1 + r_2 = p$). A complete discussion on ideal mask design is in [9], [10].

B.5 HURAs. Though square Modified Uniformly Redundant Arrays (MURAs) are used most often in CAI, the hexagonal URA (HURA) was implemented in this problem. Both the square and hexagonal URAs have four copies of the basic pattern, but the HURA has a central hexagon surrounded by three half-copies as shown in Figure B-. The most compelling reason why HURAs were chosen over MURA masks is because MURAs do not have ideal bi-level auto-correlation properties. Instead, they create tri-

level auto-correlations where there is a result for zero shift and two different results for other shifts.⁵² Reconstruction is not possible with the mask pattern itself, but requires an additional, modified mask pattern. Also, there are two sets of transform values in the frequency domain which means the transform is not desirably flat and SNR will be negatively affected.

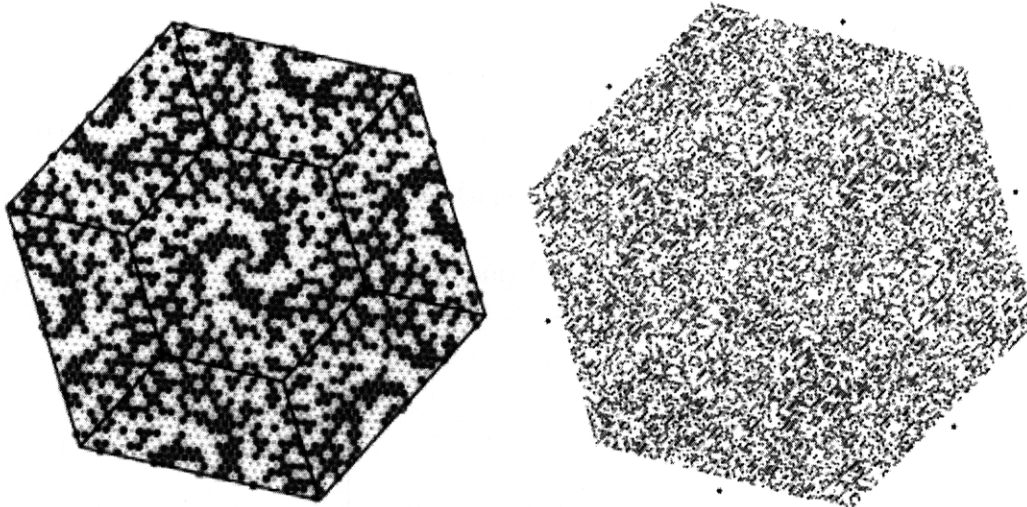


Figure B-1. A Hexagonal Uniformly Redundant Array (50% fill factor) is shown at left ($p = 643$) with the basic repeating pattern outlined.⁵³ The actual 50% fill mask drill pattern used in backscatter experiments ($p = 5419$) is shown at right for comparison. Image is from [10].

HURAs have other advantages over MURAs to obtain the most ideal images given the constraints of this problem. HURAs are similar to MURAs but are simply emplaced differently on another grid. HURAs allow more mask elements per unit area given fixed hole spacing. Consequently, the signal is improved due to a larger fractional open area. Square tiles can have hole sizes $\pi/4$, or 0.7853, whereas holes in hexagonal tiles can occupy $\pi/(2/\sqrt{3})$ or 0.9068.⁵⁴ Furthermore, more mask elements per area increases the number of available pixels in the final image, improving overall resolution. The ratio of mask elements per unit area for hexagonal versus square patterns is $1/\sin(60)$ or $2/\sqrt{3}$. The ratio of round hole area to HURA mask element area is $3/\pi$ as opposed to only $\pi/4$ for the MURA

HURAs also have practical advantages over MURAs. The cheapest fabrication method involves drilling round holes. The hexagonal hole shape is the closest fit to a round hole. Also, HURAs can become their own anti-masks when rotated 60 degrees versus a full 90 degree rotation for the MURA.

Finally, the HURAs FOV is best matched to the Anger Camera's rectangular FOV. When the desired FOV does not require on axis alignment or a unity aspect ratio, a hexagonal FOV has less wasted image area than is a square pattern on the order of $12/(\pi^* \pi)$.⁵⁵

Proper selection of p and r according to the following equations creates a 1-D sequence and 2-D HURA mask with the ideal bi-level autocorrelation property, as described in Paragraph 1.2. The largest prime value is chosen such that

$$p = a^2 + ab + b^2, \tag{B-2}$$

where a and b are integers. The number of rows must be chosen where the relations

$$r^2 \equiv (r - 1)(\text{mod } p), \tag{B-3}$$

and,

$$p = r_1 + r_2, \tag{B-4}$$

hold, where r is the number of rows, and r₁ and r₂ are simply two possible values of r that sum to the prime in Equation B-4.⁵⁶

Appendix C. Addendum to X-Ray Experiments

C.1 Water Jug Sequence with 50% fill mask. The entire water jug sequence, from $z = 4770$ to $z = 5185$ mm in 80 mm increments, is shown in Figure C-1. Contrast was exceedingly low due to a temporary mask fixture allowing in background noise and errors in the source-mask distance. The reconstructions at $z = 4928$ mm, 5004 mm, and 5087 mm were of the highest quality due to magnification effects.

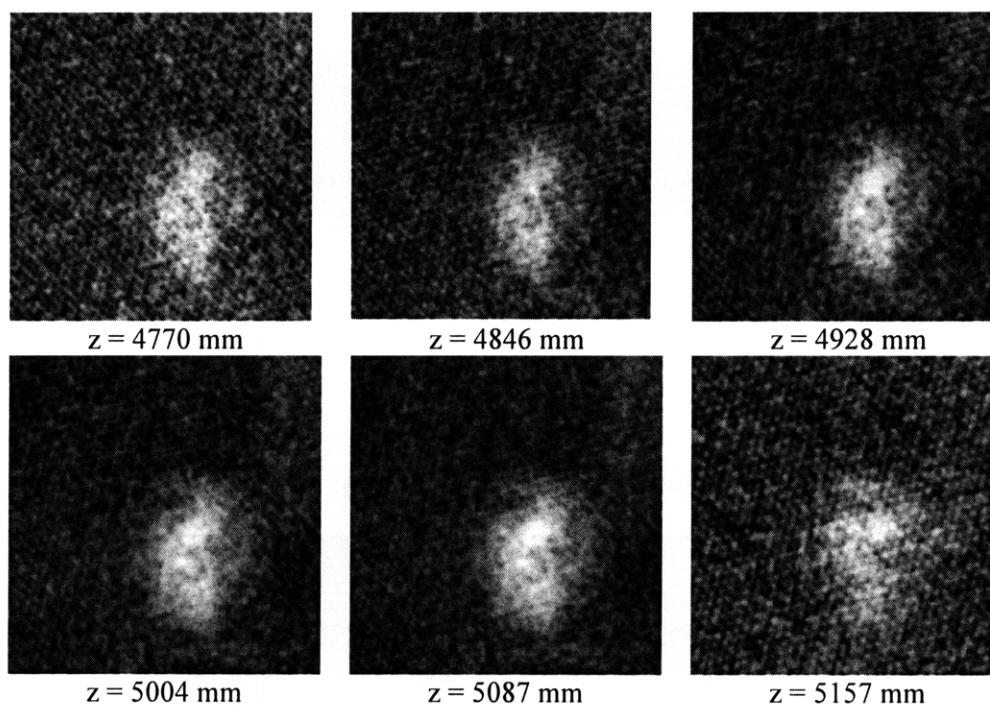


Figure C-1. 50% fill reconstruction sequence of water jug with optical axis aligned. Image matrix sizes are 256 x 256 covering a 960 x 960 mm FOV.

C.2 Polyethylene Ring Sequence with 50% Fill mask.

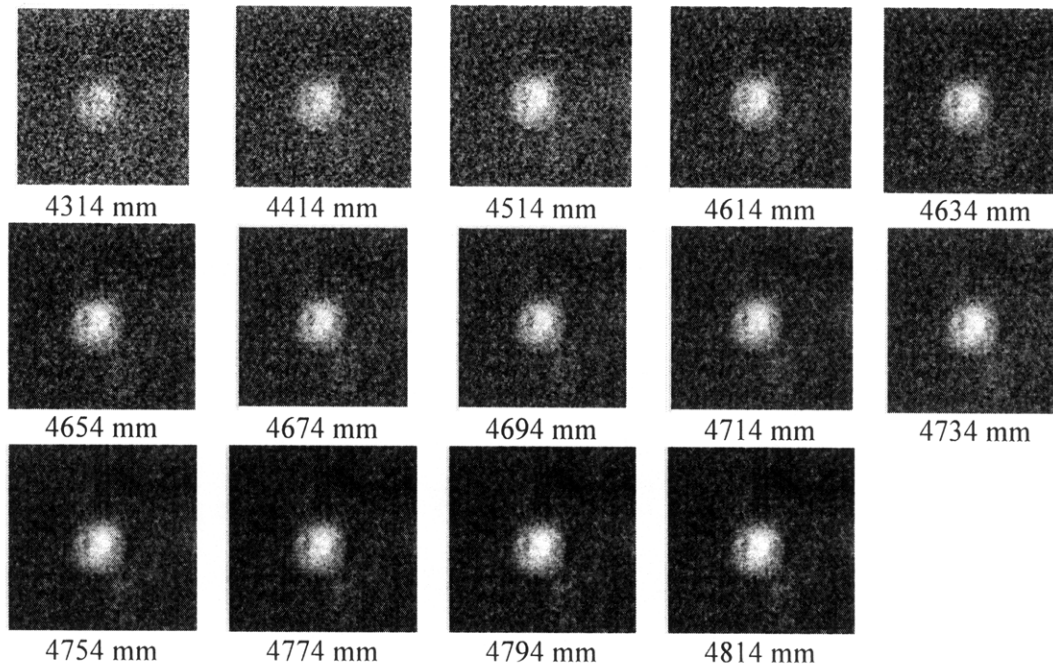


Figure C-2. 14-frame reconstructed sequence of the polyethylene rings on poly sheets. The contrast improves nominally as the sequence progresses from near to far. Image matrix size is 128 x 128 covering a 1536 x 1536mm FOV.

C.3 Arrow Comparison for old geometry and new geometry.

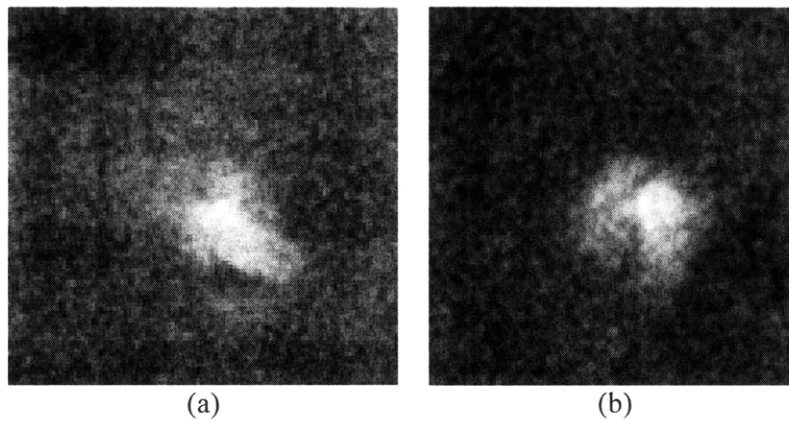


Figure C-3. Reducing the source-target distance and increasing the mask-target distance improved contrast. The arrow ($z = 5208$ mm) was imaged with a) old geometry pointing to the upper left and b) new geometry and pointing upright. Images cover a 1280 x 1280 mm FOV.

C.4 Mask and Anti-mask. The first three reconstructions in both the mask and anti-mask sequence are heavily marred by artifacts. The arrow is not discernible. The outline of the arrow, though blurred, is noticeable in the last three reconstructions in the sequence at $z = 347, 397,$ and 4470 mm.

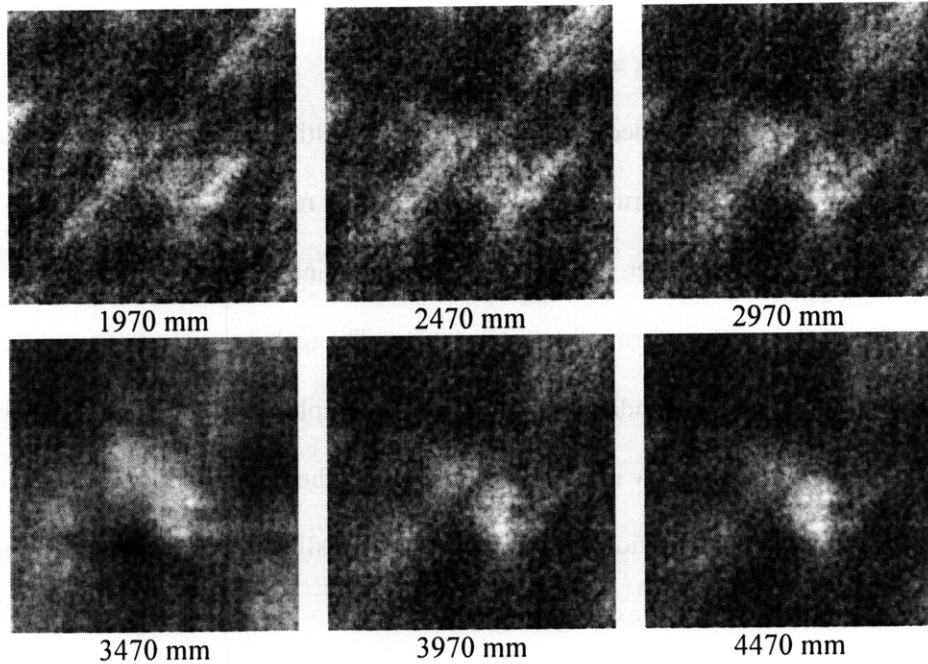


Figure C-4. Reconstructed arrow sequence with 50% fill mask. Image FOV is 1280×1280 mm.

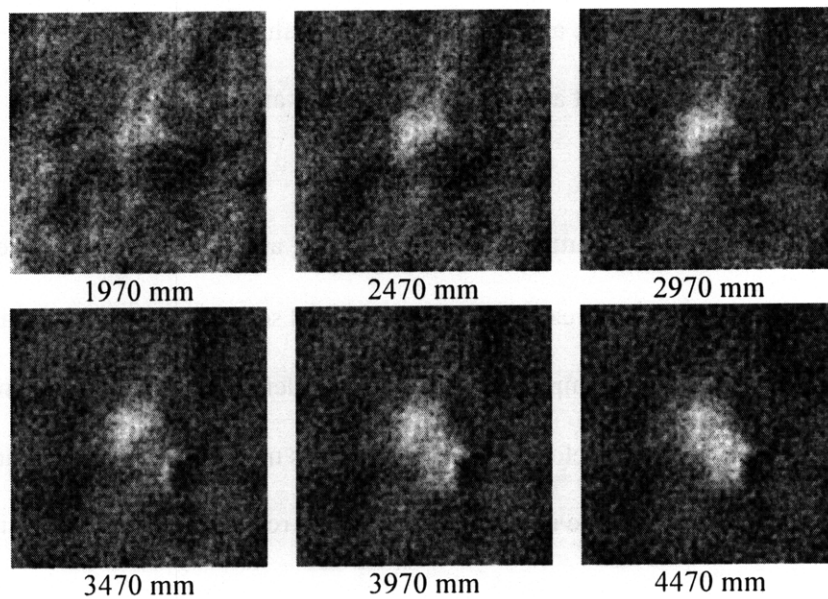


Figure C-5. Reconstructed arrow sequence with 50% fill anti-mask (rotated 60 degrees). Image FOV is 1280×1280 mm.

C.5 Updates to the Dynamic Reconstruction algorithm.

Earlier versions of the dynamic reconstruction program produced streaking artifacts in the output. Two of the most important modifications included: applying a normalization to deal with streaking artifacts, and smoothing the internal mask array.

First, a "normalization" was applied to remove artifacts resulting from discretization and sampling on a finite grid. In ideal reconstruction, a spatially uniform raw image should yield a spatially uniform reconstruction. However, aliasing and finite sampling results in non-uniform reconstructions from even the most uniform of detector output. The real reconstructions contain "streaking" and "mottling" artifacts dependent on the size of the sampling interval. These artifacts can be suppressed by first pre-computing the raw image and then dividing the reconstructions pixel-by-pixel with this image which serves as a calibration. For each test series, calibration images were computed according to the imaging parameters and experimental geometry.

The second algorithm modification was adding smoothing of the internal mask pattern. Smoothing the pattern used in the back-projection suppressed some aliasing artifacts. However, this technique required that the mask be treated as having continuous values in the 0 to 1 range instead of binary values equating to open, transparent areas or closed, opaque areas.

C.6. Contrast-to-noise empirical estimate. Using ImageJ™, an area was manually defined inside the outline of the respective target. This area was carefully defined so as not to include areas near the inner or outer edges of the target. For example, an inner area was defined in the following manner for the 50% fill water jug reconstruction shown below in Figure C-6. This method was repeated three times and the mean intensity averaged. Repeating the inner area was done to reduce the error in that measurement.

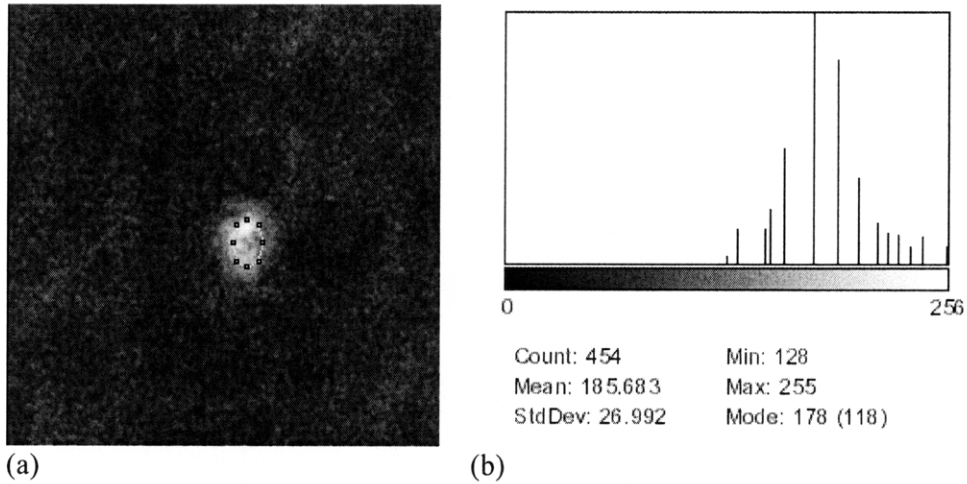


Figure C-6. Calculation of mean intensity for 50% fill factor water jug reconstruction. An area was outlined well inside the target shown in a) and a b) histogram was produced. Images were processed using ImageJ.

The background area was identified elsewhere in the image far away from the target. This method is shown in Figure C-7. Contrast was defined as the difference between the average intensity in the target area and the average of the “background” area. Then determine the standard deviation of the background area. The CNR is the ratio of the "contrast" to the standard deviation of the background. Only images where the target was fully illuminated by the beam were analyzed.

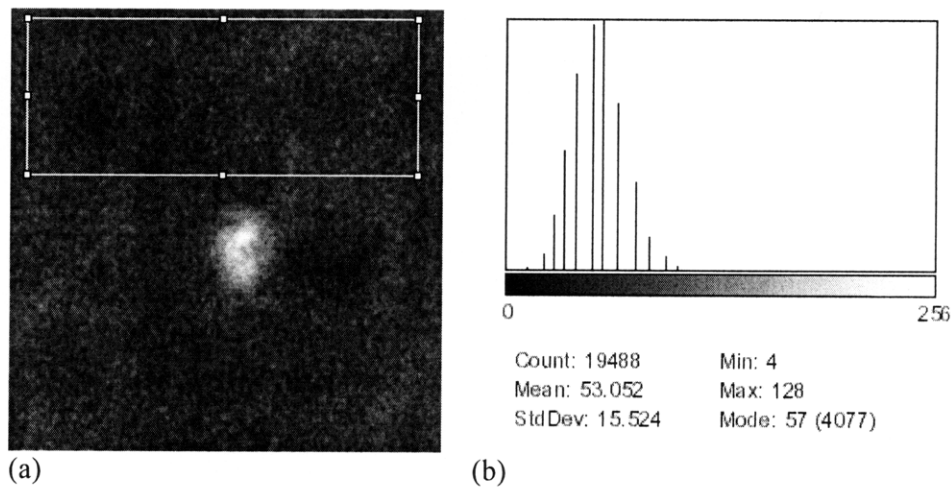


Figure C-7. Calculation of mean background and standard deviation in background. A large area in the background was selected far from the target and a histogram produced. Images were processed using Image J.

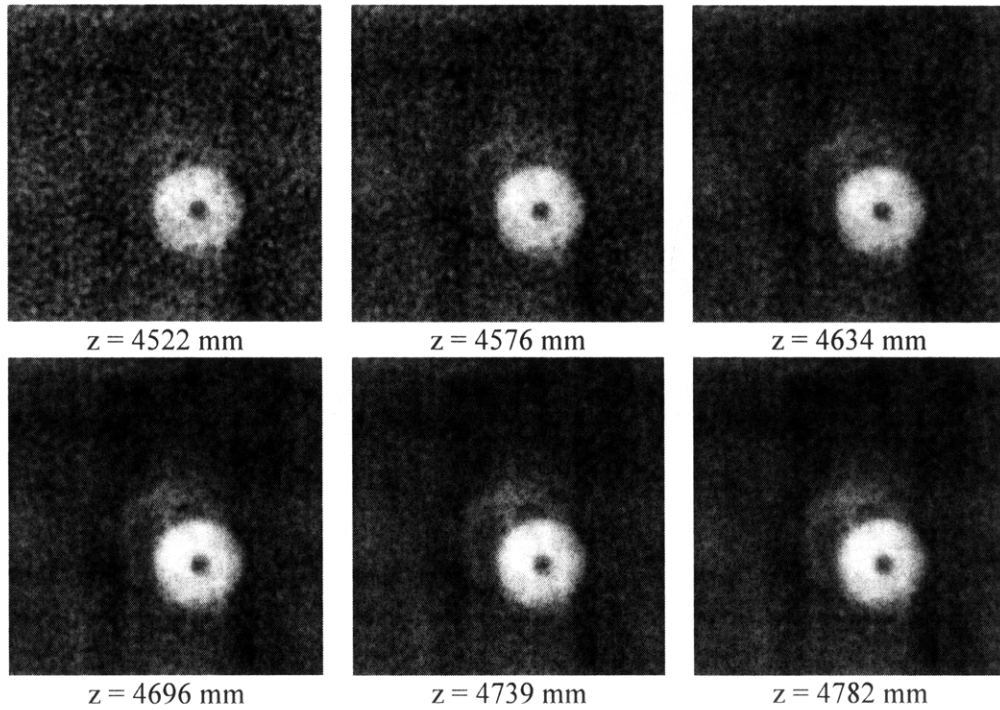


Figure C-8. Reconstructed rings with 25% fill mask. 100K total counts were acquired per image. Animation was near to far. Image sizes are 128 x 128 pixels covering a 1280 x 1280 mm FOV.

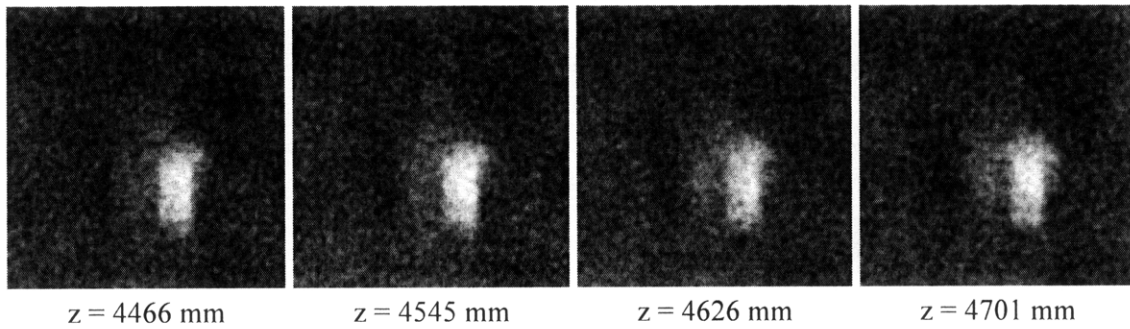


Figure C-9. Arrow sequence, 25% fill mask. Image sizes are 128 x 128 pixels covering a 1280 x 1280 mm FOV.

C.7. Widened Cone Beam. The reconstructed arrow, shown after the cone beam was widened, is shown below. The sequence is shown near to far. The corners ($-c = 175$) and edges ($-e = 20$) of the raw detector output were trimmed to remove the dark areas. Even after trimming, there are dark blobby artifacts surrounding the arrow in all the images. The arrow is not resolved in the near image at $z = 2502$ mm. The arrow is resolved in all later acquisitions and developed a backscatter halo against the steel.

This halo becomes more noticeable as the target nears the wall.

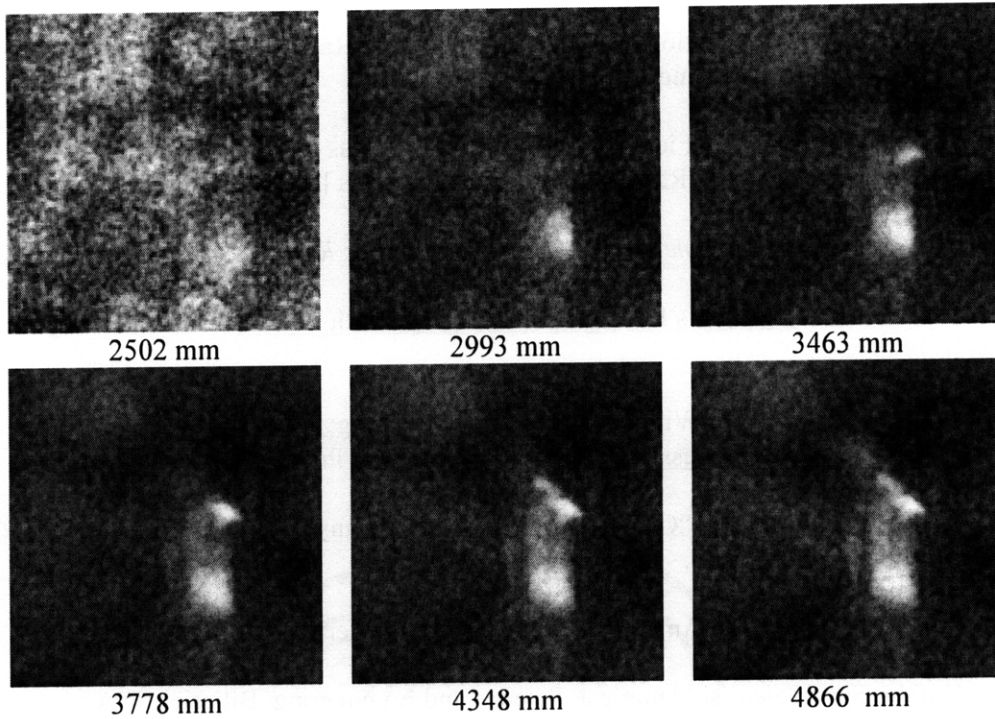


Figure C-10. Reconstructed arrow sequence after widening of cone beam from $z = 2502$ to 4866 mm. Horizontally streaking artifacts remained even after trimming detector output. Image size is 128×128 pixels covering a 1280×1280 mm FOV.

The near arrow at 2502 mm is not visible because a majority of the arrow is not illuminated by the beam at that z -value. The arrow was not fully illuminated by the source in the first three images.

BIBLIOGRAPHY

- [1] Accorsi, Roberto, "Analytic Derivation of the Contrast to Noise Ratio in Coded Aperture Imaging," Optical Society of America, 2005.
- [2] Accorsi, Roberto, "Design of Near-Field Coded Aperture Cameras for High-Resolution Medical and Industrial Gamma-Ray Imaging," Massachusetts Institute of Technology. June 2001.
- [3] Agostinelli, S. et al, *Nuclear Instruments and Methods in Physics Research A* 506, 250-303, (2003).
- [4] John Ball and Tony Price. Chesney's Radiographic Imaging, Sixth Edition. Malden: Wiley-Blackwell, 1995.
- [3] Barrett, Harrison H. and Swindell, William, Radiological Imaging: The Theory of Image Formation, Detection, and Processing. San Diego: Academic Press, 1981.
- [4] Cannon, T.M., and Fenimore, E.E., "Coded aperture imaging: many holes make light work," *Optical Engineering*, 19: 1980, 283-289.
- [5] Dr. Cristian Dinca, Staff Scientist, American Science and Engineering, Billerica, MA.
- [6] Dr. Omar al-Kofahi, Staff Scientist, American Science and Engineering, Billerica, MA.
- [7] Fenimore, E. E., "Coded aperture imaging: predicted performance of uniformly redundant arrays," *Applied Optics*, 17(22): 1978, 3562-3570.
- [8] Fenimore, E. E., "Tomographic Imaging using uniformly redundant arrays," *Applied Optics*, 18(7): 1979, 1052-1057.
- [9] Horn, B.K.P "Dynamic Reconstruction," *IEEE Transactions on Image Processing*, 2008, submitted for publication. The author is a co-author on this document.
- [10] Horn, B.K.P "Sequence with bi-level auto-correlation property equals its own DFT," *IEEE Transactions on Image Processing*, 2008, submitted for publication.
- [11] Knoll, Glenn F. Radiation Detection and Measurement, Third Edition. Ann Arbor: John Wiley & Sons, Inc., 2000.
- [12] Leary, Stephen. Improvised Explosive Devices (IEDs) & Counterinsurgency. Library Institute for Defense Analyses. Feb. 26, 2007. <<http://www.ida.gov>>
- [13] Mertz, L. and Young, N.O, in *Proceedings of the International Conference on Optical Instruments and Techniques*, K.J. Habel, Ed. (Chapman and Hall, London, 1961).
- [14] Park Medical Systems, ISOCAM II Operator's Manual. Park Medical Systems: 2005, 1-2.

- [15] Park Medical Systems, Inc. NEMA Performance Specifications for SMART Digital ISOCAM I and ISOCAM II Systems (1996)
<<http://www.med.harvard.edu/JPNM/physics/corps/park/specs.html>>
- [16] Sembiring, B O'Connor, D Li, A van Riessen, C Buckley and I Low. "Grazing Incidence X-Ray Diffraction characterization of Corrosion Deposits by Carbon Dioxide on Mild Steels", International Centre for Diffraction Data 2000, *Advances in X-ray Analysis*, Vol.43, 319 – 325.
- [17] United States. Training Circular No. 20-32-5. COMMANDER'S REFERENCE GUIDE Land Mine and Explosive Hazards (Iraq). Headquarters, Department of the Army, 13 Feb 2003.
<http://akocomm.us.army.mil/usapa/doctrine/20_Series_Collection_1.html>
- [18] United States. Headquarters of the Marine Corps. Field Manual Interim No. 3-34.119 Marine Corps Information Publication No. 3-17.01: Improvised Explosive Device Defeat. Sept. 2005, 3-1.
- [19] Zand, J. J. M. in 't. (1992, 1996) Coded aperture imaging in high-energy astronomy.
<http://astrophysics.gsfc.nasa.gov/cai/coded_intr.html>.
- [20] Zimmerman, Robert E. Instrument Quality Assurance: What is Required, Joint Program in Nuclear Medicine, Brigham & Women's Hospital, Harvard Medical School. Oct 2007.
<<http://www.med.harvard.edu/JPNM/physics/Zimmerman/Robert.html>>.
- [21] Ziock, Klaus P., Craig, William, Fabris, Lorenzo Fabris, Lanza, Richard, Gallagher, Shawn, Horn, Berthold K.P., Madden, Norm, 2004, "Large Area Imaging Detector for Long-Range Passive Detection of Fissile Material," *IEEE Transactions on Nuclear Science*, vol. 51, 2238-2244.
- [22] Ziock, Klaus P., Craig, William, Fabris, Lorenzo Fabris, Lanza, Richard, Gallagher, Shawn, Horn, Madden, Norm, Smith, E., and Woodring, and M.L., "Source-search sensitivity of a large-area, coded-aperture, gamma-ray imager," *IEEE Transactions on Nuclear Science*, vol. 53, no. 3, 1614–1621, June 2006.